DEFORMATION OF INTERIOR LAYERED DEPOSITS (ILD) AND THEIR ASSOCIATED LANDFORMS IN WEST CANDOR CHASMA, MARS: IMPLICATIONS FOR THE TIMING OF ILD DEPOSITION

Colin Birnie, BSc. (Hons.)

Submitted in partial fulfillment
of the requirements for the degree of
Master of Science

Department of Earth Sciences
BROCK UNIVERSITY
St. Catharines, Ontario
September 2011

Abstract

On Mars, interior layered deposits (ILD) provide evidence that water was once stable at the surface of the planet and present in large quantities. In West Candor Chasma, the ILD and their associated landforms record the depositional history of the chasma, and the deformation of those deposits provide insight into the stresses acting on them and the chasma as a whole. The post ILD structural history of West Candor is interpreted by analyzing the spatial relationships and orientation trends of structural features within the ILD. The recording of stresses through brittle deformation of ILDs implies that the ILD had been lithified before the stress was imposed.

Based on the prominent orientation trends of deformation features, the orientation of the stress regime acting upon the ILD appears to be linked to the regime that initially created the chasma-forming faults. An additional minor stress orientation was also revealed and may be related to large structures outside west Candor Chasma.

The late depositional history of Ceti Mensa is herein investigated by examining the attributes and spatial relationship between unique corrugated, linear formations (CLF). The CLFs appear to be aeolian in origin but display clear indications of brittle deformation, indicating they have been lithified. Evidence of lithification and the mineral composition of the surrounding material support the interpretation of circulating water in the area.

Acknowledgements

During the preparation of this manuscript, I received guidance and encouragement from Catherine Thomas, Dr. Frank Fueten, Dr. Robert Stesky, Dr. Rick Cheel and Dr. Mariek Schmidt. I am extremely grateful to them all.

Table of Contents

Chapter 1 1

1.1 Introduction 1

1.2 References 7

Chapter 2: Underlying structural control of small-scale fault and fracture orientations viewed in HiRISE images within west Candor Chasma, Mars 13

2.1 Introduction 13

2.2 Geologic Background 15

2.2.1 Interior Layered Deposits 21

2.2.2 Ceti Mensa 23

2.3 Methodology 24

2.3.1 Fracture Orientation and Local Slope 25

2.3.2 Fracture Orientation and Elevation 26

2.3.3 Data Presentation 27

2.4 Descriptions of Deformation Features 27

2.4.1 Orthogonal Fractures 27

2.4.2 En Echelon Fracture Sets 30

2.4.3 Unidirectional Fractures 31

2.4.4 Faults 32

2.4.5 Curved Fractures 33

2.5 Results 34

2.5.1 Topographic and Stratigraphic Effects on Fracture Orientation 34

2.5.2 Cumulative Fracture Data 36

2.5.3 Orthogonal Fractures 38

2.5.4 En Echelon Fractures 44

2.5.5 Unidirectional Fractures 46

2.5.6 Faults 49

2.5.7 Curved Fractures 50

2.6 Discussion 52

2.6.1 Regional Trends 52

2.6.2 Timing and Significance of Small-Scale Deformation Features 58

2.7 Conclusions 59

2.8 References 61

Chapter 3: Lithified aeolian bedforms as evidence for ancient water in Candor Chasma, Mars. 69

3.1 Introduction 69

3.1.1 Mineral Distribution 73

3.1.2 Aeolian Processes in Candor Chasma 74

3.2 Methodology 81

3.3 Results 82

3.3.1 Observations of the Corrugated Linear Features (CLF) 82

3.3.2 Active Aeolian Features 87

3.3.3 Yardangs 89

3.3.4 Light-Toned Unit (LTU) 90

3.4 Discussion 92

3.5 Conclusion 99

3.6 References.....100

Chapter 4: Overall Conclusions.....108

List of Tables

Table 2.1 – List of HiRISE images 20

Table 2.2 – Fracture orientations vs. topographic slope 34

Table 2.3 – En echelon fracture and shear zone orientations 45

Table 3.1 – List of characteristics displayed by active dunes and CLF 93

List of Figures

Chapter 1

Figure 1.1 – Location map of the Tharsis region of Mars 2

Chapter 2

Figure 2.1 – Location map of study area within Valles Marineris 15

Figure 2.2A – Labeled map of West Candor Chasma 18

Figure 2.2B – Labeled HRSC digital terrain model composite of West Candor..... 19

Figure 2.3 – Graph of topographic slope vs. deflection of fracture orientation..... 25

Figure 2.4 – Orthogonal fractures..... 29

Figure 2.5 – Irregular polygons 30

Figure 2.6 – En echelon fracture set and diagrammatic representation..... 31

Figure 2.7 – Unidirectional Fracture set 32

Figure 2.8 – Faults offsetting layered material 32

Figure 2.9 – Curved Fracture..... 33

Figure 2.10 – Distribution of elevations 35

Figure 2.11 – Orientation of fracture types vs. elevation 36

Figure 2.12 – Cumulative histograms for all fracture types 37

Figure 2.13 – Dominant orthogonal fracture orientations 41

Figure 2.14 – Secondary orthogonal fracture orientations..... 42

Figure 2.15 – Orthogonal fractures faintly visible below high albedo material 43

Figure 2.16 – Large scale fractures along the southeast border scarp of Ceti Mensa..... 44

Figure 2.17 – En echelon fracture orientations..... 46

Figure 2.18 – Unidirectional fracture orientations..... 48

Figure 2.19 – East pointing angular outcrops to the north of Ceti Mensa 49

Figure 2.20 – Trends of fault traces 50

Figure 2.21 – Curved fracture orientations 51

Figure 2.22 – Block diagram of a release fault 55

Figure 2.23 – Diagram for the formation of the conjugate en echelon arrays 57

Chapter 3

Figure 3.1 – CTX mosaic base map of the study and location map 71

Figure 3.2 – CTX and HiRISE images of central Ceti Mensa 72

Figure 3.3. – Flow model over linear dunes 77

Figure 3.4. – Model of cross strata attitudes within linear dunes 78

Figure 3.5. – Hypothetical model for cross strata formed by climbing transverse dunes.. 78

Figure 3.6 – Yardangs in LtU 80

Figure 3.7 – Scalloped texture in LtU 80

Figure 3.8 – Bifurcating CLF 84

Figure 3.9 – Characteristic planar truncations of CLF 84

Figure 3.10 – CLF offset by fault and truncated by fractures 85

Figure 3.11 – Nighttime infrared THEMIS image of Ceti Mensa 86

Figure 3.12 – HiRISE anaglyph of the southern extent of the intermediate plateau 87

Figure 3.13 – Sharp boundary between active dunes with different spacing 88

Figure 3.14 – Active linear dunes bifurcating 89

Figure 3.15 – Yardang, active dune and CLF orientations in West Candor Chasma 90

Figure 3.16A – Sharp contact between LTU and CLF 91

Figure 3.16B – Sharp contact between LTU and CLF showing elevated ridge 92

Figure 317. – Extensively orthogonally and polygonally fractured LTU.....92

Figure 3.18 – Comparison of superimposed dunes and corrugated texture on CLF 96

List of Abbreviations

CLF	Corrugated Linear Formations
CRISM	Compact Reconnaissance Imaging Spectrometer
CTX	Context Imager
HiRISE	High Resolution Imaging Science Experiment
HRSC	High Resolution Stereo Camera
ILD	Interior Layered Deposits
LTU	Light-toned Unit
MRO	Mars Reconnaissance Orbiter
OMEGA	Observatoire pour la Mineralogie, L'Eau, les Glaces et l'Activitié
THEMIS	Thermal Emission Imaging System

Chapter 1

1.1 Introduction

As one of the few terrestrial planets in our solar system, and the only other planet considered to be habitable, Mars is an important research subject in the field of planetary science. Its proximity to Earth allows for greater data collection than is feasible for planetary bodies at greater distances. The discovery of ice and large erosional channels, likely the result of large quantities of water previously stable at the surface [Aharonson et al., 2002; Sharp and Malin, 1975], has further increased the significance of Mars and changed our perceptions of it. Mars is thought to be of similar age as Earth. The Martian geologic timescale is divided into three epochs, beginning with Noachian period 4.56–3.7 Ga. the Hesperian from ~3.7–3.0 Ga. and followed by the most recent, the Amazonian, from ~3.0 Ga. to present [Hartmann and Neukum, 2001].

Two of the most obvious surface features on Mars are the Tharsis plateau and the Valles Marineris network incised into its eastern margin (Fig. 1.1). The Tharsis plateau is comprised of two broad topographic uplifts [Smith et al., 1999] of Noachian age, covered by younger volcanic flows (Late Noachian–Early Hesperian) from several volcanic edifices [Nimmo and Tanaka, 2005]. The northern uplift is dominated by the volcanic construct of Alba Patera, while the smaller volcanic edifices of Ascraeus Mons, Pavonis Mons, and Arsia Mons are superimposed on the larger southern uplift. The highest volcano on Mars, Olympus Mons, is situated off the western edge of the Tharsis plateau.

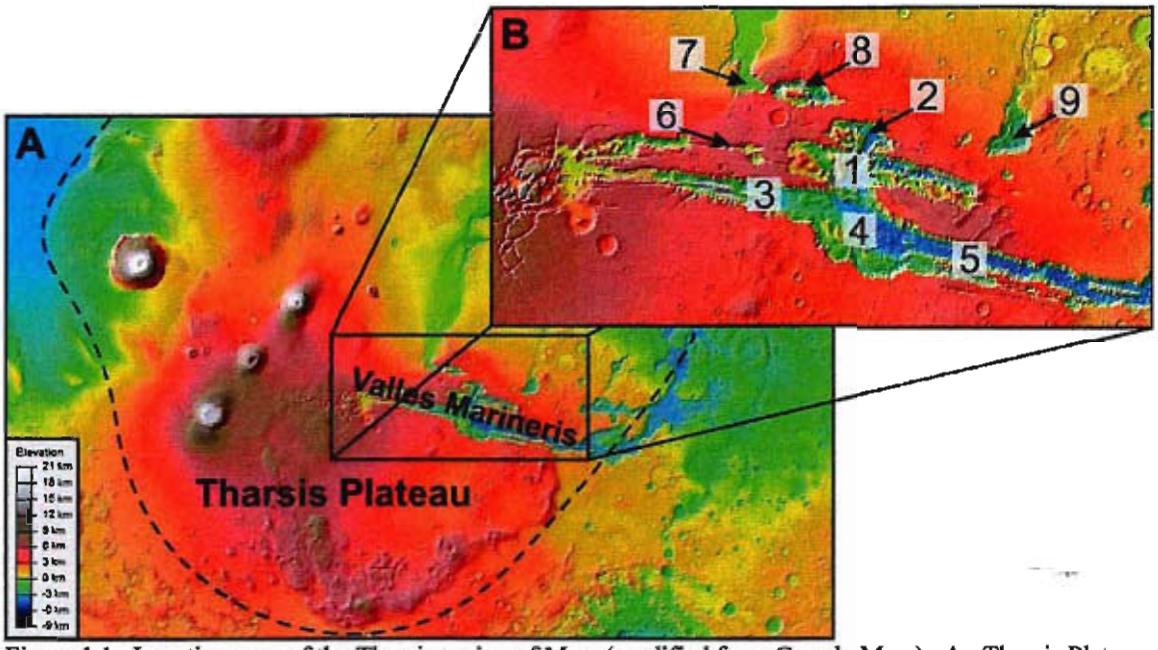

Figure 1.1. Location map of the Tharsis region of Mars (modified from Google Mars). A –Tharsis Plateau (outlined by black broken line) incised by the Valles Marineris on the eastern flank. B – Closer view of Valles Marineris and the other major geologic features of the region. (1) Candor Chasma, (2) Ophir Chasma, (3) Ius Chasma, (4) Melas Chasma, (5) Coprates Chasma, (6) Tithonia Catenae, (7) Echus Chasma, (8) Hebes Chasma and (9) Juventae Chasma.

The ~4000 km long Valles Marineris network of normal-fault-bounded troughs (Coprates, Ius, Candor, and Ophir Chasma) is defined by parallel, linear chasma walls and pit chains hundreds of kilometers long. The origin of such a large structural feature on a planet with no evidence of plate tectonics (such as convergent margins, transform fault systems or subduction zones) is therefore of great significance.

The evolution of Valles Marineris began in the early Hesperian [Tanaka et al., 1991; Witbeck et al., 1991; Dohm and Tanaka, 1999] with the development of compressional structures termed "wrinkle ridges" [Watters, 1993; Mangold et al., 1998; Schultz, 2000], aligned concentrically about the Tharsis region. Overprinting the wrinkle ridges are graben sets that formed radially around Tharsis during the Late Hesperian to Early Amazonian [Tanaka et al., 1991; Mège and Masson, 1996; Schultz and Fori, 1996]. Throughout the mid-Hesperian, large segments of subsiding crust [Spencer and Fanale,

1990, Schultz, 1998] (on the order of 10s of km^2) formed isolated ancestral basins [Lucchitta and Bertolini, 1989; Witbeck et al., 1991; Lucchitta et al., 1992, 1994; Schultz, 1998; Fueten et al., 2006], which were later linked by broadening and elongation through faulting [Lucchitta et al., 1994; Schultz and Lin, 2001] during the late Hesperian–Amazonian [Schultz, 1998; Peulvast et al., 2001]. Normal faults that bound the graben complex dip towards the centers of the troughs [Blasius et al., 1977; Masson, 1977, 1985; Lucchitta et al., 1992; Peulvast and Masson, 1993; Schultz, 1998; Peulvast et al., 2001; Schultz and Lin, 2001].

The troughs of Valles Marineris are up to 11 km deep [Lucchitta et al., 1994] and partially filled with younger, layered deposits, referred to as interior layered deposits (ILD) [Malin and Edgett, 2000]. ILD cover 17% of the total area and represent 60% by volume of all deposits [Lucchitta et al., 1994] within Valles Marineris. ILD cover ~35000 km^2 of West Candor Chasma, from elevations of -3.6 km to +3.1 km, relative to the global datum [Mangold et al., 2008] with several kilometers of conformable stratigraphy and a major late unconformity below the uppermost units [Fueten et al., 2008]. Spectral analysis of ILD [e.g. Bibring et al., 2005, 2006; Poulet et al., 2005; Gendrin et al., 2005; Murchie et al., 2007; Mustard et al., 2008], used to infer their mineralogy [e.g., Mangold et al., 2008; Murchie et al., 2009] has determined that both poly- and monohydrated sulfates were found to be large constituents of certain layered deposits.

The formation mechanisms responsible these widespread deposits are still contentious but it is unlikely a single process is responsible for such vast volumes of material. A myriad of processes have been proposed for the deposition, including

aqueous or subglacial volcanism [Komatsu et al., 2004; Lucchitta, 2004], exhumation of ancient material [Malin and Edgett, 2000; Catling et al., 2006], subaerial volcanism [Lucchitta, 1987, 1990; Chapman, 2002; Hynek et al., 2003; Komatsu et al., 2004], lacustrine deposition [Needell et al., 1987], aeolian deposition [Peterson, 1981] and combinations thereof [Malin and Edgett, 2000]. Investigation of layer attitudes [Lucchitta, 2004; Beyer and McEwen, 2005; Fueten et al., 2006; Hauber et al., 2006; Zegers et al., 2006; Gaddis et al., 2006; Fueten et al., 2008] have determined that layers commonly dip in the direction of the topographic slope at a shallow angle (< 20°). Their extensive exposure, thickness (up to thousands of meters) and shallow dip has made lacustrine deposition a favored method of ILD sedimentation [e.g., Komatsu et al., 2004; Fueten et al., 2006].

The abundant deformation structures (faults and fractures) documented within the ILD [e.g., Fueten et al., 2006, 2008; Okubo et al., 2008; Okubo, 2010] and the kilometers-high escarpments they form, suggest these sediments have been lithified [Malin and Edgett, 2000]. The material composing ILD is most likely fine grained sediments (sand, silt and/or clay) that breaks into small clasts when eroded because large boulders are not observed at the base of cliffs [Malin and Edgett, 2000]. If the observed competency of the ILD is not a result of sediment lithification but the solidification of layered resistant material, such as lava, large boulders would be expected to appear below cliffs.

Whether the ILD were emplaced within the isolated ancestral basins or in the chasmata after the normal faulting that linked them into their current configuration has been the subject of much debate. A post-chasma age for ILD is based on layered deposits

visible within the wall rock stratigraphy, limiting recent deposition to a thin mantling of aeolian sediments [e.g., Malin and Edgett, 2000, 2001; Catling et al., 2006]. Deposition of ILD within isolated ancestral basins, before the latest period of normal faulting, is supported by ILD distribution and structural mapping and has recently gained favor [e.g., Lucchitta, 1990, 1999; Witbeck et al., 1991; Lucchitta et al., 1994; Schultz, 1998; Chapman and Tanaka, 2001; Fueten et al., 2006, 2008; Okubo et al., 2008; Okubo, 2010].

This document integrates two separate studies (Chapters 2 and 3) on the geology of West Candor Chasma within Valles Marineris into a single thesis. The studies address two central questions:

- What does the deformation of ILDs and their associated landforms reveal about their genesis?
- What does the deformation of the ILDs indicate about the imposed stresses in West Candor Chasma?

Chapter 2 focuses on the structural evolution of Candor Chasma, using high resolution visible light imagery to measure the orientations of small-scale deformation features recorded within the ILD of West Candor to determine if a relationship exists with the chasma-forming faults. The orientations of the small-scale deformation features are analyzed to determine if any preferred orientations are present. By categorizing the different types of structural features, based on their morphology, it is possible to correlate their individual formation conditions with the patterns observed in their orientations and locations. This method recognized three preferred orientations of roughly 40°, 110°, 70° (from north), that were linked to the larger structural features in the chasma. These

patterns lead to an interpretation of the most recent stress regime acting on Candor Chasma and linked them to the larger structural features in the chasma. Determining the relationship between small-scale deformation features and the stress orientation is significant because it can establish the relative age of the ILD deposition and provides some insights into the length of time the regional stresses were active.

Chapter 3 is a study of unusual corrugated linear formations (CLF) on and around Ceti Mensa that display qualities of both unconsolidated active aeolian dunes and lithified material. To determine the genesis of these features, the morphological and thermal properties are analyzed using high resolution visible light imagery in conjunction with spectral and thermal data. The orientation, spacing and bifurcation modes displayed by the CLF are very similar to those of active aeolian dunes while qualities such as their apparent induration and corrugated texture are distinctly different. Furthermore, their low thermal inertia is inconsistent with lithified materials or unlithified active dunes. CLFs are found adjacent hydrated sulfate-rich material, the formation of which require water to form and may indicate water was present in these locations in the relatively recent past. Furthermore, the placement of CLF on the flanks of Ceti Mensa implies they formed after the ILD composing Ceti Mensa had been deposited and at least partially eroded [Geissler et al., 1993] or isolated by collapse of the chasma floor [Fueten et al., 2008].

Deformation structures in the ILD and CLF implies both were lithified before deformation occurred. Initial orientation data further shows that several preferred orientations are present throughout the study area. This indicates an underlying structural control and possibly reflects multiple periods of deformation.

1.2 References

Aharonson, O., M. T. Zuber, D. H. Rothaman, N. Schorghofer, and K. X. Whipple (2002), Drainage basins and channel incision on Mars, Proc. Natl. Acad. Sci. U. S. A., 99(4), 1780 – 1783, doi:10.1073/ pnas.261704198.

Bibring, J.-P., Langevin, Y., Gendrin, A., Gondet, B., Poulet, F., Berthé, M., Soufflot, A., Arvidson, R., Mangold, N., Mustard, J., Drossart, P., the OMEGA team 2005. Mars surface diversity as revealed by the OMEGA/Mars Express observations. Science, 307, 1576 – 1581, doi:10.1126/science.1108806.

Bibring, J.-P., Langevin, Y., Mustard, J. F., Poulet, F., Arvidson, R., Gendrin, A., Gondet, B., Mangold, N., Pinet, P., Forget, F., the OMEGA team, 2006. Global mineralogical and aqueous Mars history derived from OMEGA/Mars Express data. Science, 312, 400 – 404, doi:10.1126/science.1122659.

Beyer, R. A., McEwen, A.S., 2005. Constraints on the origin of fine layers in Ganges Mensa and Hebes Mensa, Mars. Lunar and Planet. Sci. XXXI, Abstract #1070.

Blasius, K.R., Cutts, J.A., Guest, J.E., Masursky, H., 1977. Geology of the Valles Marineris; first analysis of imaging from the Viking 1 orbiter primary mission. J. Geophys. Res., 82, 4067–4091

Chapman, M.G., Tanaka, K.L., 2001. Interior trough deposits on Mars: Subice volcanoes? J. Geophys. Res., 106, 10087–10100. doi:10.1029/2000JE001303.

Catling, D.C., Wood, S.E., Leovy, C., Montgomery, D.R., Greenberg, H.M., Glein, C.R., Moore, J.M., 2006. Light-toned layered deposits in Juventae Chasma, Mars. Icarus, 181, 26–51. doi:10.1016/j.icarus.2005.10.020.

Chapman, M. G., 2002. Layered, massive, and thin sediments on Mars: Possible Late Noachian to Late Amazonian tephra? In: Volcano-Ice Interactions on Earth and Mars. Smellie, J. L. and Chapman, M. G. (Eds.). Geol. Soc. Spec. Publ., London, 202, 273–203.

Dohm, J. M., Tanaka, K. L., 1999. Geology of the Thaumasia region, Mars: Plateau development, valley origins, and magmatic evolution. Planet. Space Sci., 47, 411–431.

Fueten, F., Stesky, R., MacKinnon, P., Hauber, E., Gwinner, K., Scholten, F., Zegers, T., Neukum, G., 2006. A structural study of an interior layered deposit in southwestern

Candor Chasma, Valles Marineris, Mars, using high resolution stereo camera data from Mars Express. Geophys. Res. Lett., 33. L07202. doi:10.1029/2005GL025035.

Fueten, F., Stesky, R., MacKinnon, P., Hauber, E., Gwinner, K., Scholten, F., Zegers, T., 2008. Stratigraphy and structure of interior layered deposits in west Candor Chasma, Mars, from High Resolution Stereo Camera (HRSC) stereo imagery and derived elevations. J. Geophys. Res., 113, doi:10.1029/2007JE003053.

Gaddis, J., Skinner, T., Hare, R., Kirk, T., Titus, L., Weller, G.N., HRSC Co-Investigator Team, U.S. Geological Survey, Astrogeology Program, 2006. Morphology and morphometry of Ceti Mensa, west Candor chasma, Mars. Lunar and Planet. Sci. XXXVII, Abstract #2076.

Geissler, P. E., Singer, R. B., Komatsu, G., Murchie, S., Mustard, J., 1993. An unusual spectral unit in west Candor Chasma: Evidence for aqueous or hydrothermal alteration in the Martian canyons, Icarus, 106, 380– 391, doi:10.1006/icar.1993.1179.

Gendrin, A., Mangold, N., Bibring, J.-P., Langevin, Y., Gondet, B., Poulet, F., Bonello, G., Quantin, C., Mustard, J., Arvidson, R., LeMouélic, S., 2005. Sulfates in Martian layered terrains: The OMEGA/Mars Express view. Science, 307, 1587–1591, doi:10.1126/science.1109087.

Hartmann, W.K., Neukum, G., 2001. Cratering chronology and the evolution of Mars, Space Sci. Rev., 96, 94– 165.

Hauber, E., Gwinner, K., Gendrin, A., Fueten, F., Stesky, R., Pelkey, S., Wulf, H., Reiss, D., Zegers, T., MacKinnon, P., Michael, G., Jaumann, R., Bibring, J.-P., Neukum, G., the HRSC Co-Investigator Team, 2006. An integrated study of interior layered deposits in Hebes Chasma, Valles Marineris, using MGS, MO, and MEX Data, Lunar and Planet. Sci. XXXVII, Abstract #2022.

Hynek, B. M., Phillips, R. J., Arvidson, R. E., 2003. Explosive volcanism in the Tharsis region: Global evidence in the Martian record. J. Geophys. Res., 108(E9), 5111, doi:10.1029/2003JE002062.

Komatsu, G., Ori, G. G., Ciarcelluti, P., Litasov, Y. D., 2004. Interior layered deposits of Valles Marineris, Mars: Analogous subice volcanism related to Baikal Rifting, Southern Siberia. Planet. Space Sci., 52, 167– 187.

Lucchitta, B. K., 1987. Recent mafic volcanism on Mars. Science., 235, 565–567.

Lucchitta, B.K., 1990. Young volcanic deposits in the Valles Marineris, Mars. Icarus, 86, 476–509. doi:10.1016/0019-1035(90)90230-7.

Lucchitta, B.K., 1999. Geologic Map of Ophir and Central Candor Chasmata MTM-05072 of Mars. US Geological Survey, Geologic Investigations Series Map I-2568.

Lucchitta, B.K., 2004. A volcano composed of light-colored layer deposits on the floor of Valles Marineris. Lunar and Planet. Sci. XXXV, Abstract #1881.

Lucchitta, B.K., Bertolini, L.M., 1989. Interior structures of Valles Marineris. In: Lunar and Planet. Sci. XX Proceedings, 590–591.

Lucchitta, B.K., McEwen, A.S., Clow, G.D., Geissler, P.E., Singer, R.B., Schultz, R.A., Squyres, W.W., 1992. The canyon system on Mars. In: Mars, Kieffer, H.H., Jakosky, B.M., Snyder, C.W., Matthews, M.S. (Eds.). Univ. of Arizona Press, Tucson, pp. 453–492.

Lucchitta, B.K., Isbell, N.K., Howington-Kraus, A., 1994. Topography of Valles Marineris: Implications for erosional and structural history. J. Geophys. Res., 99(E2), 3783–3798.

Malin, M.C., Edgett, K.S., 2000. Sedimentary rocks of early Mars. Science, 290, 1927–1937. doi:10.1126/science.290.5498.1927.

Mangold, N., Allemand, P., Thomas, P. G., 1998. Wrinkle ridges of Mars: Structural analysis and evidence for shallow deformation controlled by ice-rich décollements. Planet. Space Sci., 46 (4) 345-356.

Mangold, N., Gendrin, A., Gondet, B., LeMouelic, S., Quantin, C., Ansan, V., Bibring, J.-P., Langevin, Y., Masson, P., Neukum, G., 2008. Spectral and geological study of the sulfate-rich region of West Candor Chasma, Mars. Icarus, 194, 519– 543, doi:10.1016/j.icarus.2007.10.021.

Masson, P., 1977. Structure pattern analysis of the Noctis Labyrinthus–Valles Marineris regions of Mars. Icarus, 30, 49–62.

Mège, D., Masson, P., 1996. A plume tectonics model for the Tharsis province. Mars. Planet. Space Sci., 44 (12), 1499–1546. doi:10.1016/S0032- 0633(96)00113-4.

Murchie, S., Arvidson, R., Bedini, P., Beisser, K., Bibring, J.-P., Bishop, J., Boldt, J., Cavender, P., Choo, T., Clancy, R. T., Darlington, E. H., Des Marais, D., Espiritu, R., Fort, D., Green, R., Guinness, E., Hayes, J., Hash, C., Heffernan, K., Hemmler, J., Heyler, G., Humm, D., Hutcheson, J., Izenberg, N., Lee, R., Lees, J., Lohr, D., Malaret, E., Martin, T., McGovern, J. A., McGuire, P., Morris, R., Mustard, J., Pelkey, S., Rhodes, E., Robinson, M., Roush, T., Schaefer, E., Seagrave, G., Seelos, F., Silverglate, P., Slavney, S., Smith, M., Shyong, W.-J., Strohbehn, K., Taylor, H., Thompson, P., Tossman, B., Wirzburger, M., Wolff5, M., 2007. Compact Reconnaissance Imaging Spectrometer for Mars (CRISM) on Mars Reconnaissance Orbiter (MRO). J. Geophys. Res., 112, E05S03, doi:10.1029/2006JE002682.

Murchie, S.L., Roach, L.H., Seelos, F.P., Milliken, R.E., Mustard, J.F., Arvidson, R.E., Wiseman, S.M., Lichtenberg, K.A., Andrews-Hanna, J.C., Bibring, J.-P., Bishop, J.L., Parente, M., Morris, R.V., 2009. Evidence for the origin of layered deposits in Candor Chasma, Mars, from mineral composition and hydrologic modeling. J. Geophys. Res., 114, E00D05, doi:10.1029/2009JE003343.

Mustard, J. F., Murchie, S. L., Pelkey, S. M., Ehlmann, B. L., Milliken, R. E., Grant, J. A., Bibring, J.-P., Poulet, F., Bishop, J., Noe Dobrea, E., Roach, L., Seelos, F., Arvidson, R. E., Wiseman, S., Green, R., Hash, C., Humm, D., Malaret, E., McGovern, J. A., Seelos, K., Clancy, T., Clark, R., Marais, D. D., Izenberg, N., Knudson, A., Langevin, Y., Martin, T., McGuire, P., Morris, R., Robinson, M., Roush, T., Smith, M., Swayze, G., Taylor, H., Titus, T., Wolff, M., 2008. Hydrated silicate minerals on Mars observed by the CRISM instrument on MRO. Nature, 454, 305– 309, doi:10.1038/nature07097.

Nedell, S. S., Squyres, S. W., Andersen, D. W., 1987. Origin and evolution of the layered deposits in the Valles Marineris, Mars. Icarus, 70, 409–441.

Nimmo, F., Tanaka, k., 2005. Early crustal evolution of Mars. Annu. Rev. Earth Planet. Sci., 33, 133-161.

Neukum, G., Koenig, B., Fechtig, H., Storzer, D., 1975. Cratering in the Earth–Moon system: Consequences for age determination by crater counting. Lunar Planet. Sci. 6, 2597–2620.

Okubo, C. H., 2010. Structural geology of Amazonian-aged layered sedimentary deposits in southwest Candor Chasma, Mars. Icarus, 207, 210-225.

Okubo, C.H., Lewis, K.W, McEwen, A.S., Kirk, R.L., 2008. Relative age of interior layered deposits in southwest Candor Chasma based on high-resolution structural mapping. J. Geophys. Res., 113, E12002, doi:10.1029/ 2008JE003181

Peterson, C., 1981. A secondary origin for the Central Plateau of Hebes Chasma. In: Lunar and Planet. Sci. XII Proceedings, Part B, pp. 1459– 1471.

Poulet, F., Bibring, J.-P., Mustard, J. F., Gendrin, A., Mangold, N., Langevin, Y., Arvidson, R. E., Gondet, B., Gomez, C., the OMEGA Team, 2005. Phyllosilicates on Mars and implications for the early Mars history. Nature, 438, 623–627, doi:10.1038/nature04274.

Peulvast, J. P., Masson, P. L.,-1993. Erosion and tectonics in central Valles Marineris (Mars): A new morpho-structural model. Earth Moon Planets, 61, 191-217.

Peulvast, J.P., Mège, D., Chiciak, J., Costard, F., Masson, P.L., 2001. Morphology, evolution and tectonics of Valles Marineris wallslopes (Mars). Geomorphology, 37, 329–352.

Schultz, R.A., 1998. Multiple-process origin of Valles Marineris basins and troughs, Mars. Planet. Space Sci., 46, 827–834.

Schultz, R.A., 2000. Localization of bedding plane slip and backthrust faults above blind thrust faults: Keys to wrinkle ridge structure. J. Geophys. Res., 105, 12,035– 12,052. Sleep, N.H., Phillips, R.J., 1985. Gravity and lithospheric stress on the terrestrial planets with reference to the Tharsis region of Mars. J. Geophys. Res., 90, 4469-4489.

Schultz, R. A., Fori, A. N., 1996. Fault-length statistics and implications of graben sets at Candor Mensa, Mars. J. Struct. Geol., 18, 373-383.

Schultz, R.A., Lin, J., 2001. Three-dimensional normal faulting models of the Valles Marineris, Mars, and geodynamic implications. J. Geophys. Res., 106 (B8), 16,549–16,566.

Sharp, R. P., and M. C. Malin (1975), Channels onMars, Geol. Soc. Am. Bull., 86(5), 593– 609, doi:10.1130/0016-7606(1975)86<593:COM>2.0.CO;2.

Smith, D. E., Zuber, M. T., Solomon, S. C., Phillips, R. J., Head, J. W., Garvin, J. B., Banerdt, W. B., Muhleman, D. O., Pettengill, G. H., Neumann, G. A., Lemoine, F. G., Abshire, J. B., Aharonson, O., Brown, C. D., Hauck, S. A., Ivanov, A. B., McGovern, P.

J., Zwally, H. J., and Duxbury, T. C., 1999. The global topography of Mars and implications for surface evolution. Science, 284, 1495-1503.

Spencer, J. R., Fanale, F. P., 1990. New models for the origin of Valles Marineris closed depressions. J. Geophys. Res., 95, 14,301-14,313.

Tanaka, K. L., Golombek, M. P., Benerdt, W. B., 1991. Reconciliation of stress and structural histories of the Tharsis region of Mars. J. Geophys. Res., 96, 15,617-15,633.

Watters, T. R., 1993. Compressional tectonism on Mars. J. Geophys. Res., 98(E9), 17, 049-17,060.

Witbeck, N.E., Tanaka, K.L., Scott, D. H., 1991. The geologic map of the Valles Marineris region, Mars. U.S. Geol. Surv. Misc. Invest. Map, I-2010.

Zegers, T. E., Dabekaussen, W., Hauber, E., Gwinner, K., Scholten, F. Fueten, F., Stesky, R., MacKinnon, P., Neukum, G., HRSC Co-Investigator Téam, 2006. 3D structural analysis of Ophir Chasma based on HRSC image data and stereo-derived DTM. Lunar and Planet. Sci. XXXVII, Abstract #1605.

Chapter 2: Underlying structural control of small-scale fault and fracture orientations viewed in HiRISE images within west Candor Chasma, Mars

C. Birnie[1], F. Fueten[1], R. Stesky[2], E. Hauber[3], [1]Department of Earth Sciences, Brock University, St. Catharines, Ontario, Canada; [2]Pangaea Scientific, Brockville, Ontario, Canada; [3]Institute of Planetary Research, German Aerospace Center (DLR).

2.1 Introduction

Regional mapping of small-scale deformations features on Mars can reveal significant information about the regional stress history and the material being deformed. Structural analysis of Valles Marineris has previously been focused on large structural features, such as linear chasma walls and pit crater chains (e.g. Schultz, 1998; Schultz and Lin 2001) that define the distinct west-northwest orientation of Valles Marineris, or the localized deformation of ILD (e.g. Fueten et al., 2008; Okubo et al., 2008; Okubo, 2010), and not the regional distribution or orientation of small-scale deformation features within the chasmata. This study, which examines the orientations of small-scale deformation features visible within HiRISE images of West Candor Chasma, is meant as a preliminary investigation of what mechanisms, if any, determine the orientations of small-scale deformation features in Valles Marineris.

Within the Valles Marineris network of normal-fault-bounded troughs, displacement along large scale, basin-bounding normal faults (herein referred to as border faults) , internal (buried) normal faults [Schultz and Lin, 2001] and pre-existing cross faults [Wilkins and Schultz, 2003], collectively referred to as chasma forming faults, accommodated the collapse that produced the troughs of Valles Marineris. The west-northwest border fault orientations [Schultz and Lin, 2001] are reflected by the consistent alignment of Coprates, Ius, Candor, and Ophir Chasma. Chains of pit craters such as Tithonia Catenae also exhibit this common orientation and are thought to be the surface

expression of either dike emplacement [Schultz, 1998] or reactivation and lateral extension along border faults [Tanaka and Golombek, 1989; Wilkins and Schultz, 2003].

The troughs of Valles Marineris are up to 11 km deep [Lucchitta et al., 1994] and partially filled with younger, layered deposits, referred to as interior layered deposits (ILD) [Malin and Edgett, 2000]. Deformation features documented within the ILD [e.g. Fueten et al., 2006, 2008; Okubo, 2008, 2010] indicates these deposits are lithified to some degree. The lack of large mass wasting blocks, otherwise expected to accumulate beneath eroded outcrops of competent lithologies, may be attributed to fine grain sizes that allows ILD talus to break into small clasts when eroded [Lewis et al., 2009; Malin and Edgett, 2000].

Several authors have suggested structures such as pit chains [Blasius et al., 1977; Lucchitta, 1979, 1999; Spencer, 1983; Schultz, 1991; Lucchitta et al., 1992], fault scarps [Wilkins and Schultz, 2003] or orthogonal fracture sets [Fueten et al., 2009; 2010] observed in the area of West Candor Chasma to be the result of late reactivation of the chasma-forming faults. Evidence for the imposed stresses which initiated a late reactivation of chasma-forming faults should be recorded by the orientations of small-scale deformations features within ILD. Small-scale fractures, like the ones measured here, have been shown to form on Earth, parallel to the maximum horizontal compressive stress [Rives et al., 1994; Caputo, 1995; Twiss and Moores, 2007].

The study area is centered on Ceti Mensa, a large ILD at the western end of Candor Chasma (Fig. 2.1). The area around Ceti Mensa has been extensively targeted by High Resolution Imaging Science Experiment (HiRISE) [McEwen et al., 2007] with a maximum resolution of 25 cm/pixel, making it an ideal location to examine small-scale

structures. The orientations of a large number of small-scale deformation features within the ILD of West Candor were examined to determine they can provide insights into the geologic history of the ILD. Results show that their orientations display significant trends that can be related to the regional stress field and to movement along pre-existing cross-faults.

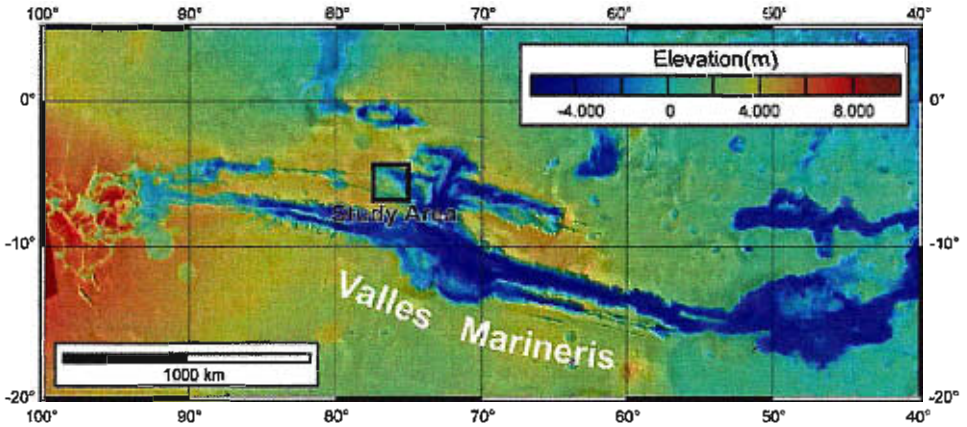

Figure 2.1. Location map of study area within Valles Marineris

2.2 Geologic Background

Valles Marineris is an approximately 4000 km long, network of fault-bounded troughs with a consistent NNW-SSE orientation, located on the eastern margin of the Tharsis plateau. The evolution of this region began in the early Hesperian [Tanaka et al., 1991; Witbeck et al., 1991; Dohm and Tanaka, 1999] with the development of compressional structures called "wrinkle ridges" [Watters, 1993; Mangold et al., 1998; Schultz, 2000], aligned concentrically about the Tharsis region. Wrinkle ridges are thought to be the surface expression of blind thrusts [Plescia and Golombek, 1986; Schultz, 2000] accommodating lithospheric loading of the Tharsis plateau [Banerdt et al., 1982; Sleep and Phillips, 1985]. Overprinting the wrinkle ridges are graben sets formed during the Late Hesperian to Early Amazonian [Tanaka et al., 1991; Mège and Masson,

1996; Schultz and Fori, 1996], distributed radially around Tharsis and thought to be a consequence of flexural loading stresses related to lithospheric deformation [Banerdt et al., 1992; Wilson and Head, 2002]. Throughout the mid-Hesperian [Spencer and Fanale, 1990, Schultz, 1998], large segments of subsiding crust (on the order of 10s of km^2) formed isolated ancestral basins [Lucchitta and Bertolini, 1989; Witbeck et al., 1991; Lucchitta et al., 1992, 1994; Schultz, 1998; Fueten et al., 2006], which were later linked by broadening and elongation through faulting [Lucchitta et al., 1994; Schultz and Lin, 2001] during the late Hesperian - Amazonian [Schultz, 1998; Peulvast et al., 2001].

Initial subsidence of crustal segments into the ancestral basins on the order of 3–5 km is reported by Lucchitta et al., [1994], while later fault-controlled subsidence may have lowered portions of Ius, Melas, Coprates, Candor and Ophir Chasma to levels below older, adjacent ILD [Schultz, 1998]. Normal faults that bound the graben complex dip towards the centers of the troughs [Blasius et al., 1977; Masson, 1977, 1985; Lucchitta et al., 1992; Peulvast and Masson, 1993; Schultz, 1998; Peulvast et al., 2001; Schultz and Lin, 2001]. Displacement along the border faults and interior buried faults (displacement on buried faults was minor relative to border faults) accommodated the roughly 6 km of vertical displacement necessary for the formation of Candor Chasma [Schultz and Lin, 2001].

Several troughs within Valles Marineris exhibit a rectangular profile for which different mechanisms have been proposed [e.g., Spencer and Fanale, 1990; Wilkins and Schultz, 2003]. The model proposed by Wilkins and Schultz [2003] to explain Candor Chasma's blunted terminations relies on pre-existing faults, oriented parallel to the principal extension trend of Valles Marineris (i.e., N-S). Such faults could be the blind

thrusts ascribed to wrinkle ridges, or normal faults involved in the formation of small graben [Wilkins and Schultz, 2003], predating extension and giving them the appropriate orientation. If, during N-S extension, border faults intersected one of these pre-existing faults, the pre-existing fault would reactivate to form a cross-fault and enable normal displacement in the hanging walls of the border faults [Wilkins and Schultz, 2003].

The normal faults bounding Candor Chasma [Wilkins and Schultz, 2003; Schultz and Lin, 2001] define trough walls (Fig. 2.2A) with the following orientations. The western blunted terminations are defined by the Northern Cross Fault (NCF) and the Southern Cross Fault (SCF), both of which have a general trend of ~40°. The southern boundary of Candor and the southern Tithonia Catenae pit chain are aligned along the Southern Border Fault (SBF), oriented at 107°. The Northern Border Fault (NBF) separating Candor and Ophir trends roughly 101°. The truncated central western wall is aligned with the northern pit chain of Tithonia Catenae and an embayment of Candor Mensa along a 105° trend is designated the Central Border Fault (CBF). In Candor, as described above, pre-existing faults were reactivated within the hanging walls of the border faults and formed the cross faults (NCF and SCF) along the northern and southern blunted terminations [Wilkins and Schultz, 2003].

Figure 2.2A. Labeled map of West Candor Chasma with Ceti Mensa outlined by thick white broken line. (1) Northwest blunted termination of Candor Chasma. (2) Northern border scarp of Ceti Mensa. (3) Northern re-entrant into Ceti Mensa. (4) Northeast border of Ceti Mensa. (5) Eastern re-entrant into Ceti Mensa. (6) Eastern prominence. (7) Southeast border scarp of Ceti Mensa. (8) Large discrete scarp. (9) Southwest blunted termination of Candor Chasma. X denotes the location of Figure 2.16. Letters in the top right corner of each HiRISE image location, defined by white boxes, correspond to Table 2.1. The proposed locations of large scale underlying border faults of Schultz and Lin (2001) are indicated by dashed lines with the bar and ball symbols on the on the hanging wall side of the faults (NBF = Northern Border Fault. CBF = Central Border fault. SBF = Southern Border fault). The cross fault locations proposed by Wilkins and Schultz (2003) are represented by a dash and two dots without a symbol designating the hanging wall (SCF = Southern Border Fault).

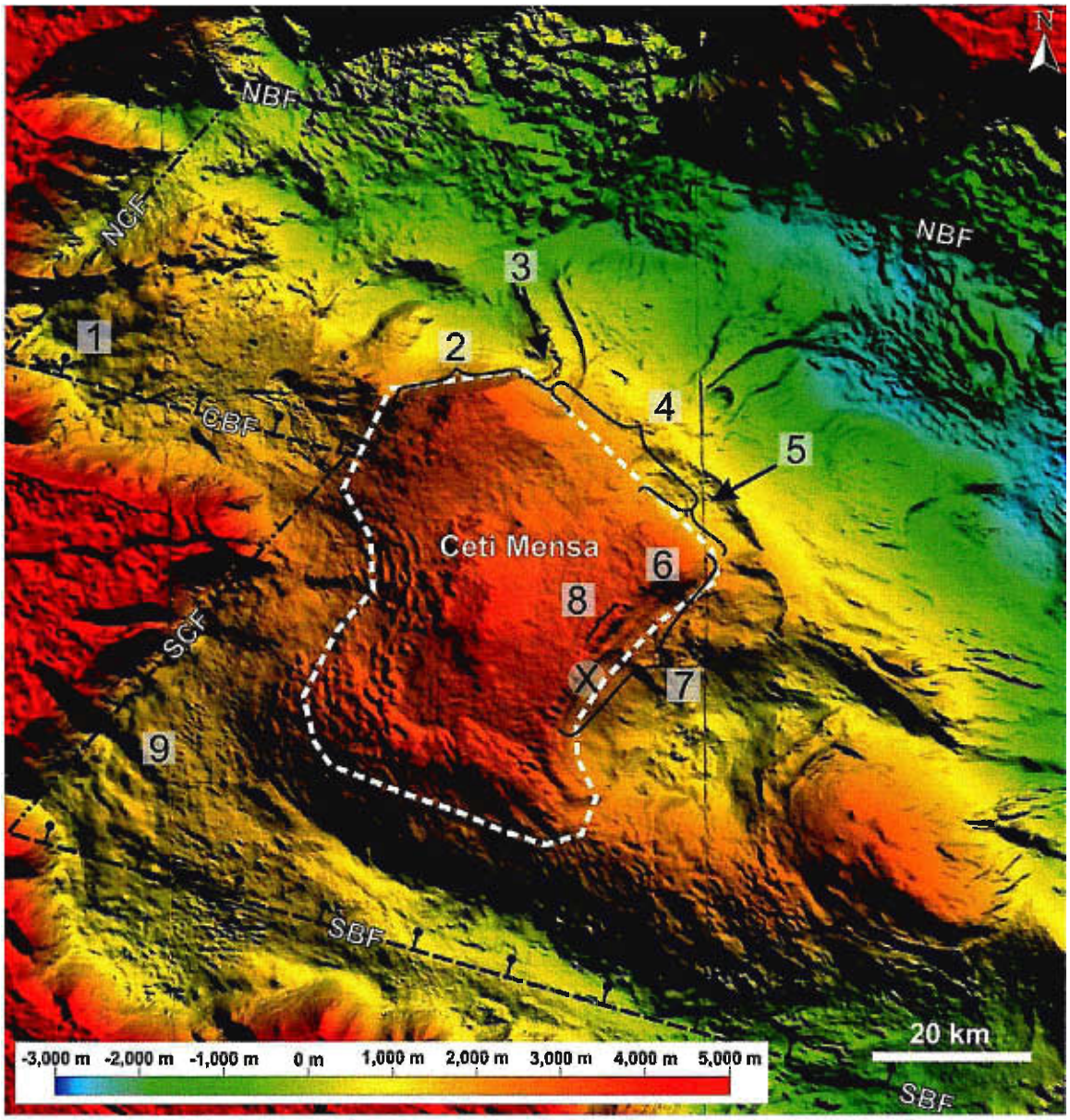

Figure 2.2B. Labeled High Resolution Stereo Camera (HRSC) [Jaumann et al., 2007] digital terrain model (DTM) composite of West Candor Chasma.

Table 2.1. List of HiRISE images used for this study and corresponding letters on all figures using the CTX mosaic of West Candor Chasma. The map projected scale of all the images is 25 cm/pixel. The X denotes the images which compose an anaglyph set.

Letter	HiRISE Image Number	Anaglyph
A	ESP_018374_1740	
B	PSP_002195_1745	X
	PSP_002406_1745	
C	PSP_002340_1735	
D	PSP_001918_1735	X
	PSP_001984_1735	
E	PSP_003540_1735	X
	PSP_003474_1735	
F	ESP_013350_1745	
G	PSP_003329_1745	
H	ESP_015895_1745	
I	PSP_002841_1740	X
	PSP_003896_1740	
J	PSP_002907_1745	
K	PSP_008814_1740	X
	ESP_016317_1740	

Letter	HiRISE Image Number	Anaglyph
L	PSP_007232_1740	X
	PSP_007021_1740	
M	PSP_009460_1745	X
	ESP_017741_1745	
N	PSP_010238_1745	X
	PSP_008023_1745	
	PSP_005386_1745	
O	PSP_003263_1740	
P	PSP_002129_1735	
Q	PSP_002696_1745	X
	PSP_003197_1745	
R	PSP_010093_1740	X
	PSP_010515_1740	
S	TRA_000836_1740	
T	PSP_009315_1745	
U	PSP_003830_1740	

Deformation of ILDs by faulting [Fueten et al., 2008; Okubo and McEwan, 2007; Okubo et al., 2008; Okubo, 2010] and fracturing [Fueten et al., 2008; Okubo, 2010] has been previously documented in West Candor. Structural observations of ILDs by Fueten et al. [2008] in West Candor Chasma demonstrates that certain prominent trends of fractures and other surface features are consistent throughout the area and may reflect underlying faults. In their study area directly adjacent ours, two regional trends approximately parallel to the southern and western borders of the chasma were displayed by fault scarps, fractures and linear depressions.

In the southwest corner of our study area, Okubo et al., [2008] attempted to determine the relative age of ILD by identifying chasma-forming faults within them.

They observe no strike-slip faults and no faults (thrust or normal) of sufficient size or appropriate orientation exposed at the surface to be categorized as chasma-forming faults. The average trend of 62° for normal faults in their study area is inconsistent with the predicted 110° orientations of Schultz and Lin [2001]. They conclude that the material within their study area represents mass-wasted (slump) material along a south-facing slope (movement is to the south), similar to the present topography. Later work in the same area by Okubo [2010] determined a population of sub-vertical joints (average trend of approximately 108°, average dip of 80° ±5°), consistent with minor chasma subsidence, to be the most recent deformation features in the area.

Pit chains, oriented parallel to the main trend of Valles Marineris (e.g., Tithonia Catenae) and perpendicular to the NNE-SSW axis of extension, developed during the late Amazonian [Blasius et al., 1997; Lucchitta, 1979, 1999; Spencer, 1983; Schultz, 1991; Lucchitta et al., 1992]. They extend from the corners of the chasma's blunted terminations where border and cross faults are assumed to intersect. It is during this episode of border fault motion, subsequent to the initial chasma opening, that reactivation and synchronous orthogonal extension (following Morewood and Roberts, 1997, 2000, 2001) of cross faults likely produced the blunted terminations observed in several chasmata (e.g., West Candor [Wilkins and Schultz, 2003]).

2.2.1 Interior Layered Deposits

Covering the chasma floors of Valles Marineris are layered deposits that have been eroded and deformed into a variety of landforms. Interior Layered Deposits (ILDs) cover 17% of the total area, representing 60% by volume of all deposits [Lucchitta et al., 1994] within Valles Marineris and display a variety of layer thicknesses, competencies

and albedos. Layered units are classified into three general categories by Malin and Edgett [2000], based on layer thickness, albedo and configuration: a) "Massive" units are a few hundred meters to a few kilometers thick with poor to no bedding and are light- to intermediate-toned. b) "Layered" units are composed of hundreds of thin, tabular units with a wide range of thicknesses of up to 2000 meters. This relatively thin bedding is light- to intermediate-toned with a characteristic stair-stepped morphology. c) "Thin mesa" units are dark- to intermediate-toned, and usually unconformably overlie massive or layered units.

Within West Candor, several kilometers of conformable stratigraphy are exposed with a major late unconformity below the uppermost units [Fueten et al., 2008]. The formation mechanisms responsible for such widespread deposits are still a matter of debate and it is unlikely a single process is responsible for the vast volumes of material and their associated landforms. The proposed processes of ILD deposition are: aqueous or subglacial volcanism [Komatsu et al., 2004; Lucchitta, 2004], exhumation of ancient material [Malin and Edgett, 2000; Catling et al., 2006], spring deposits [Rossi et al., 2008; Clarke and Bourke, 2009], subaerial volcanism [Komatsu et al., 2004], lacustrine [Needell et al., 1987], aeolian [Peterson, 1981], pyroclastic volcanism [Hynek et al., 2003; Chapman, 2002; Lucchitta,1987, 1990] and combinations thereof [Malin and Edgett, 2000].

Investigation of layer attitudes [Lucchitta, 2004; Beyer and McEwen, 2005; Fueten et al., 2006; Hauber et al., 2006; Zegers et al., 2006; Gaddis et al., 2006; Fueten et al., 2008] have determined that layers commonly dip in the direction of the topographic slope at a shallow angle (< 20°). The extensive exposure and shallow dip has made

lacustrine deposition a favored method of sedimentation [e.g., Komatsu et al., 2004; Fueten et al., 2006]. The diversity of attributes represented by ILD and their wide distribution indicate a variety of processes, preferentially forming ILD in specific environments.

The ages of ILD are also uncertain, though evidence has been provided supporting two evolutionary time scales. 1. The assumed presence of ILD within the wall rock stratigraphy lead to the interpretation that deposition took place before the formation of Valles Marineris and recent deposition is limited to mantling material [e.g., Malin and Edgett, 2000, 2001; Catling et al., 2006]. 2. ILD distribution and structural mapping supports deposition during and/or after the formation of the ancestral basins [e.g., Lucchitta, 1990, 1999; Witbeck et al., 1991; Lucchitta et al., 1994; Schultz, 1998; Chapman and Tanaka, 2001; Fueten et al., 2006, 2008; Okubo et al., 2008; Okubo, 2010]. In recent years, post- and/or syn-subsidence deposition has become the favored model of ILD emplacement. Layered material comprising Ceti Mensa and other large isolated ILDs were suggested to have been deposited in isolated sub-basins and acquired their current configuration by differential subsidence rates and magnitudes [Fueten et al., 2008].

2.2.2 Ceti Mensa

Ceti Mensa, an ILD spanning >2500 km^2 reaches heights of more than 5 km above the surrounding chasma floor [Lucchitta, 2007; Gaddis et al., 2006] and lies at the center of our study area in West Candor (Figs. 2.2A, B). Two domal edifices, separated by an NE-SW trending trough, are bordered by several scarps of 650 m to more than 1500 m of relief locally and expose a range of inclined layer morphologies. Both the

northern (Figs. 2.2A, B; 2) and southeast border scarps (Figs. 2.2A, B; 7) are defined by two deeply incised, rounded re-entrants (Figs. 2.2A, B; 3, 5) [Lucchitta, 2007]. The southeast border scarp is oriented at 40°, parallel to the western blunted terminations of Candor (Figs. 2.2A, B; 1, 9). The northeast border (Figs. 2.2A, B; 4), oriented ~124° is bifurcated by chaotic material sliding/flowing northward off Ceti Mensa. To the northwest, it is truncated by a normal fault (Figs. 2.2A, B; 2) 16 km long, striking 263° with at least 1.4 km of displacement and dips ranging from 28° and 36° [Fueten et al., 2007].

2.3 Methodology

Seven Context Imager [CTX; Malin et al., 2007] images were registered to HRSC elevation data of West Candor using Global Mapper (GIS/GPS mapping) software to construct a base map mosaic of the study area. Thirty-two HiRISE images were examined for this study and their locations recorded on the CTX mosaic to provide a context in which to view the measured orientations for each HiRISE image. The azimuth of the horizontal projection of the fracture trace will henceforth be referred to as the fracture's "orientation". All orientations were measured in plan view directly from HiRISE images using a digital on-screen protractor and were not corrected for the topographic slope because the fractures are assumed to be vertical. This assumption is reasonable because fractures are generally linear, even when formed in uneven topography and form steeply dipping cliff faces, despite the subsequent effects of erosion. The attitudes of joints measured in the south of our study area by Okubo [2010] of 80° ±5° also agree with this assumption. The orientations of vertical fractures are equal to their strike and give useful information about the stress orientations present during their

formation. For reasonably shallow slopes, such as those observed in the study area (maximum slope ~35°), the deflection generated by a non vertical (>60°) fracture is minimal, less than about 20° (Fig. 2.3).

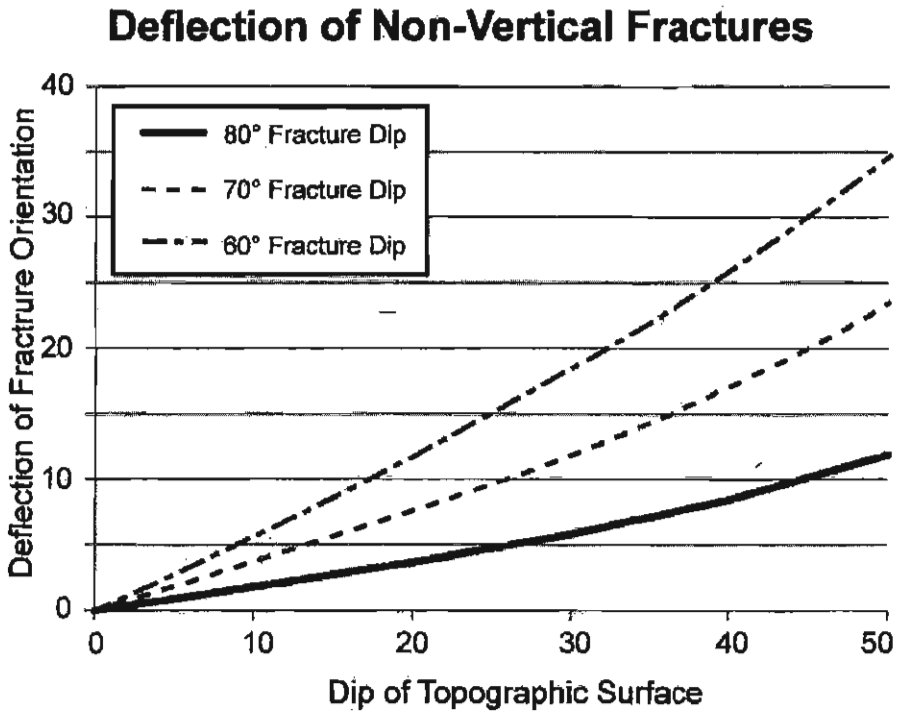

Figure 2.3. Graph of topographic slope vs. deflection of the recorded fracture orientation from the actual strike for various fracture dips.

The maximum resolution of the HiRISE images used for this study is 25 cm/pixel, requiring the length and aperture dimensions of deformation features (faults and fractures) to be at least 12 cm wide for them to be visible. Measurements of small-scale faults and fractures could only be made in areas covered by HiRISE images (unless otherwise noted) and are therefore inevitably biased by the location of the available HiRISE images.

2.3.1 Fracture Orientation and Local Slope

To determine if the fracture orientations were influenced by the directions of the topographic slope, possibly as a result of local slumping, HRSC digital elevation models

(0360_0000 (100 m/pixel) and 0334_0000 (100 m/pixel)) and Orion structural analysis software (http://www.pangaeasci.com) were used to compare fracture orientations with local topography at 15 locations (Table 2.2). It is unlikely that slumping would produce en echelon fractures sets or the observed faulting and they were therefore not tested by these means. Both orthogonal and unidirectional fractures form by similar means and may have been affected by topography. Orthogonal fractures are the most common fractures observed and were therefore selected to determine the influence of topography on their orientations. The difference between local surface strike direction and dominant fracture orientation was calculated as a value between 0-90°. If a relationship between the fracture orientation and slope exists, suggesting a local slumping origin, the difference between the two values is expected to be approximately 0° or 90°.

2.3.2 Fracture Orientation and Elevation

The formation of fracture systems may be strongly controlled by the mechanical properties of the rock [e.g. Lorenz et al., 2002]. No stratigraphic units have previously been identified but the measured dip of layering in the area is shallow [e.g. Fueten et al., 2007; Fueten et al., 2008] and therefore elevation can be used as a proxy for stratigraphic level (assuming no differential vertical displacement of equivalent units). The orientations of individual types of deformation features for a given location were averaged and recorded along with the locations elevation. The average orientation was used because the DTM resolution for this area is only 50–100 m/pixel and the elevation of individual deformation features cannot be resolved.

2.3.3 Data Presentation

Orientation data for all fracture types were plotted on circular histograms using the SpheriStat orientation analysis software (http://www.pangaeasci.com) to apply a Gaussian smoothing which compensated for the small number of data points collected in some areas. Data with a unimodal distribution were given a class interval so that the expected frequency value was equal to or greater than the standard deviation (Robin and Jowett, 1986). For very small data sets (N<7), it was sometimes impossible to achieve expected values less than the standard deviation even with the maximum class interval size of 45°. When graphing a clearly multimodal data set, a class interval which preserved the individual modal characteristics was used.

For HiRISE images that transect the borders of Ceti Mensa (HiRISE images K and L), two histograms were produced to display data from on top of and below Ceti Mensa accordingly. For HiRISE images J, M and O, where only a small portion of the image transects the border, the entirety of the data was collected in the area represented by the bulk of the image. Data for HiRISE image A, which transects the chasma floor, wall rock and plateau, was only gathered from chasma floor and the base of the wall rock and is represented by a single histogram.

2.4 Descriptions of Deformation Features

2.4.1 Orthogonal Fractures

Orthogonal fractures sets (Fig. 2.4) are composed of a dominant set and an orthogonally oriented secondary set. Both the dominant and secondary sets are extensional features composed of parallel to sub-parallel planar fractures with similar

spacing. The lengths of the dominant fractures are greater than four times the spacing between the members of the dominant set. Roughly orthogonal to the dominant set are the secondary fractures with short lengths, typically defined by the spacing between the members of the dominant fracture set. Secondary fractures generally terminate (abut) against the dominant fractures. In some areas, secondary fractures do transect dominant fractures but their lengths are less than four times the spacing of the dominant set. Relative to the dominant fractures, the orientations of the secondary fractures are more variable, a result of their short lengths. The intersection of the dominant and secondary fractures produces an equant to elongated rhombic pattern in plan view.

Previous work on the propagation of orthogonal fractures in terrestrial settings [e.g., Rives et al., 1994; Caputo, 1995; Bai et al., 2002] have proposed that the dominant set forms first, parallel to the maximum horizontal compressive stress (i.e., perpendicular to the maximum tensile stress). In Candor, the maximum horizontal compressive stress, assuming the border and cross faults are normal faults, would be parallel to them. After the dominant set forms, if a second stress is applied orthogonal or oblique to the initial stress, a secondary fracture set abutting the dominant fractures will form. The source of the secondary stress may result from one of a variety of sources such as orthogonal loading [Rives et al., 1994] or visco-elastic relaxation [Rives et al., 1994]. Visco-elastic relaxation displays both viscous and elastic properties, producing time dependant strain in the affected material [Twiss and Moores, 2007]. In orthogonal fracturing, visco-elastic relaxation allows for the gradual release of the initial stress, producing a tension normal to the initial extension, causing a secondary fracture set to develop progressively during relaxation [Rives et al., 1994].

A mutually cross-cutting relationship may occur if either the secondary stress is greater than the initial stress or the initial fractures are closed (healed) when the secondary stress is applied [Rives et al., 1994]. The orientation of the dominant fracture set is determined by the largest horizontal compressive stress. In general, only one fracture orientation is dominant and the fractures orthogonal to it are secondary. However, when the conditions previously discussed are satisfied and a mutually cross-cutting relationship is established, both orientations were recorded as being dominant.

Superficially, regions with orthogonal fractures may appear similar to polygonal patterned ground reported poleward of 55° latitude on Mars [Mangold et al., 2004] and formed through a combination of processes. Thermal contraction or desiccation of sediments can produce small, irregular fractures which are then progressively widened, elongated and interconnected by sediment infilling [Mangold et al., 2004; Sletten et al., 2003; Weitz et al., 2008]. Irregular polygons (Fig. 2.5) were excluded from our measurements as they do not fall within the categories specified for this study and are therefore not considered useful.

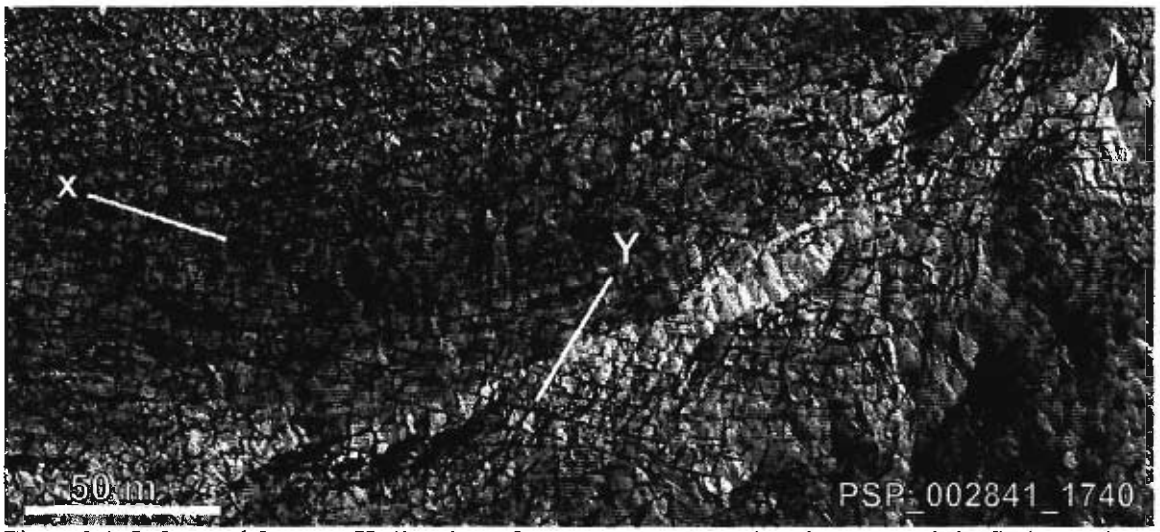

Figure 2.4. Orthogonal fractures X= Dominant fracture set. Y= Secondary fracture set (HiRISE image I).

Figure 2.5. Irregular polygons (HiRISE image L).

2.4.2 En Echelon Fracture Sets

En echelon fracture sets are composed of multiple fractures with nearly parallel orientations in an apparent en echelon pattern and roughly equal offset, either left or right stepping indicating the sense of shear (Fig. 2.6). En echelon fractures appear similar to gash fractures [Twiss and Moores, 2007] that have not undergone ductile shear and are assumed to have similar origins. Gash fractures are extensional features that form during shearing, the fractures being parallel to the maximum horizontal compressive stress and oblique to the orientation of the shear zone [Twiss and Moores, 2007]. With this in mind, the orientations of individual fractures within an en echelon array were recorded to document the maximum horizontal compressive stress direction and the overall trend representing the shear zone orientation is reported in Table 2.3.

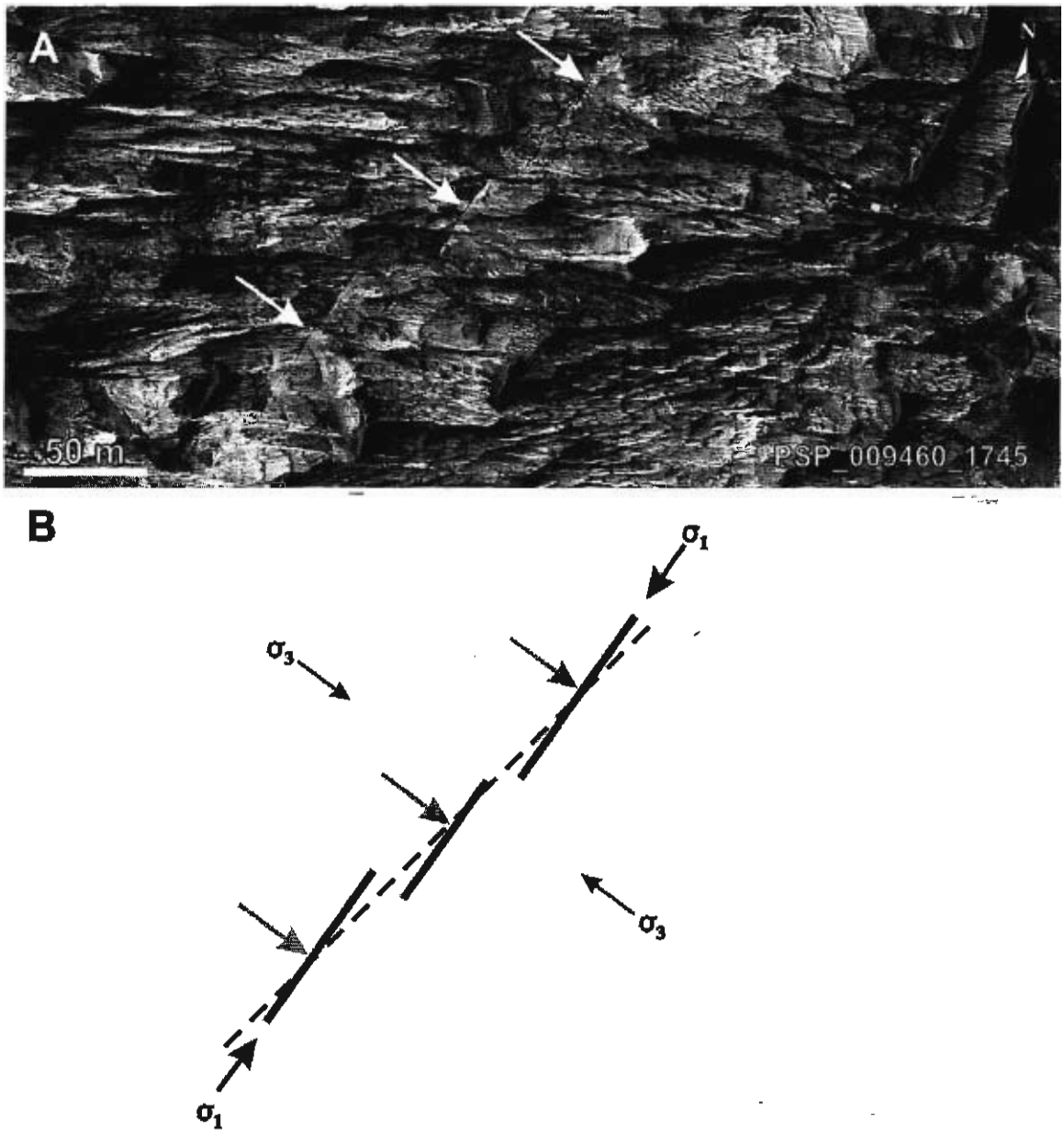

Figure 2.6. A – En echelon fracture set (HiRISE image M). White arrows point to individual fractures within the en echelon array and correspond to the gray arrows of B. B – Gash fracture formation model modified from Twiss and Moores, [2007]. The dashed line show the orientation of the shear zone, σ_1 is the direction of the maximum horizontal compressive stress and σ_3 is the direction of the minimum horizontal compressive stress.

2.4.3 Unidirectional Fractures

Unidirectional fractures are described as parallel to sub-parallel linear fracture sets with similar spacing but not occurring in conjunction with a secondary fracture orientation. These fractures can be 1000s of meters long but are generally 10s to 100s of

meters long (Fig. 2.7) and also form parallel to the maximum horizontal compressive stress [Engelder and Geiser, 1980].

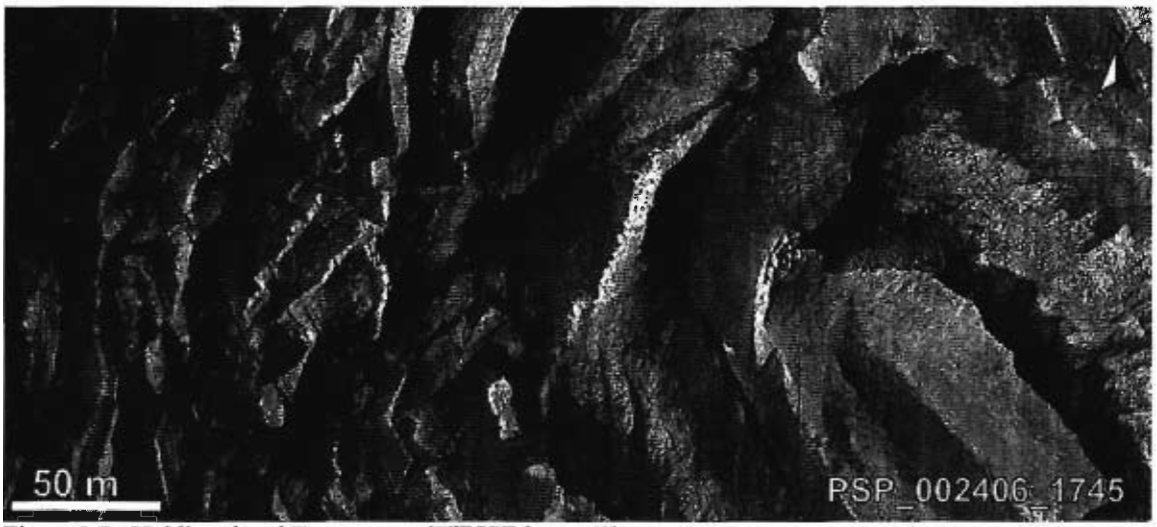

Figure 2.7. Unidirectional Fracture set (HiRISE image B)

2.4.4 Faults

Faults were defined by an observable apparent horizontal offset in layering or a scarp morphology only, and do not include more complex faults requiring detailed structural mapping for identification (Fig. 2.8). As only the apparent offset of the faults were visible, the true offsets could not be determined and only their orientation was recorded.

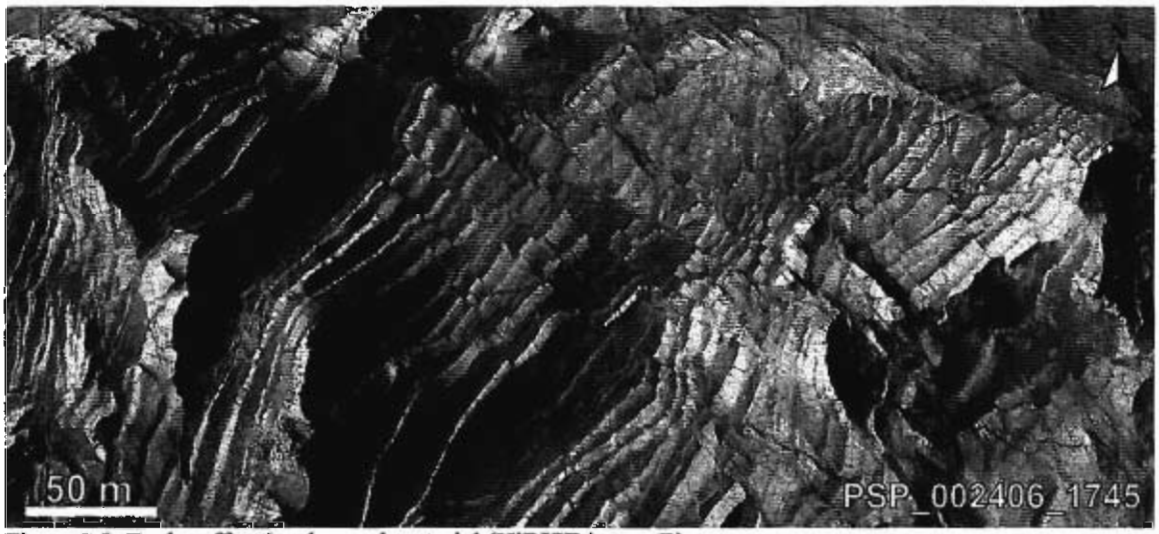

Figure 2.8. Faults offsetting layered material (HiRISE image B)

2.4.5 Curved Fractures

Fractures that display an irregular or curved trace are designated curved fractures. They were measured by visually estimating a straight line of best fit that accommodates their variable orientations. The curved profiles are consistent with extensional fractures formed by longitudinal splitting and not the result of topography and a low dip angle (although it may have accentuated the curvature). Material factors such as variations in tensile strength encouraging propagation along the path of lowest energy or the coalescing of individual fractures may also have played a role in creating their curved profile. Fractures with an overall curve to their profile may have experienced a rotational component during their formation, although the source of such rotation is unknown. Curved fractures are the only fracture type recorded that does not occur in parallel sets (Fig. 2.9).

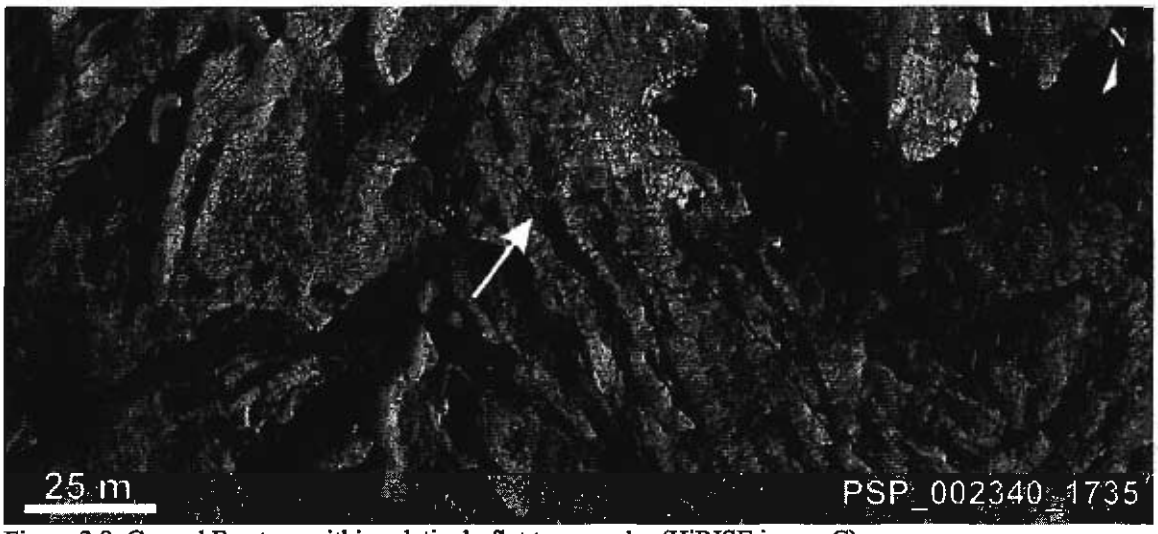

Figure 2.9. Curved Fracture within relatively flat topography (HiRISE image C)

2.5 Results

2.5.1 Topographic and Stratigraphic Effects on Fracture Orientation

The difference between the local average dominant fracture orientation and the local slope direction reported in Table 2.3, are highly variable and not give values of 0° or 90° that would indicate a relationship exists between them.

Table 2.2. Comparison of the dominant fracture orientations, from different parts of the study area, and the corresponding surface dip direction to determine if a relationship exists between the two values. Fracture orientations were measured from 0–180° while the strike and dip of the surface was recorded using right hand rule from 0–360°. The strike value was then converted to a commensurate value from 0–180° and the difference between the two measurements was expressed as a value from 0–90°.

HiRISE Image	Image Letter	Dominant Fracture Orientation (0–180°)	Strike / Dip of Surface	Difference Between Avg. Orientation and Strike (0–90°)
ESP_013350_1745	F	109	155 ± 15 / 05 ± 1	46
PSP_003329_1745	G	155	275 ± 18 / 05 ± 2	60
PSP_003329_1745	G	25	174 ± 16 / 11 ± 3	31
PSP_002841_1740	I	115	172 ± 14 / 16 ± 4	57
PSP_007232_1740	L	54	049 ± 9 / 11 ± 2	5
PSP_002696_1745	Q	26	079 ± 9 / 07 ± 1	53
PSP_002696_1745	Q	96	297 ± 6 / 09 ± 1	21
PSP_002696_1745	Q	31	109 ± 5 / 11 ± 1	78
ESP_015895_1745	H	88	298 ± 13 / 04 ± 1	30
ESP_015895_1745	H	46	030 ± 20 / 01 ± 0	16
PSP_007232_1740	L	54	191 ± 23 / 02 ± 1	43
PSP_002841_1740	I	107	190 ± 6 / 11 ± 1	83
ESP_013350_1745	F	108	129 ± 12 / 11 ± 3	21
ESP_013350_1745	F	43	124 ± 8 / 20 ± 2	81
ESP_013350_1745	F	119	124 ± 8 / 20 ± 2	5

The orientation of deformation features are recorded over a continuous range of elevations from 155 to 3217 m, with few observations between 155 m and -2608 m (Fig. 2.10). Orientation vs. elevation graphs for individual fracture types are provided below (Fig. 2.11). In the graph of dominant fracture orientations vs. elevation, two clusters of data for the 120° orientation are observed at ~1600 m and ~3000 m. The curved and

unidirectional fracture data is diffusely distributed but a bias for 3000 m is again present in both. However, the clustering of data along a given elevation, for a wide range of orientations, may indicate a sampling bias (many orientations measured in the same location and therefore with a similar elevation) and not a significant relationship between the elevation and orientation. A significant relationship between elevation and orientation will be a discrete cluster of data for a defined elevation and orientation. The small sample size for the en echelon fractures does not provide enough data to draw any definitive conclusions.

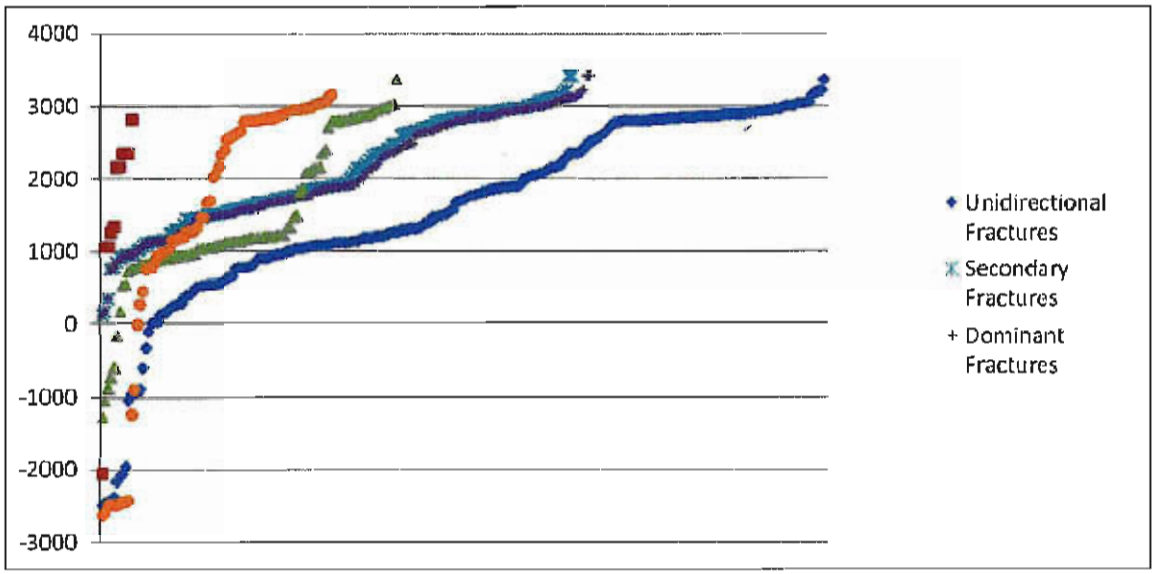

Figure 2.10. Distribution of elevations over which orientation data for each fracture type was recorded.

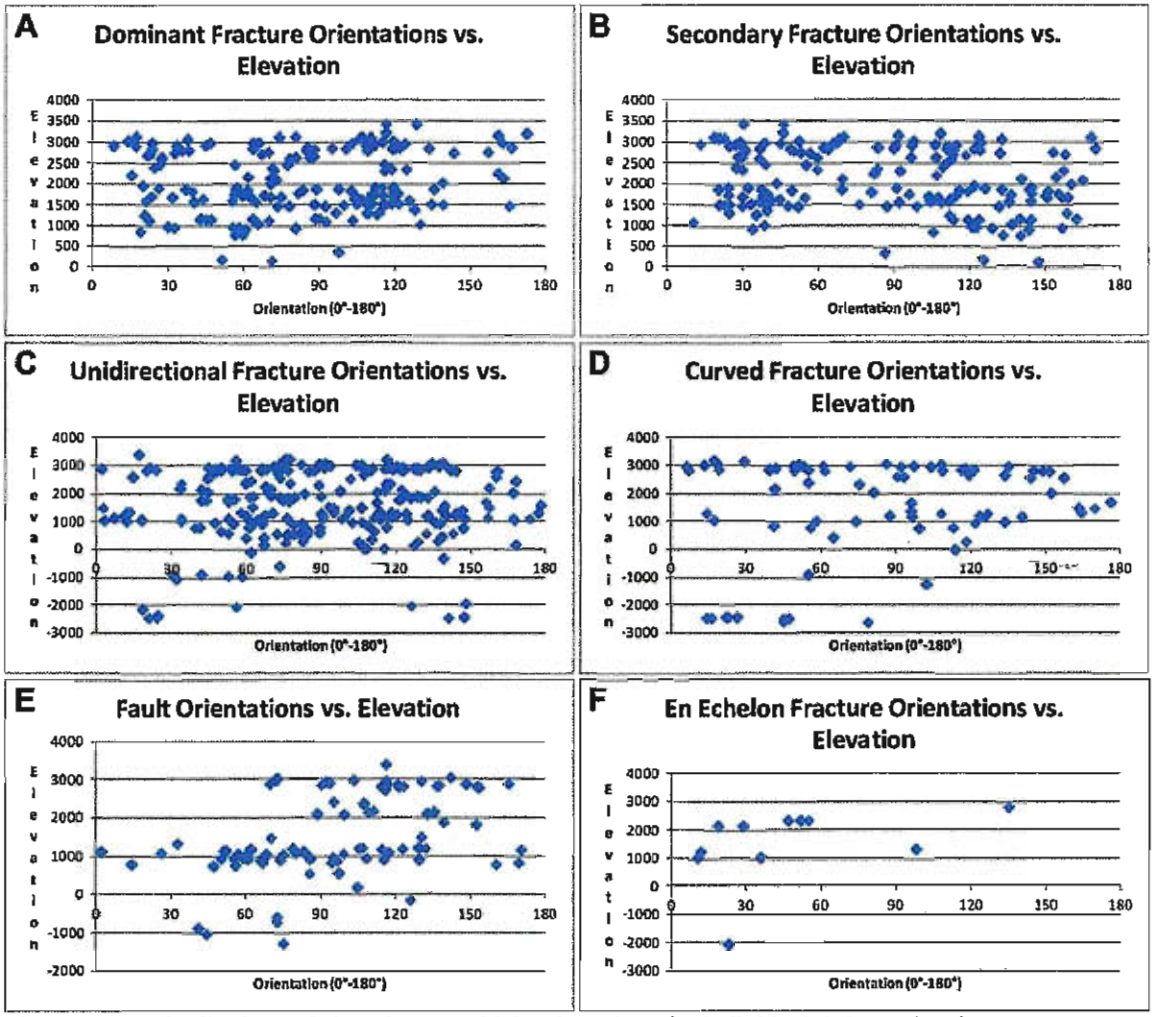

Figure 2.11. Distributions of elevations at which orientations for individual deformation feature types are recorded.

2.5.2 Cumulative Fracture Data

Where not obscured by dunes or mantling cover, faults and fractures can be observed throughout West Candor. Fracture abundance gradually diminishes to the east of Ceti Mensa due in large part to greater volumes of obscuring material. A data set incorporating the orientations of 683 faults, 3114 orthogonal fractures, 1027 unidirectional fractures, 286 curved fractures and 16 en echelon fracture sets (Fig. 2.12; A–K) was compiled.

Figure 2.12 displays the cumulative histograms for individual fracture types. Throughout the study area, orthogonal fractures predominate. Both the dominant and secondary orthogonal fracture histograms (Figs. 2.12; A, B & C) show two prominent regional trends of 20–40° and 100–125°. A secondary peak between 60–80° is also present in the dominant fracture histogram but not in the secondary fracture histogram.

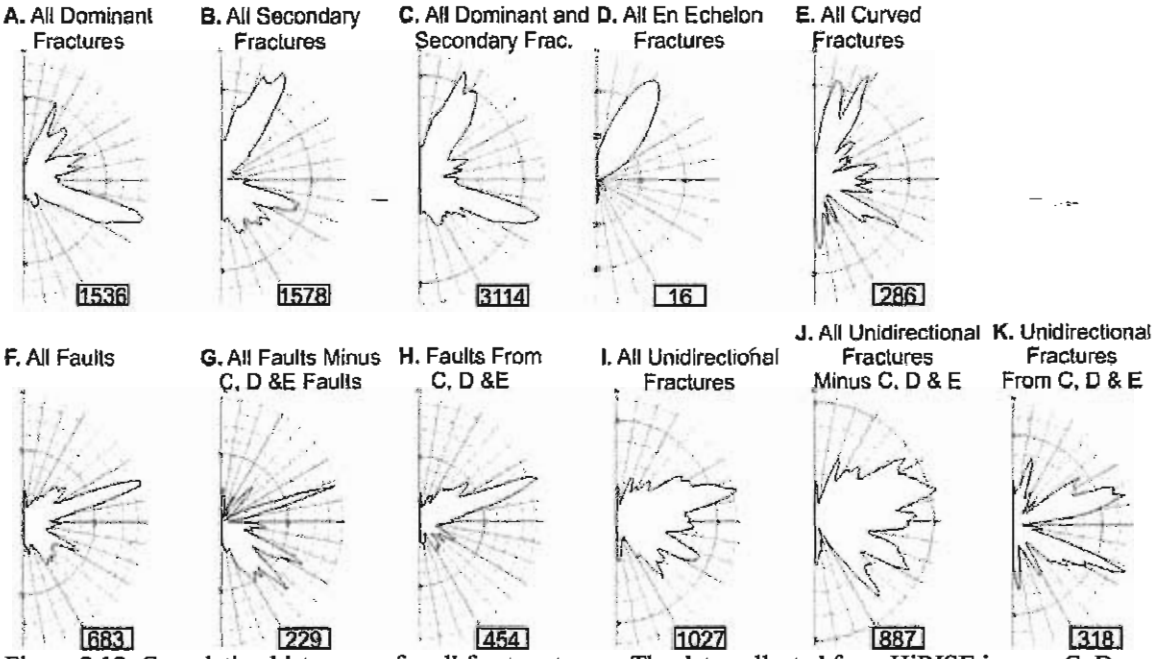

Figure 2.12. Cumulative histograms for all fracture types. The data collected from HiRISE images C, D and E has been presented separately for the faults and unidirectional fractures. The All Dominant and Secondary histogram is just a composite of the All Dominant and All Secondary histograms.

En echelon fractures display a very strong trend of 25 –55° parallel to the cross faults but the data set is quite small (Fig. 2.12; D).

The cumulative histogram for curved fractures (Fig. 2.12; E) reveals a wide distribution of orientations from 1° to 180°, but with three slightly larger populations, two at right angles to each other of 25–35° and 115–135° and one of 10–15°.

A prominent trend of 72° is observed for faults (Fig. 2.12; F). When the orientations of the faults in the SW (HiRISE images C, D and E), proposed by Okubo et

al., [2008] to be slump material are removed, this trend becomes more defined and two other trends of 115–125° and 135–155° become prominent (Fig. 2.12; G). The faults in C, D and E also display a prominent orientation trend of 70° but do not display an abundance of the 115–125° and 135–155° orientations (Fig. 2.12; H).

The cumulative histogram for unidirectional fractures (Fig. 2.12; I) shows a wide distribution within the study area but with a slight peak for 70–80° orientations. By removing the unidirectional fractures from the SW slump material this trend becomes less prominent and two trends of ~110–120° and ~140° stand out (Fig. 2.12; J). The unidirectional fracture data from HiRISE images C, D and E (Fig. 2.12; K) display two clearly preferred orientations which include the ~65–75° and 110–120° previously described for all unidirectional fractures and the dominant orthogonal fractures respectively. Local orientation trends for each fracture type are discussed below and presented separately in Figures 2.13, 2.14, 2.17, 2.18, 2.20 and 2.21.

2.5.3 Orthogonal Fractures

Near the inferred intersection of the CBF and SCF along the western margin of Ceti Mensa, areas of orthogonally fractured material, both atop western Ceti Mensa and in the surrounding lowlands (Figs. 2.13 & 2.14; F, G, H & I), display two principal orientations of roughly 105–120° and 20–30°. Both the dominant and secondary fracture sets display these well defined, preferred orientations and represent 47% of all the orthogonal fractures in the area.

Towards the center of southern Ceti Mensa (Figs. 2.13 & 2.14; I), the principal orientation of the secondary fracture set trends 10–30°, sub-parallel to the cross fault orientation and the dominant fracture set has a distinct 105°–120° trend parallel to the

border faults. In north central Ceti Mensa (Figs. 2.13 & 2.14; J), large regions of extensively fractured material are present but do not exhibit clearly defined dominant and secondary fracture sets. Instead, fractures have multiple orientations and produce irregular polygons.

Below much of Ceti Mensa's southeast border scarp, a layer of unfractured high albedo material covers the chasma floor. In places however, fractures are faintly visible underneath a thin covering (Fig. 2.15) or have not been covered and are clearly visible. Where orthogonal fractures are discernible below the southeast border scarp (Figs. 2.13 & 2.14; L) and to the east of the eastern prominence (Figs. 2.13 & 2.14; O & Q), two strong orientations of 20–65° and 105–145° were recorded in both fracture sets. The extent of the orthogonal fractures exhibiting these orientations spans the entire length of the scarp with only one exception. Secondary fractures recorded below the southeast border scarp within Figure 2.14; L, display a strong bimodal distribution of 20–35° and 130–145°. The 130–145° trend is parallel to one set of large unidirectional fractures visible in CTX image P16_007232_XN_05S076W (5.44 m/pixel) immediately to the west of this location (Fig. 2.16). These large fractures are visible along Ceti Mensa's southeast border scarp trending ~140° and dissect only the upper layered units. A few of the large unidirectional fractures appear to intersect a less well developed fracture set trending ~80° (Fig. 2.16; Y), producing angular outcrops.

Within the eastern re-entrant (Figs. 2.13 & 2.14; M), two orthogonal fracture sets within high albedo material display four strong trends. The larger set with a broader peak trends 60–75° (dominant set) and 135–160° (secondary set) while the second smaller well defined set trends, 57–62° (dominant) and 98–101° (secondary). In areas where

both orthogonal fracture sets are present, irregular polygons are formed. The dominant fractures of the smaller well defined trend cross-cut both the dominant and secondary fractures of the larger population set.

Both the northern and southern blunted terminations of West Candor (Figs. 2.13 & 2.14; A, B, C, D & E) display relatively few orthogonal fractures. The largest population of dominant fractures in the southern blunted termination (Figs. 2.13 & 2.14; C) displays two trends of 110–120° (Dominant) and 35–65° (Secondary). The orthogonal fractures in this area are not only fewer in number but are also not as well developed and have smaller dimensions (length and width), which reduce their visibility.

Figure 2.13. Histograms for the dominant orthogonal fracture orientations recorded in each HiRISE image location. The number of data points, N, for each image is recorded to the bottom right of the histogram and the size of each histogram has been scaled relative to the N value (>20 = large, ≤20 = small).

Figure 2.14. Histograms for the secondary orthogonal fracture orientations recorded in each HiRISE image location. The number of data points, N, for each image is recorded to the bottom right of the histogram and the size of each histogram has been scaled relative to the N value (>20 = large, ≤20 = small).

Figure 2.15. Orthogonal fractures are faintly visible below high albedo material and more clearly defined fractures not covered by later high albedo material.

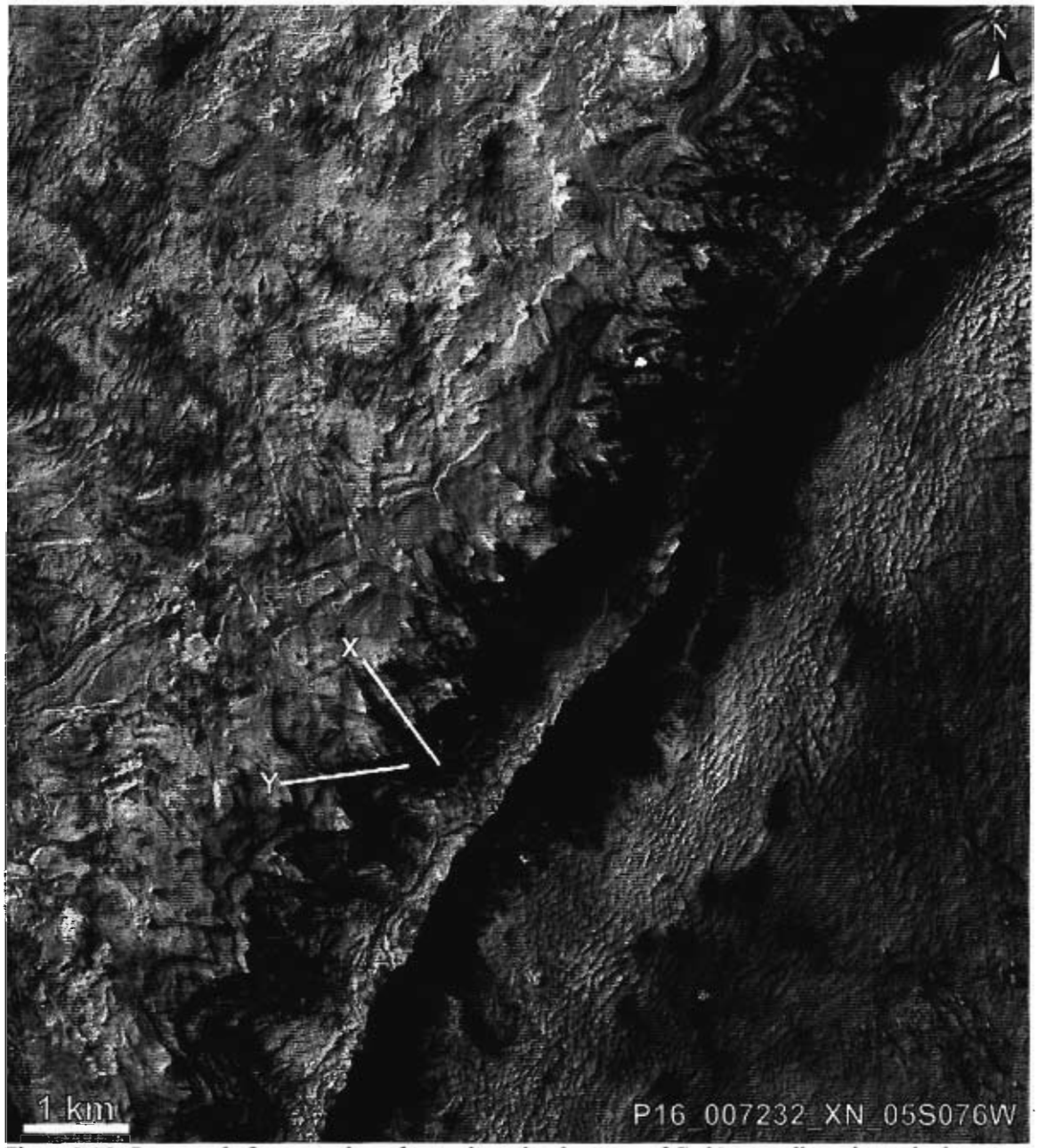

Figure 2.16. Large scale fractures along the southeast border scarp of Ceti Mensa dissecting only the uppermost layers of the section. The intersection of two fracture orientations parallel to X and Y forms the angular outcrops pointing east. (P16_007232_XN_05S076W (5.44 m/pixel))

2.5.4 En Echelon Fractures

En echelon fractures are most abundant below the eastern border scarp and within the eastern re-entrant where they display a strongly uniform orientation of 38° (Fig. 2.17; L & M). The sense of shear displayed by these en echelon fractures is not consistently

left or right stepping but with the exception of the data from HiRISE images E and H, the shear zone orientations are clustered according to their shear sense. En echelon arrays with a left stepping sense of shear have shear zone orientations from 11–33° while fracture arrays with a right stepping sense of shear have shear zone orientations from 40–76°.

Table 2.3. En echelon fracture orientations, shear zone orientations and sense of shear. All measurements in HiRISE image L are from below the eastern border scarp.

HiRISE Image Letter	Shear Sense	Fracture Orientation	Shear Zone Orientation
H	Left stepping	139	135
J	Left stepping	45	33
L	Left stepping	42	29
L	Left stepping	22	19
M	Left stepping	17	11
M	Left stepping	27	26
M	Left stepping	36	33
T	Left stepping	29	23
E	Right stepping	180	7
E	Right stepping	11	17
L	Right stepping	35	50
L	Right stepping	35	43
L	Right stepping	54	76
L	Right stepping	50	52
M	Right stepping	26	40
M	Right stepping	32	46

Figure 2.17. Histograms for the en echelon fracture orientations recorded in each HiRISE image location. Because of the small number of data points, the size of each histogram has not been scaled relative to the N value.

2.5.5 Unidirectional Fractures

Along the northern border scarp and to the north and west (Fig. 2.18; F & G), unidirectional fractures display a predominant trend of 60–105° while the scarp itself is oriented 83°. These unidirectional fractures intersect at a ~40° angle creating angular

outcrops aligned to the east (Fig.2.19), similar to the large unidirectional fractures along the southeast border scarp (Fig. 2.16) but in greater abundance.

In Figure 2.18; J, a strong peak of unidirectional fractures trends 105° with a minor peak at 15°. Below these in Figure 2.18; I, another large population displays two well defined trends of ~70° and ~130°. Along the base of the southeast border scarp, the most prominent orientation is oblique to the scarp at 65–70° (Fig. 2.18; L, O and Q) and is also reflected by one of two large unidirectional fracture sets that dissect the uppermost layers of the scarp (Fig. 2.16). A second, less prominent trend of ~40° is parallel to the southeast border scarp in Figure 2.18; O and L.

The northern blunted termination contains an abundance of unidirectional fractures with a strong trend of 97°. A lesser trend of 152° is also present, parallel to the dominant fault trend in the area. At the southern blunted termination, within the slump material described by Okubo et al., [2008] and Okubo [2010], two prominent trends are present. The first trend from 55–75° is oblique to both the chasma forming faults but parallel to the abundant small-scale faults in the area. The second is from 110–120°.

Figure 2.18. Histograms for the unidirectional fracture orientations recorded in each HiRISE image location. The number of data points, N, for each image is recorded to the bottom right of the histogram and the size of each histogram has been scaled relative to the N value (>20 = large, ≤20 = small).

Figure 2.19. East pointing angular outcrops to the north of Ceti Mensa's northern border scarp formed by the intersection of two unidirectional fracture sets parallel to X and Y (HiRISE image G).

2.5.6 Faults

The average apparent offset ranges between 5–15m over a trace length of 100–350 m but occasionally faults of over a kilometer are observed. Atop western Ceti Mensa (Fig. 2.20; H), faults with two general orientations occur. The larger population is oriented from 135–150° and is composed of faults with relatively short lengths. The second fault peak of 72° was predominantly recorded in the northern portion of Figure 2.20; H and these faults are generally longer that the faults to the south. Within the northern blunted termination, Figure 2.20; B has 69 faults with orientations of 125°–160°, east of the NCF (i.e., in the hanging wall). These faults are similar to the large population of faults observed atop western Ceti Mensa as they also have short lengths. Midway along the southeast border scarp (Fig. 2.20; L) is a discrete, 4 km long scarp, parallel to the southeast border. Faults below the southeast border scarp are perpendicular to the discrete scarp and also have short lengths.

Approximately 65% of all faults recorded are located within the highly deformed material documented by Okubo et al., [2008] and Okubo, [2010]. These faults have a

consistent strike of ~70° (Fig. 2.20; C, D & E), similar to the trend of normal faults reported by Okubo et al., [2008].

Figure 2.20. Histograms for the trends of fault traces recorded in each HiRISE image location. The number of data points, N, for each image is recorded to the bottom right of the histogram and the size of each histogram has been scaled relative to the N value (>20 = large, ≤20 = small).

2.5.7 Curved Fractures

To the north and east of Ceti Mensa's eastern prominence (Fig. 2.21; N & Q), populations of curved fractures with well-defined orientations parallel to the border faults

are observed (Fig. 2.21). Below the southeast border scarp in Figure 2.21; L, a large 75° trend is present parallel to several large unidirectional fractures and the Y orientation of the large scale fractures in Figure 2.16. Figure 2.21; T contains the largest population of curved fractures that display a well defined 15–28° trend.

Figure 2.21. Histograms for the curved fracture orientations recorded in each HiRISE image location. The number of data points, N, for each image is recorded to the bottom right of the histogram and the size of each histogram has been scaled relative to the N value (>20 = large, ≤20 = small).

2.6 Discussion

2.6.1 Regional Trends

The ILDs of West Candor have clearly been subjected to deformation in which the resulting small-scale structures developed non-random trends. These features are visible throughout West Candor and their consistent orientations favor an underlying structural control as opposed to the localized effects of topography, stratigraphic position or sediment desiccation. Topographic control over fracture orientation will produce fractures parallel and/or perpendicular to the local slope direction and would not produce preferred orientations that are consistent over areas of variable topography. The values presented in Table 2.2 comparing the dominant fracture orientation and the local slope direction do not consistently give values of 0° or 90°, indicating orientation of the dominant fractures are not controlled by the local topography.

There appears to be no clear relationship between fracture orientation and elevation. Dominant fracture orientations (Fig. 2.11; A), suggest two clusters of 120° fracture orientation at ~1600 m and ~3000 m. However this apparent relationship is most likely a sampling bias for these elevations, as result of the large number of data collected in HiRISE images F, H and I. The bias for these elevations is also evident in the 40° clusters within the secondary fractures vs. elevation graph (Fig. 2.11; B). The graphs for unidirectional and curved fractures (Fig. 2.11; C & D) also present a sampling bias at 3000 m elevation. Sampling biases are also present for 1000 m and 3000 m in the graph of fault orientations vs. elevations (Fig. 2.11; E) for a large range of orientations. The small sample size for the en echelon fractures (Fig. 2.11; F) does not provide enough data to draw any definitive conclusions. No data set shows clear isolated clusters of the same

orientation at different elevations. In the larger data sets, the full range of orientations is present all elevations with sufficient data. Hence we suggest that the fractures are present throughout the entire ILD stratigraphy and not governed by particular units.

Within the ILD of West Candor, several regional trends were recognized in the orientations of deformation features and interpretations of their genesis are given. The most prominent trend is found within the unidirectional fractures and orthogonal fracture sets, reflecting the postulated orientations of the border (101–107°) and cross (40°) faults. The second most prominent trend is 70° and was displayed by faults, unidirectional fractures and orthogonal fractures. A third trend is observed within the faults of West Candor, oriented 135–150°, roughly perpendicular to the inferred cross fault orientations. Assuming the simplest scenario of ILD deformation, a continuation of the imposed stress field which produced the chasma-forming faults, with a similar orientation, would produce small-scale deformation features and corresponding orientations. The number and distribution of deformation features may have been influenced by heterogeneities within the ILD (e.g. bed thickness, particle size, competency, etc) and could account for their inhomogeneous distribution throughout the study area.

During a continuation of the imposed stress field, unidirectional and dominant orthogonal fracture sets formed in direct response to the imposed stresses, parallel to the maximum horizontal compressive stress. Where a mutually cross-cutting relationship is present, both orthogonal fracture orientations (dominant and secondary) may be directly linked to the stresses which acted to produce the blunted terminations of West Candor. However, where no cross-cutting relationship is present, the alignment of the stresses

producing the secondary fracture sets is more ambiguous and may have resulted directly from the imposed stress or indirectly by the processes described by Rives et al., [1994].

Along the Ceti Mensa's southeast border scarp, orthogonal and unidirectional fracture histograms display several consistent trends parallel to the chasma-forming faults and the 70° trend which is discussed later. The alignment of orthogonal (Figs. 2.13 & 2.14; K, L below, O, Q, R and M) and unidirectional fractures (Fig. 2.18; L, O, R and M) parallel to the southeast border scarp may indicate a large fault underlies the southeast border scarp. The interaction of the imposed regional stress and an underlying fault could generate the observed fracture orientations along the south-eastern border scarp. This proposed fault may be another preexisting blind thrust (below a wrinkle ridge) aligned concentrically about the Tharsis region that was exploited later to form Ceti Mensa's south-eastern border scarp. The distance from the southeast border scarp to the SCF is 42 km, roughly the same distance between the NCF to the SCF. The frequency distribution of wrinkle ridge spacing reported by Watters [1991] based on 2934 measurements and displays an average spacing of 30 km (the mode, instead of the mean was used to obtain the most reliable measure because of the strongly skewed distribution). The value of ~42 km between cross-faults and between the SCF and southeast border scarp is well within the skewed frequency distribution range of ridge spacing. Hence we suggest that the south-eastern border scarp of Ceti Mensa is the eroded remnant of a larger now buried basement fault that may have been active during basin formation.

The prominent 133–151° trend of the small-scale faults in areas B and H of Figure 2.20 is slightly more than 90° from the inferred orientation of the nearby cross

fault. In both locations, relatively large populations of short faults with very uniform orientations are present at the intersection of a border and cross fault. This large number of highly uniform faults of short length is consistent with small cross faults termed "release faults" by Destro [1990]. The faults perpendicular to the southeast border scarp identified in area L of Figure 2.20 may also be release faults that accommodated bending stresses from displacement along the large underlying cross fault proposed above.

Release faults form to alleviate bending stresses accumulated by differential vertical displacement in the hanging wall of a normal fault (Fig. 2.22) and die out before intersecting another normal fault [Destro, 1995]. Release faults form near the fault tip and do not cut normal fault planes or detachment surfaces [Destro, 1995]. Generally, only one or two major release faults form over strike ramps or at the margins of a normal fault but smaller release faults may occupy intermediate positions. If a major release fault does not form, numerous small release faults may form along the length of the normal fault to accommodate the bending stresses [Destro, 1995].

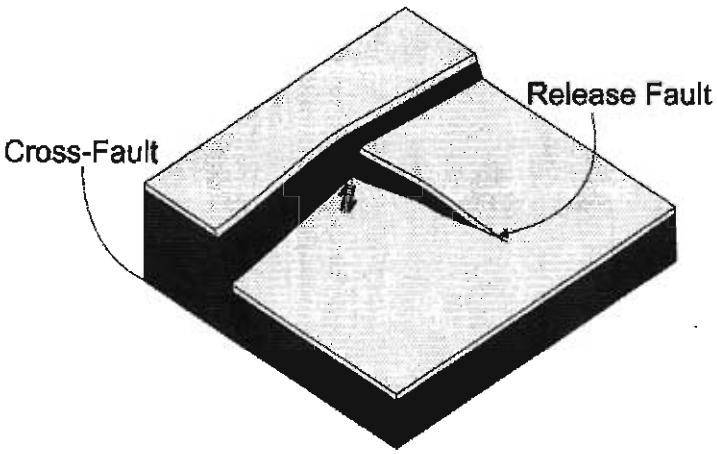

Figure 2.22. Block diagram of a release fault [modified from Destro, 1995]. Release faults accommodate predominantly vertical/dip-slip displacement and die out within the hanging wall before connecting to a second normal fault [Destro, 1995].

The 70° trend displayed by faults, unidirectional fractures and orthogonal fractures (Figs. 2.18 & 2.20; C, D, E, H, I, J, L, N, O and Q) is most abundant in the southwest of the study area (Figs. 2.18 & 2.20; C, D and E). The material in which they form is described by Okubo et al., [2008] and Okubo, [2010] as slump material shed off the southern flank of Ceti Mensa and eroded by aeolian processes. In this scenario, numerous faults would have formed parallel to the direction of movement to accommodate variable lateral displacement and can explain the heavily deformed appearance of the layered material. This explanation, however, does not resolve the presence of the 70° trend displayed by faults and unidirectional fractures in the other parts of the study area. The 70° trend is also prominent in faults atop northwestern Ceti Mensa, through central Ceti Mensa and north of the northern re-entrant. In these areas, the fault trend is almost parallel to the northern border scarp and is therefore more likely to have resulted from the same deformation event and not from slumping. This connection may suggest that none of the deformation features with a 70° orientation resulted from a slumping event. The extent with which the 70° trend occurs is significant but the trend does not appear to correlate with the regional trends within West Candor other than the northern border scarp. However, outside West Candor, the 70° orientation appears in several features, such as a graben complex south of Echus Chasma (78–84°), the southern border of Juventae Chasma (83°) and a pit chain that intersects the SW border of Hebes Chasma (74°). As this trend does not correlate to the orientation of the chasma-bounding faults within West Candor, it may be the result of post-collapse deformation.

The locations of the left and right stepping en echelon fracture sets are in close proximity and of similar orientation to the eastern border scarp and the proposed fault along it. While the number of fracture sets is limited, the two clusters of shear orientations could be interpreted as a conjugate set with a common maximum compressive stress direction of ~40° (Fig. 2.23). This orientation for the maximum compressive stress is consistent with one of the primary orthogonal fractures orientations.

Figure 2.23. Diagram for the formation of the conjugate en echelon arrays clustered about two shear zone orientations and a common maximum compressive stress orientation. A is the average orientation (22°) of the sinistrally offset en echelon fractures, produced by a dextral shear sense. B is the average orientation (58°) of the dextrally offset en echelon fractures, produced by a sinistral shear sense. The orientation of the individual fractures that compose the en echelon arrays is 40°, parallel to the maximum compressive stress. (Modified from Twiss and Moores, [2007])

Curved fractures display broad, multimodal orientation trends, only weakly subparallel to the border and cross faults. Hence, their origin cannot directly be linked to the movement of chasma-forming faults or to any other processes.

Other than the curved fractures, all of the trends discussed above indicate their development is the result of a pervasive underlying mechanism and not local topography or material properties.

2.6.2 Timing and Significance of Small-Scale Deformation Features

The occurrence of small-scale deformation features within ILD implies ILD had already formed and lithified before deformation. For the purpose of further discussion, we accept the prevalent view that ILD formed as ancestral basin fill (Lucchitta, 1990, 1999; Witbeck et al., 1991; Lucchitta et al., 1994; Schultz, 1998; Chapman and Tanaka, 2001; Fueten et al., 2006, 2008; Okubo et al., 2008; Okubo, 2010). The orientations of the deformation features within the ILD of West Candor record three strong trends, one of 70° and two that are parallel to the chasma-forming faults, suggesting the study area has undergone two distinct periods of deformation. The small displacement of the exposed deformation features indicates that they record minor amounts of strain; hence, no reactivation of chasma forming faults with significant offset could have occurred, nor indeed is reactivation required to produce the observed deformation features. Deformation features can form in response to applied stresses without the need for reactivation of major faults

Along the southern blunted termination, within the material described by Okubo et al., [2008] as an eroded slump, the small number of orthogonal fractures oriented parallel to the border and cross faults appears to represent a period of deformation that post-dates the eroded slump. Fractures which formed before the onset of slumping would have been obliterated during transport or modified to display highly variable orientations.

The small number, immature nature and orientations of these fractures are consistent with fractures formed recently in response to stresses parallel to the border and cross faults.

We attribute the 70° trend to a separate period of deformation which does not appear to be related to chasma formation since other features of this trend are located outside the chasma. We tentatively suggest that this deformation is a later event but further investigation is needed to definitively resolve the genesis of the 70° orientation.

2.7 Conclusions

The small-scale faults and fractures within the ILD of West Candor Chasma record the orientations of stress regimes acting on the region. By categorizing the small-scale deformation features by morphology and measuring their orientations, the imposed stresses are revealed, providing a better understanding of the geologic history of the ILD and Candor Chasma.

Within the measured orientations for all but the curved fractures, strong and well-defined orientation preferences are visible indicating non-random alignments controlled by consistent and pervasive underlying mechanisms. The alignment of these preferred orientations parallel to the chasma-forming faults indicates a close relationship between them. This relationship implies that chasma-forming faults were active after ILD emplacement and lithification. The small-scale deformation features were likely produced by a continuation of the imposed stress which initially produced the chasma forming faults. From the orientations of the small-scale deformation features measured in the study area, it is suggested that the orientation of this imposed stress was almost parallel to the stress that created the chasma-forming faults. The relationship observed between the orientations of small-scale surface structures and the imposed stress field

suggests that a large fault underlies the southeast border scarp, possibly another preexisting blind thrust. The recurrence of a ~70° trend, parallel to the northern border scarp, within the orientations of orthogonal and unidirectional fractures as well as numerous faults, indicates another period of deformation that may not have been limited to Candor Chasma.

The data presented in this paper demonstrates that small-scale deformation features can display regionally consistent orientations that offer insights into the regional stresses. It also provides a baseline data set for future investigation of small-scale deformation features, in other areas of Mars. Furthermore, the data suggests that the stresses responsible for the formation of Valles Marineris and the imposed stresses were not short lived.

2.8 References

Bai, T., Maerten, L., Gross, M. R., Aydin, A., 2002. Orthogonal cross joints: do they imply a regional stress rotation? J. Struct. Geol., 24, 77-88.

Banerdt, W.B., Phillips, R.J., Sleep, N.H., Saunders, R.S., 1982. Thick shell tectonics on one-plate planets: Applications to Mars. J. Geophys. Res., 87, 9723-9733.

Banerdt, W. B., Golombek, M. P., Tanaka, K. L., 1992. Stress and tectonics on Mars. In: Mars, Kieffer, H.H., Jakosky, B.M., Snyder, C.W., Matthews, M.S. (Eds.). Univ. of Arizona Press, Tucson, pp. 249–297.

Beyer, R. A., McEwen, A.S., 2005. Constraints on the origin of fine layers in Ganges Mensa and Hebes Mensa, Mars. Lunar and Planet. Sci. XXXI, Abstract #1070.

Blasius, K.R., Cutts, J.A., Guest, J.E., Masursky, H., 1977. Geology of the Valles Marineris; first analysis of imaging from the Viking 1 orbiter primary mission. J. Geophys. Res., 82, 4067–4091.

Caputo, R., 1995. Evolution of orthogonal sets of coeval extension joints. Terra Nova, 7, 479-490.

Catling, D.C., Wood, S.E., Leovy, C., Montgomery, D.R., Greenberg, H.M., Glein, C.R., Moore, J.M., 2006. Light-toned layered deposits in Juventae Chasma, Mars. Icarus, 181, 26–51. doi:10.1016/j.icarus.2005.10.020.

Chapman, M. G., 2002. Layered, massive, and thin sediments on Mars: Possible Late Noachian to Late Amazonian tephra? In: Volcano-Ice Interactions on Earth and Mars. Smellie, J. L. and Chapman, M. G. (Eds.). Geol. Soc. Spec. Publ., London, 202, 273–203.

Chapman, M.G., ed., 2007. The Geology of Mars: Evidence from Earth-based Analogs. Cambridge Planetary Science Series 5, Cambridge University Press. p 460.

Chapman, M.G., Tanaka, K.L., 2001. Interior trough deposits on Mars: Subice volcanoes? J. Geophys. Res., 106, 10087–10100. doi:10.1029/2000JE001303.

Clarke, J. D. A., Bourke, M. C., 2009. Recognition criteria of spring deposits on Mars at all scales: Evidence from the Dalhousie Springs analog (Australia). Lunar and Planet. Sci. XL, Abstract #1102.

Destro, N., Chagas, L. S., Chiossi, D. S. N., Machado, E. C. V., Masiero. G. H. N., 1990. Sistema em 'relay' associado a regime extensional na borda oeste da Bacia de Sergipe-Alagoas. In: XXXVI Congresso Brasileiro de Geologia Natal, Anais, 5, 2226-223?.

Destro, N., 1995. Release fault: A variety of cross fault in linked extensional fault systems in the Sergipe-Alagoas Basin, NE Brazil. J. Struct. Geol., 17, 615–629.

Dohm, J. M., Tanaka, K. L., 1999. Geology of the Thaumasia region, Mars: Plateau development, valley origins, and magmatic evolution. Planet. Space Sci., 47, 411–431.

Engelder T., Geiser P., 1980. On the use of regional joint sets as trajectories of paleostress fields during the development of the Appalachian plateau, N.Y. J. Geophys. Res. 85, 6319-6341.

Fueten, F., Stesky, R., MacKinnon, P., Hauber, E., Gwinner, K., Scholten, F., Zegers, T., Neukum, G., 2006. A structural study of an interior layered deposit in southwestern Candor Chasma, Valles Marineris, Mars, using high resolution stereo camera data from Mars Express. Geophys. Res. Lett., 33. L07202. doi:10.1029/2005GL025035.

Fueten, F., Stesky, R., MacKinnon, P., Hauber, E., Zegers, T., Gwinner, K., Scholten, F., Neukum, G., HRSC Co-Investigator Team, 2007. Faulting of ILD deposits on Ceti Mensa, Western Candor Chasma, Mars. Lunar and Planet. Sci. XXXVIII, Abstract #1388.

Fueten, F., Stesky, R., MacKinnon, P., Hauber, E., Gwinner, K., Scholten, F., Zegers, T., 2008. Stratigraphy and structure of interior layered deposits in west Candor Chasma, Mars, from High Resolution Stereo Camera (HRSC) stereo imagery and derived elevations. J. Geophys. Res., 113, doi:10.1029/2007JE003053.

Fueten, F., Racher, H., Stesky, R., MacKinnon, P., Hauber, E., McGuire, P., Zegers, T., Gwinner, K., 2010. Structural analysis of interior layered deposits in Northern Coprates Chasma, Mars. Earth and Planet. Sci. Lett., 294, 343-356.

Gaddis, J., Skinner, T., Hare, R., Kirk, T., Titus, L., Weller, G.N., HRSC Co-Investigator Team, U.S. Geological Survey, Astrogeology Program, 2006. Morphology and morphometry of Ceti Mensa, west Candor chasma, Mars. Lunar and Planet. Sci. XXXVII, Abstract #2076.

Gibbs, A. D., 1984. Structural evolution of extensional basin margins. J. Geol. Soc. London, 141, 609-620.

Hauber, E., Gwinner, K., Gendrin, A., Fueten, F., Stesky, R., Pelkey, S., Wulf, H., Reiss, D., Zegers, T., MacKinnon, P., Michael, G., Jaumann, R., Bibring, J.-P., Neukum, G., the HRSC Co-Investigator Team, 2006. An integrated study of interior layered deposits in Hebes Chasma, Valles Marineris, using MGS, MO, and MEX Data, Lunar and Planet. Sci. XXXVII, Abstract #2022.

Hynek, B. M., Phillips, R. J., Arvidson, R. E., 2003. Explosive volcanism in the Tharsis region: Global evidence in the Martian record. J. Geophys. Res., 108(E9), 5111, doi:10.1029/2003JE002062.

Jaumann, R., Neukumb, G., Behnkea, T., Duxburyc, T.C., Eichentopfa, K., Flohrera, J., Gasseltb, S.V., Giesea, B., Gwinnera, K., Haubera, E., Hoffmanna, H., Hoffmeistera, A., Köhlera, U., Matza, K-D., McCordd, T.B., Mertensa, V., Obersta, J., Pischela, R., Reissa, D., Ressa, E., Roatscha, T., Saigera, P., Scholtena, F., Schwarze, G., Stephana, K., Wählischa, M., HRSC Co-Investigator Team, 2007. The high-resolution stereo camera (HRSC) experiment on Mars Express: Instrument aspects and experiment conduct from interplanetary cruise through the nominal mission. Planet. Space Sci., 55, 928–952.

Komatsu, G., Ori, G. G., Ciarcelluti, P., Litasov, Y. D., 2004. Interior layered deposits of Valles Marineris, Mars: Analogous subice volcanism related to Baikal Rifting, Southern Siberia. Planet. Space Sci., 52, 167– 187.

Lewis, K., Aharonson, O., Grotzinger, J., Kirk, R., McEwen, A., Suer, T.-A., 2008. Quasi-periodic bedding in the sedimentary rock record of Mars. Science, 322, 1532–1535.

Lorenz, J. C., Sterling, J. L., Schechter, D. S., Whigham, C. L., Jensen, J. L., 2002. Natural Fractures in the Spraberry Formation, Midland Basin, Texas: The Effects of Mechanical Stratigraphy on Fracture Variability and Reservoir Behavior. AAPG Bulletin, 86, 505-524

Lucchitta, B. K., 1979. Landslides in Valles Marineris, Mars. J. Geophys. Res., 84, 8079-8113.

Lucchitta, B. K., 1987. Recent mafic volcanism on Mars. Science., 235, 565–567.

Lucchitta, B.K., 1990. Young volcanic deposits in the Valles Marineris, Mars. Icarus, 86, 476–509. doi:10.1016/0019-1035(90)90230-7.

Lucchitta, B.K., 1999. Geologic Map of Ophir and Central Candor Chasmata MTM-05072 of Mars. US Geological Survey, Geologic Investigations Series Map I-2568.

Lucchitta, B.K., 2004. A volcano composed of light-colored layer deposits on the floor of Valles Marineris. Lunar and Planet. Sci. XXXV, Abstract #1881.

Lucchitta, B. K., 2007. Multiple erosional and depositional episodes in West Candor Chasma, Mars. Lunar and Planet. Sci. XXXVIII, Abstract #2093.

Lucchitta, B.K., Bertolini, L.M., 1989. Interior structures of Valles Marineris. In: Lunar and Planet. Sci. XX Proceedings, 590–591.

Lucchitta, B.K., McEwen, A.S., Clow, G.D., Geissler, P.E., Singer, R.B., Schultz, R.A., Squyres, W.W., 1992. The canyon system on Mars. In: Mars, Kieffer, H.H., Jakosky, B.M., Snyder, C.W., Matthews, M.S. (Eds.). Univ. of Arizona Press, Tucson, pp. 453–492.

Lucchitta, B.K., Isbell, N.K., Howington-Kraus, A., 1994. Topography of Valles Marineris: Implications for erosional and structural history. J. Geophys. Res., 99(E2), 3783–3798.

Malin, M.C., Edgett, K.S., 2000. Sedimentary rocks of early Mars. Science, 290, 1927–1937. doi:10.1126/science.290.5498.1927.

Malin, M.C., Edgett, K.S., 2001. Mars Global Surveyor Mars Orbiter Camera: Interplanetary cruise through primary mission. J. Geophys. Res., 106(E10), 23429–23570. doi:10.1029/2000JE001455.

Malin, M. C., Danielson, G. E., Ingersoll, A. P., Masursky, H., Veverka, J., Ravine, M. A., Soulanille, T. A., 1992. Mars observer camera. J. Geophys. Res., 97(E5), 7699– 7718.

Malin, M.C., Bell III, J.F., Cantor, B.A., Caplinger,M.A., Calvin,W.M., Clancy, R.T., Edgett, K.S., Edwards, L., Haberle, R.M., James, P.B., Lee, S.W., Ravine, M.A., Thomas, P.C., Wolff, M.J., 2007. Context camera investigation on board the Mars Reconnaissance Orbiter. J. Geophys. Res., 112, doi:10.1029/2006JE002808.

Mangold, N., Allemand, P., Thomas, P. G., 1998. Wrinkle ridges of Mars: Structural analysis and evidence for shallow deformation controlled by ice-rich décollements. Planet. Space Sci., 46 (4) 345-356.

Mangold, N., Maurice, S., Feldman, W.C., Costard, F., Forget, F., 2004. Spatial relationships between patterned ground and ground ice detected by the Neutron Spectrometer on Mars. J. Geophys. Res., 109, E08001, doi:10.1029/2004JE002235.

Masson, P., 1977. Structure pattern analysis of the Noctis Labyrinthus–Valles Marineris regions of Mars. Icarus, 30, 49–62.

Masson, P. 1985. Origin and evolution of the Valles Marineris region of Mars. Adv. Space Res., 5(8), 83-92.

McEwen, A.S., Eliason, E.M., Bergstrom, J.W., Bridges, N.T., Hansen, C.J., Delamere, W.A., Grant, J.A., Gulick, V.C., Herkenhoff, K.E., Keszthelyi, L., Kirk, R.L., Mellon, M.T., Squyres, S.W., Thomas, N., Weitz, C.M., 2007. Mars Reconnaissance Orbiter's High Resolution Imaging Science Experiment (HiRISE). J. Geophys. Res., 112, E05S02, doi:10.1029/2005JE002605.

Mège, D., Masson, P., 1996. A plume tectonics model for the Tharsis province. Mars. Planet. Space Sci., 44 (12), 1499–1546. doi:10.1016/S0032- 0633(96)00113-4.

Morewood, N. C., Roberts, G. P., 1997. The geometry, kinematics and rates of deformation in a normal fault segment boundary, central Greece. Geophys. Res. Lett., 24, 3081– 3084.

Morewood, N. C., Roberts, G. P., 2000. The geometry, kinematics and rates of deformation within an en echelon normal fault segment boundary, central Italy. J. Struct. Geol., 22, 1027–1047.

Morewood, N. C., Roberts, G. P., 2001. Comparison of surface slip and focal mechanism slip data along normal faults: An example from the eastern Gulf of Corinth, Greece. J. Struct. Geol., 23, 473– 487.

Nedell, S. S., Squyres, S. W., Andersen, D. W., 1987. Origin and evolution of the layered deposits in the Valles Marineris, Mars. Icarus, 70, 409–441.

Okubo, C. H., 2010. Structural geology of Amazonian-aged layered sedimentary deposits in southwest Candor Chasma, Mars. Icarus, 207, 210-225.

Okubo C.H., McEwan A.S., 2007. Fracture-controlled paleo-fluid flow in Candor Chasma, Mars. Science, 315, 983–985.

Okubo, C.H., Lewis, K.W, McEwen, A.S., Kirk, R.L., 2008. Relative age of interior layered deposits in southwest Candor Chasma based on high-resolution structural mapping. J. Geophys. Res., 113, E12002, doi:10.1029/ 2008JE003181

Peulvast, J. P., Masson, P. L., 1993. Erosion and tectonics in central Valles Marineris (Mars): A new morpho-structural model. Earth Moon Planets, 61, 191-217.

Peulvast, J.P., Mège, D., Chiciak, J., Costard, F., Masson, P.L., 2001. Morphology, evolution and tectonics of Valles Marineris wallslopes (Mars). Geomorphology, 37, 329–352.

Peterson, C., 1981. A secondary origin for the Central Plateau of Hebes Chasma. In: Lunar and Planet. Sci. XII Proceedings, Part B, pp. 1459– 1471.

Plescia, J. B., Golombek, M. P., 1986. Origin of planetary wrinkle ridges based on the study of terrestrial analogs. Geol. Soc. Amer. Bull., 97, 1289– 1299.

Rives, T., Rawnsley, K.D., Petit, J.P., 1994. Analogue simulation of natural orthogonal joint set formation in brittle varnish. J. Struct. Geol., 16, 419–429.

Robin, P.-Y.F., Jowett, E.C., 1986. Computerized density contouring and statistical evaluation of orientation data using counting circles and continuous weighting functions. Tectonophysics, 121 (2–4), 207–233.

Rossi, A. P., Neukum, G., Pondrelli, M., van Gasselt, S., Zegers, T., Hauber, E., Chicarro, A., Foing, B., 2008. Large-scale spring deposits on Mars? J. Geophys. Res., 113, E08016, doi:10.1029/2007JE003062.

Schultz, R.A., 1991. Structural development of Coprates Chasma and western Ophir Planum, central Valles Marineris rift, Mars. J. Geophys. Res., 96, 22777–22792. doi:10.1029/91JE02556.

Schultz, R.A., 1998. Multiple-process origin of Valles Marineris basins and troughs, Mars. Planet. Space Sci., 46, 827–834.

Schultz, R.A., 2000. Localization of bedding plane slip and backthrust faults above blind thrust faults: Keys to wrinkle ridge structure. J. Geophys. Res., 105, 12,035– 12,052.

Schultz, R. A., Fori, A. N., 1996. Fault-length statistics and implications of graben sets at Candor Mensa, Mars. J. Struct. Geol., 18, 373-383.

Schultz, R.A., Lin, J., 2001. Three-dimensional normal faulting models of the Valles Marineris, Mars, and geodynamic implications. J. Geophys. Res., 106 (B8), 16,549–16,566.

Scott, D., Tanaka, K., 1986. Geologic Map of the Western Equatorial Region of Mars. US Geological Survey Investigation Series, Map I-1802-A.

Sleep, N.H., Phillips, R.J., 1985. Gravity and lithospheric stress on the terrestrial planets with reference to the Tharsis region of Mars. J. Geophys. Res., 90, 4469-4489.

Sletten, R.S., Hallet, B., Fletcher, R.C., 2003. Resurfacing time of terrestrial surfaces by the formation and maturation of polygonal patterned ground. J. Geophys. Res., 108 (E4), 25-1.

Smith, D.E., M.T. Zuber, H.V. Frey, J.B. Garvin, J.W. Head, D.O. Muhleman, G.H. Pettengill, R.J. Phillips, S.C. Solomon, H.J. Zwally, W.B. Banerdt, T.C. Duxbury, M.P. Golombek, F.G. Lemoine, G.A. Neumann, D.D. Rowlands, O. Aharonson, P.G. Ford, A.B. Ivanov, P.J. Mcgovern, J.B. Abshire, R.S. Afzal, X. Sun, 2001. Mars Orbiter Laser Altimeter: Experiment summary after the first year of global mapping of Mars. J. Geophys. Res., 106, 23689–23722.

Spencer, J. R., 1983. A tectonic geomorphological classification of the walls of Valles Marineris (abstract). In Reports of Planetary Geology Program. NASA Tech. Memo., NASA TM-86246, 243–245.

Spencer, J. R., Fanale, F. P., 1990. New models for the origin of Valles Marineris closed depressions. J. Geophys. Res., 95, 14,301-14,313.

Tanaka, K. L., Golombek, M.P., 1989. Martian tension fractures and the formation of grabens and collapse features at Valles Marineris. Lunar and Planet. Sci. XIX, 383–396.

Tanaka, K. L., Golombek, M. P., Benerdt, W. B., 1991. Reconciliation of stress and structural histories of the Tharsis region of Mars. J. Geophys. Res., 96, 15,617-15,633.

Twiss, R. J., Moores, E. M., 2007. Structural Geology, 532 pp., W. H. Freeman, New York.

Watters, T. R., 1991. Origin of Periodically Spaced Wrinkle Ridges on the Tharsis Plateau of Mars. J. Geophys. Res., 96, No. E1, 15,599-15,616.

Watters, T. R., 1993. Compressional tectonism on Mars. J. Geophys. Res., 98(E9), 17, 049-17,060.

Weitz, C.M., Milliken, R.E., Grant, J.A., McEwen, A.S., Williams, R.M.E., Bishop, J.L., 2008.
Light toned strata and inverted channels adjacent to Juventae and Ganges chasmata, Mars. Geophys. Res. Lett., 35, L19202. doi:10.1029/2008GL035317.

Wilkins, S.J., Schultz, R.A., 2003. Cross faults in extensional settings: Stress triggering, displacement localization, and implications for the origin of blunt troughs at Valles Marineris, Mars. J. Geophys. Res., 108(E6), 5056, doi:10.1029/2002JE001968.

Wilson, L., Head, J. W., 2002. Tharsis-radial graben systems as the surface manifestation of plume-related dike intrusion complexes: Model and implications. J. Geophys. Res., 107(E8), 5057, doi:10.1029/ 2001JE001593.

Witbeck, N.E., Tanaka, K.L., Scott, D. H., 1991. The geologic map of the Valles Marineris region, Mars. U.S. Geol. Surv. Misc. Invest. Map, I-2010.

Zegers, T. E., Dabekaussen, W., Hauber, E., Gwinner, K., Scholten, F. Fueten, F., Stesky, R., MacKinnon, P., Neukum, G., HRSC Co-Investigator Team, 2006. 3D structural analysis of Ophir Chasma based on HRSC image data and stereo-derived DTM. Lunar and Planet. Sci. XXXVII, Abstract #1605.

Chapter 3: Lithified aeolian bedforms as evidence for ancient water in Candor Chasma, Mars.

C. Birnie[1], F. Fueten[1], R. Stesky[2], R. Cheel[1], A. P. Rossi[3]. [1]Department of Earth Sciences, Brock University, St. Catharines, Ontario, Canada; [2]Pangaea Scientific, Brockville, Ontario, Canada; [3]Jacobs University Bremen, Bremen, Germany.

3.1 Introduction

The eastern flank of Tharsis plateau is incised by the Valles Marineris network of fault-bound chasmata with a maximum depth of 11 km and east-west extent of more than 4000 km. Most chasmata of Valles Marineris are partially filled with aeolian sediments and thick, layered deposits, referred to here as Interior Layered Deposits (ILD) [Malin and Edgett, 2000]. This study focuses on Ceti Mensa, a deeply eroded ILD remnant [Lucchitta, 2010] in West Candor Chasma (Fig. 3.1A) and the previously undescribed features along its slopes. The morphology, mineralogy and thermal attributes of these new features provide evidence supporting their origin as aeolian sediments, lithified by water at the surface and/or circulating in the subsurface in several possible environments (e.g. hydrothermal, sedimentary) [Bibring et al., 2007].

Ceti Mensa is flanked to the north and southeast by two deeply incised re-entrants (Fig. 3.1B). Geissler et al., [1993] first recognized the re-entrant floors as likely candidate sites for circulating and possible ponding of hydrothermal fluids. The interpretations of Geissler et al., [1993] and those of subsequent authors [e.g. Bibring et al., 2007] are based on the close association of ferric oxides and hydrated sulfate mineral deposits, thought to form by acidic groundwater and associated alteration [Bibring et al., 2007], within the re-entrants. The placement of sulfate and oxide deposits within the re-entrants implies they formed after Ceti Mensa had been at least partially eroded [Geissler et al., 1993] or isolated by collapse of the chasma floor [Fueten et al., 2008].

In Context Imager (CTX) [Malin et al., 2007] imagery (6.64 m/pixel) of West Candor, large areas of Ceti Mensa and the southeast re-entrant floor appear to be covered by active dune fields (Fig. 3.2A). In this paper, the term *active dunes* will be applied to all non-indurated aeolian bedforms with dune morphology, regardless of whether they are currently mobile (i.e., undergoing erosion and deposition) and can change orientation and morphology in response to a changing wind regime. However, the High Resolution Imaging Science Experiment (HiRISE) [McEwen et al., 2007] (25 cm/pixel) imager has revealed that some of the low albedo linear features have a corrugated texture, herein referred to as Corrugated Linear Features (CLF), and display other characteristics inconsistent with unconsolidated aeolian sediments (Fig. 3.2B). The goal of this work is to demonstrate that CLF are paleodunes that have been lithified by circulating water.

A further significance of the CLF is that they appear to have been exhumed from beneath an overlying light-toned material, referred to here as the light-toned unit (LTU). LTU covers large areas of West Candor and other Chasmata [e.g. Mangold et al., 2008; Chojnacki and Hynek, 2008]. Dune formation and lithification on the eroded slopes of Ceti Mensa and their subsequent burial by the LTU provides further insight into the sequence of deposition and erosion that shaped Ceti Mensa and Candor Chasma.

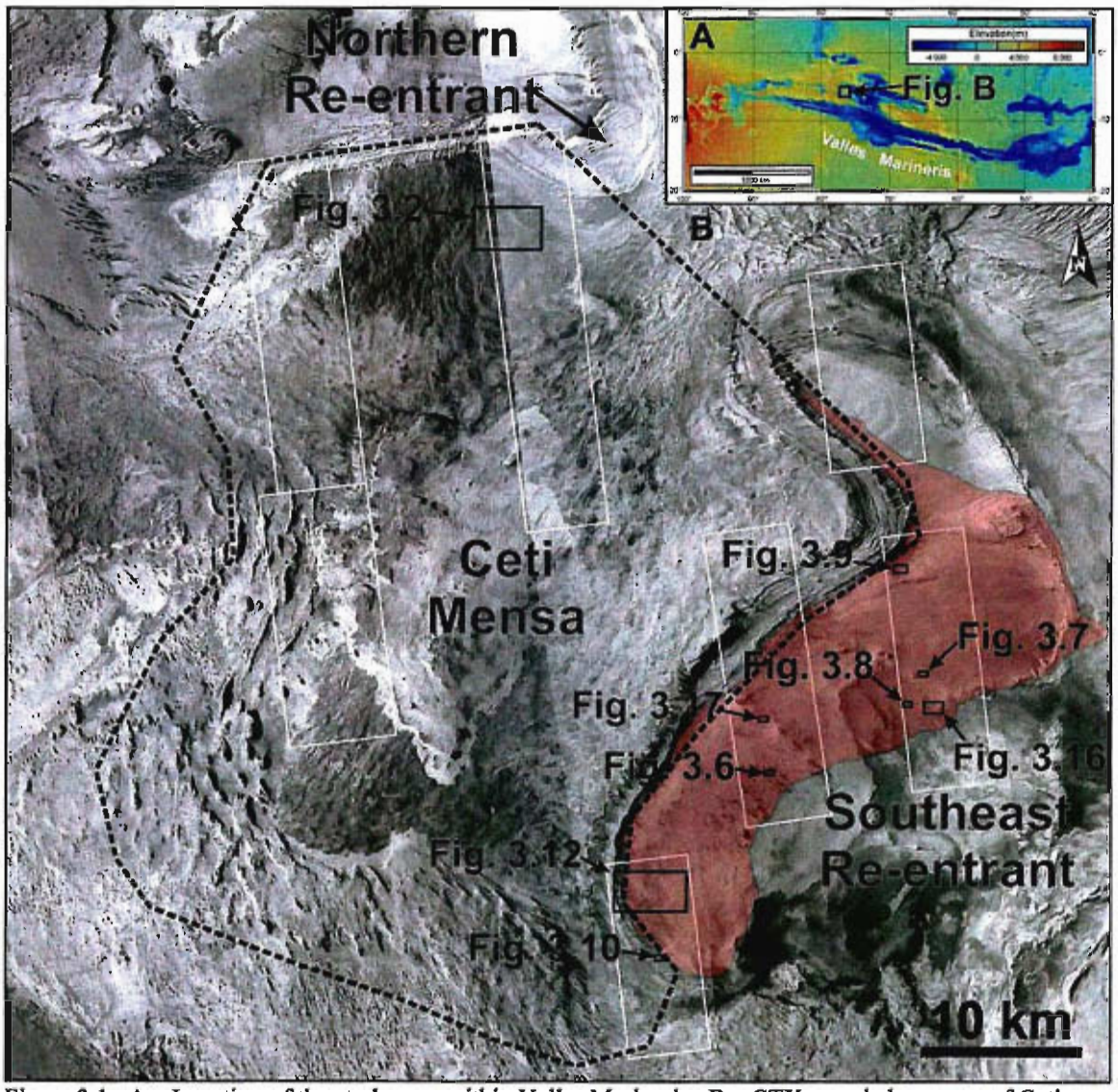

Figure 3.1. A – Location of the study area within Valles Marineris. B – CTX mosaic base map of Ceti Mensa (outlined with dashed black line) with the available HiRISE images outlined in white (not all HiRISE images used in this study are depicted) and figure locations outlined with a solid black line. The features of active dunes depicted in Figures 3.14 and 3.13 are not dependant on location and are therefore not included in this figure. Ceti Mensa covers an area of more than 25, 000 km^2 and reaches heights of more than 5 km above the chasma floor [Lucchitta, 2007; Gaddis et al., 2006]. The red shaded area indicates the extent of the intermediate plateau (~1400 m) along the eastern flank of Ceti Mensa.

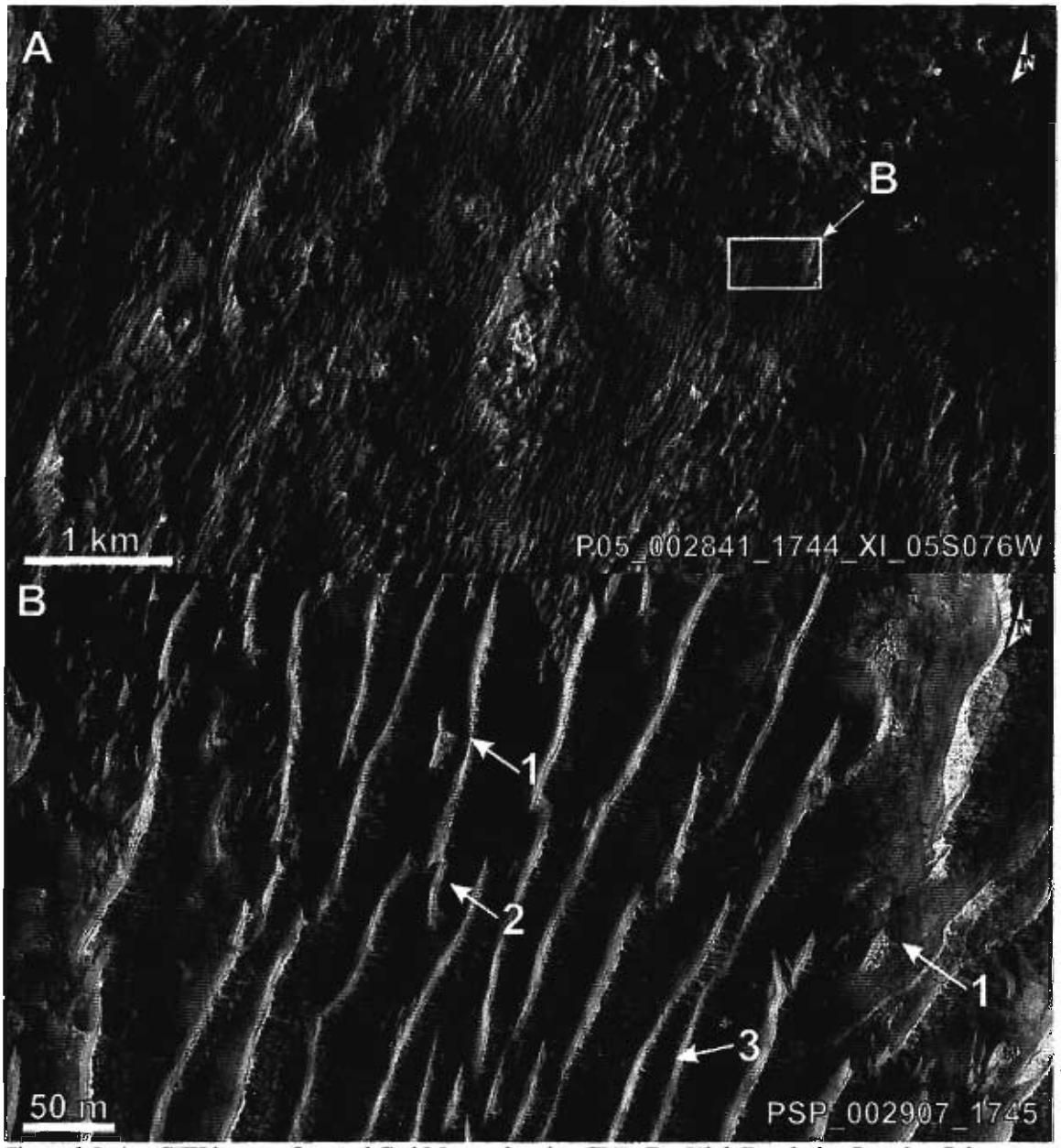

Figure 3.2. A – CTX image of central Ceti Mensa showing CLF. B – High Resolution Imaging Science Experiment (HiRISE) [McEwen et al., 2007] image giving a detailed view of the outlines area and CLF. B illustrates characteristics indicative of indurated materials such as (1) planar fractures, (2) disjointed appearance and the (3) corrugated texture on the east-facing slope.

The abundant deformation structures (faults and fractures) documented within the ILD [e.g. Fueten et al., 2006, 2008; Okubo et al., 2008; Okubo, 2010] and the kilometers-high escarpments they form, suggest these sediments are lithified [Malin and Edgett, 2000]. The material comprising ILD is most likely friable fine grained sediments (sand,

silt and/or clay) that break into small clasts when eroded, as large boulders are not observed at the base of cliffs [Malin and Edgett, 2000]. If the observed competency of the ILD is not a result of sediment lithification but the solidification of layered lavas, large boulders would again be expected to appear below cliffs.

The timing of ILD emplacement has been extensively studied and two general evolutionary timescales have been proposed. A pre-chasma age for ILD (deposition within isolated ancestral basins [Lucchitta and Bertolini, 1989; Witbeck et al., 1991; Lucchitta et al., 1992, 1994; Schultz, 1998; Fueten et al., 2006]) is based on layered deposits visible within the wall rock stratigraphy and limits recent deposition to a thin mantling of aeolian sediments [e.g., Malin and Edgett, 2000, 2001; Catling et al., 2006]. Deposition of ILD during and after normal faulting that linked the ancestral basins into what is now Valles Marineris, is supported by ILD distribution and structural mapping, has gained favor [e.g., Lucchitta, 1990, 1999; Witbeck et al., 1991; Lucchitta et al., 1994; Schultz, 1998; Chapman and Tanaka, 2001; Fueten et al., 2006, 2008; Okubo et al., 2008; Okubo, 2010].

3.1.1 Mineral Distribution

Using data from the Observatoire pour la Mineralogie, L'Eau, les Glaces et l'Activitié (OMEGA) [Bibring et al., 2005, 2006; Poulet et al., 2005; Gendrin et al., 2005] (40 cm/pixel) and Compact Reconnaissance Imaging Spectrometer (CRISM) [Murchie et al., 2007; Mustard et al., 2008] (20 m/pixel), the mineralogy of ILD and the active sediments can be inferred [e.g. Mangold et al., 2008; Murchie et al., 2009]. Both poly- and monohydrated sulfates were found to be large constituents of layered sediments, increasing their overall albedo.

Analysis of OMEGA data [e.g. Mangold et al., 2008; Murchie et al. [2009] determined that kieserite ($MgSO_4 \cdot H_20$), is the best spectral match for the monohydrated sulfate, while the polyhydrated sulfate signature could represent a more varied mineralogy. Spectral analysis of the areas containing CLF determined they were not rich in either pyroxene (unlike active dunes) or sulfates [Mangold et al., 2008]. The formation of poly- and/or monohydrated sulfates requires atmospheric temperatures and pressures in which water is stable, conditions not currently present at the Martian surface. The kieserite may represent either a primary mineral precipitated from a hydrothermal system at the surface [e.g. Geissler et al., 1993], an alteration product of subsurface fluid circulation or dehydration of hydrated minerals during diagenesis at depth [e.g. Warren, 1999].

Conversely, the hydration of the monohydrated phase to produce polyhydrated sulfates is considered a likely mechanism because the polyhydrated forms are more stable at the temperatures present at the Martian surface [Vaniman et al., 2004]. However, observations of the same ILD over a two year period using OMEGA and CRISM data by Roach et al. [2009], did not detect any alteration of monohydrated sulfates to a polyhydrated phase.

3.1.2 Aeolian Processes in Candor Chasma

In the current Martian environment aeolian processes are the dominant forces controlling deposition and erosion in the non-polar regions of Mars. Aeolian landforms representing both deposition and erosion, such as sand dunes, dust mantles, yardangs and scalloped textures are common in many environments including that of West Candor. Aeolian deposition occurs in zones of flow separation (fast air over slow air), such as on

the down-wind side of topographic features (e.g. dunes) [Wiggs et al., 2002]. A critical balance must be struck in order for deposition to occur; the wind velocity must be sufficient to transport grains by saltation but not so strong as to keep grains suspended [Tokano, 2007]. Sand dunes take many forms but their overall morphologies are very similar. The three basic types of dunes that compose the majority of terrestrial sand seas are described by Bridge and Demmico [2008]: transverse (which includes crescentic and barchan dunes), linear and star/pyramidal dunes.

Transverse dunes form where sand supply is limited and the wind direction varies less than 15° [Bridge and Demmico, 2008]. The crestlines of transverse dunes form perpendicular to the essentially unidirectional wind direction, producing the characteristic asymmetric profile. On Earth, crescentic dunes make up 40% of sand seas [Bridge and Demmico, 2008].

Linear dunes form where two (seasonal) wind directions of unequal strength (dominant and subordinate) are active [Tsoar, 1983; Pye and Tsoar, 1990; Lancaster, 1995, 2005; Bristow et al., 2000, 2005], producing a symmetrical to slightly asymmetrical profile with either rounded or sharp crests parallel to the average of the two wind directions (Fig. 3.3). Commonly, smaller dunes are superimposed on the slopes of larger primary dunes by strong currents moving longitudinally along the axis of the primary dune [McKee, 1945; 1957; Sharp, 1963]. The type and orientation of the superimposed dunes are a function of the secondary airflow over the primary dune or a portion of the overall wind regime, such as a subordinate wind direction [Kocurek and Ewing, 2005] (Fig. 3.3).

Linear dunes were initially thought to only migrate downwind, producing cross strata dipping away from the crest in opposite directions [Bagnold, 1941] (Fig. 3.4). It has since been demonstrated that lateral migration also occurs by superimposed transverse dune migration along the flanks of the linear dune, producing smaller cross strata dipping in the same direction as lateral migration [Rubin and Hunter, 1985; Hesp et al., 1989; Rubin, 1990; Bristow et al., 2000, 2005] (Fig. 3.5). The asymmetric wind velocities are thought to be responsible for lateral migration by creating unequal rates of erosion and deposition on either side of the crest. On the lee, where deposition is greater, superimposed dunes are able to form perpendicular to the crestline (dip parallel to the crestline) [Rubin, 1990] (Fig. 3.5). Linear dunes are commonly more than 20 km long (~20 times longer than transverse dunes) and comprise about half of terrestrial sand seas [Bridge and Demmico, 2008].

Star dunes comprise three to four crestlines which meet at a central peak and form in multidirectional wind regimes, such as in the lee of land masses where periodic flow separation occurs. Star dunes are a minor component of terrestrial sand seas at only 8.5% of terrestrial sand seas [Bridge and Demmico, 2008].

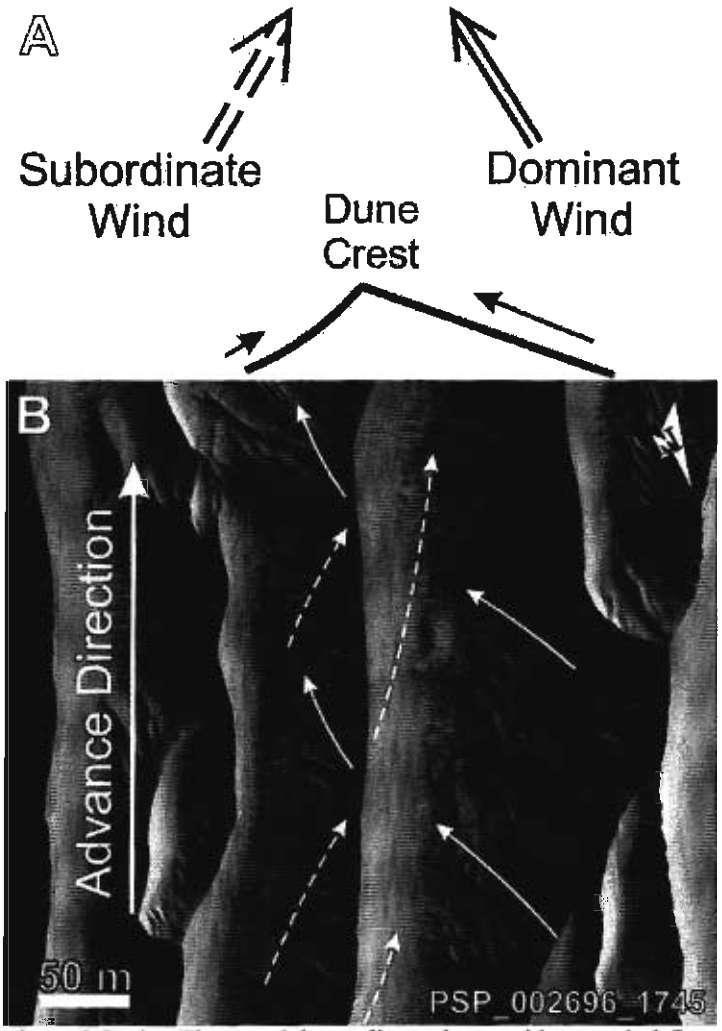

Figure 3.3. A – Flow model over linear dunes with two wind-flow directions of unequal velocity, modified from Bridge and Demmico, [2008]. B – Active primary linear dune migrating downwind from bottom to top (NE to SW) with superimposed transverse dunes forming on the stoss (SE-facing) slope.

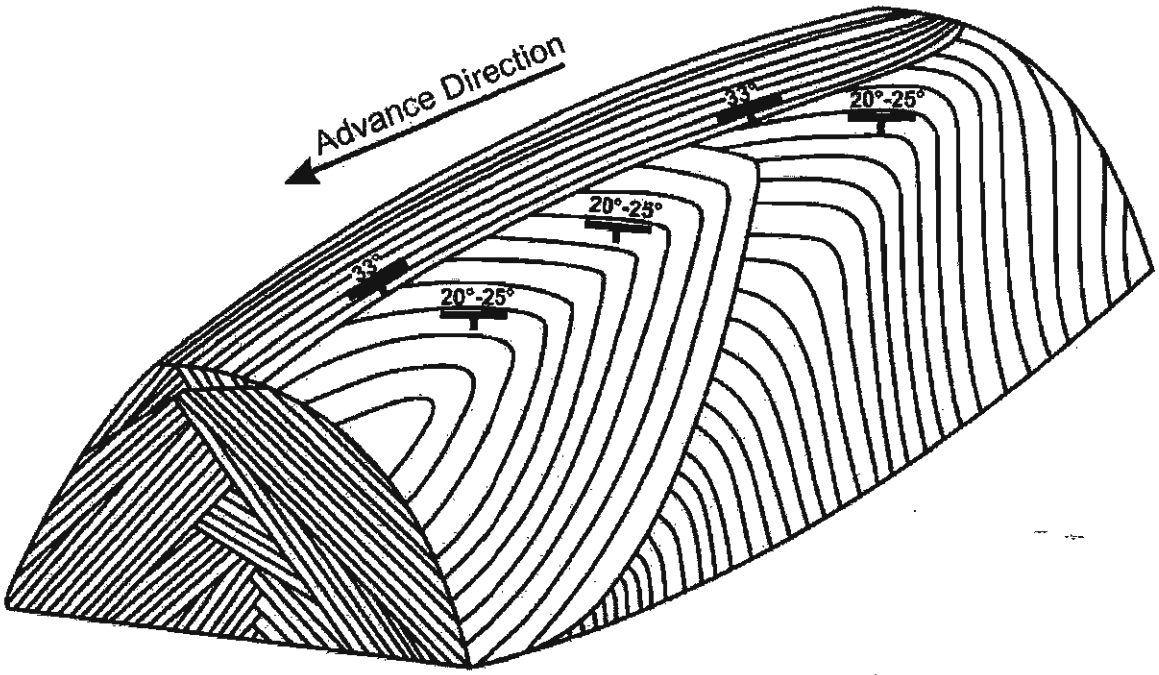

Figure 3.4. Model from Tsoar [1982], illustrating the attitudes of cross strata within linear dunes.

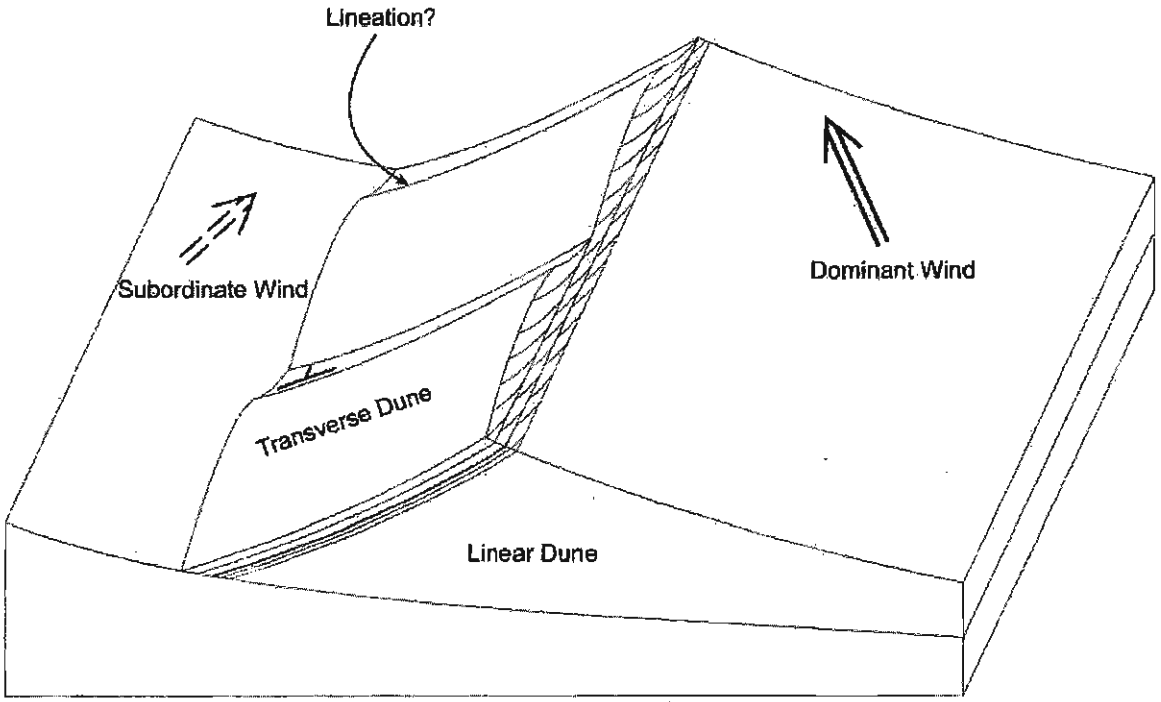

Figure 3.5. Hypothetical model from Rubin and Hunter (1985) illustrating the cross strata produced by climbing transverse dunes on the lee slope of a linear dune, modified from Bridge and Demmico [2008].

Computer modeling of dune field evolution by Werner [1995], has shown that under a consistent wind regime and given enough time, dunes will evolve into larger

well-formed linear dunes with consistent orientations and a minimum number of crest terminations, regardless of the initial conditions (orientation, number and type of dunes present).

The two surfaces of a dune (windward and down-wind) are defined by the dominant process (deposition or erosion) acting upon the surface. The windward surface, where erosion predominates, is the stoss and the down-wind surface, where deposition predominates, is the lee or slip-face.

Erosion by aeolian processes is dominant in areas of increased wind velocity, such as the windward side of topographic features [Greeley et al., 2002], and suspension of particles predominates. Grain size and moisture content of the sediment are also factors when considering the erodibility of a surface [Van Boxel et al., 1999].

Yardangs have positive relief and are erosive features, sculpted from indurated material by wind abrasion into streamlined ridges parallel to the prevailing wind direction with a broad, rounded windward face that gradually gets lower and narrower down-wind (Fig. 3.6; 1) [Bridge and Demmico, 2008]. The scalloped texture likely formed by wind abrasion and is frequently observed on kieserite-rich deposits in Valles Marineris [Chojnacki and Hynek, 2008], indicating that erosion is dominant. This texture is defined by numerous bowl-like (rounded bottom) depressions that overlap, forming polygonal/irregular outlines (Fig. 3.7).

The orientation of the local prevailing winds has been inferred in previous research by these types of erosional features. Chojnacki and Hynek [2008] concluded the prevailing wind direction north of Ceti Mensa is likely east-west based on parallel elongated "fins". However, they do not necessarily represent the current wind regime,

and may in fact represent a paleo wind regime, as their response time is much longer than that of active sediments.

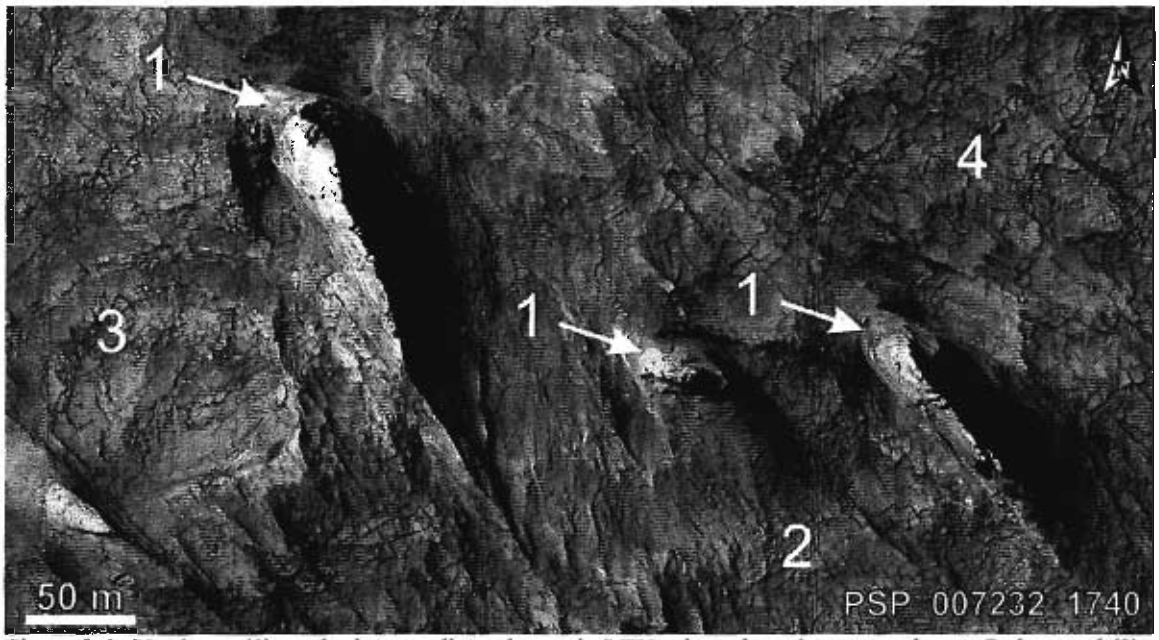

Figure 3.6. Yardangs (1) on the intermediate plateau in LTU oriented northwest-southeast. Orthogonal (2) and polygonal (3 & 4) fractures and scalloping (4) is also visible.

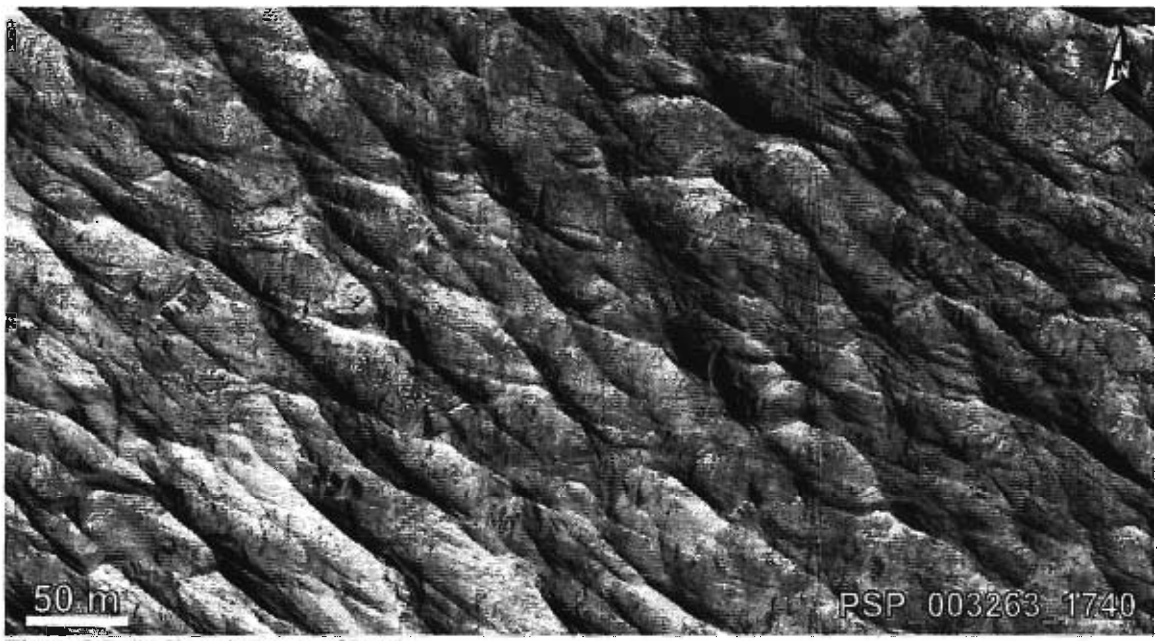

Figure 3.7. Scalloped texture of LTU.

3.2 Methodology

Where available, HiRISE and CRISM data made it possible to examine individual CLF and determine their relationsbip with the LTU. Thirteen HiRISE images, including three stereo image pairs of West and Central Candor Chasma were examined for this study. High-resolution digital terrain models (DTM) were derived from four HiRISE stereo image pairs using the NASA Stereo Pipeline Automated Stereogrammetry Software [Moratto et. al, 2010]. Utilizing the high-resolution DTM, the attitudes of planar features were calculated (e.g. slopes of CLF) and displayed 3D manipulations of the data with Orion structural analysis software (http://www.pangaeasci.com). A plane surface of best fit was computed by placing several points along the observed contact or planar surface and using a multi-linear regression.

The orientations of the yardangs and active primary dunes were measured to determine if the wind regimes they record are reflected by the CLF orientations. The orientations of the different features were measured along a visual line of best fit for the long axis and the direction of the wind determined from the yardangs which narrow in the down-wind direction. No wind direction could be interpreted from the CLF or active primary dunes.

To better understand the material properties of CLF and LTU surfaces, the relative thermal inertia of both were observed using night-time infrared imagery, obtained by the Thermal Emission Imaging System (THEMIS) [Christensen et al., 2004] camera (100 m/pixel), onboard Mars Odyssey. Thermal inertia describes the resistance to a change in temperature throughout the day of the upper few centimeters of a material [Fergason et al., 2006]. The thermal inertia of a material depends on properties such as

density, caloric capacity and most significantly, thermal conductivity [Mellon et al., 2000]. The thermal conductivity of a material depends on several key factors including particle size, porosity [Alvarez et al., 2010], rock abundance, degree of induration and the amount of bedrock within the top few centimeters of the subsurface [Putzig et al., 2005]. The greater surface area of fine grained materials increases thermal conductivity by allowing heat to be absorbed and released, through radiation and conduction, more rapidly than course grained or indurated materials. Overall, thermal inertia increases with increasing particle size and/or degree of induration [Kieffer et al., 1977; Fergason et al., 2006] due to a decrease in thermal conductivity.

3.3 Results

3.3.1 Observations of the Corrugated Linear Features (CLF)

CLF are defined by two exposed surfaces that intersect at the ridge crest and are uniformly aligned approximately northeast-southwest. These surfaces have distinct morphologies. The slopes facing the northwest are smooth with a thin covering of dark mantling material, while the slopes facing the southeast are covered with vertical to inclined lineations producing the corrugated texture (Fig. 3.8).

The southeast-facing slopes (mean =18.6°±2.4° (95% confidence interval), n =15) are generally steeper than the northwest-facing slopes (mean =10.2°±2.6° (95% confidence interval), n =15), producing a slightly asymmetric profile. A characteristic of the CLF are sharp, planar truncations, especially when surrounded by LTU (Fig. 3.9). Small fractures are also observed transecting the CLF and are offset by faults in places (Figs. 3.10 A&B). A further distinguishing feature of the CLF is their extremely low

thermal inertia relative to the surrounding units, including aeolian active dunes (when viewed in night-time infrared imagery) (Fig. 3.11; 2).

CLF bifurcate and merge either along the crestline or from midway through the NW- or SE-facing slope (Fig. 3.8) in a manner similar to that of dunes. Where many divisions occur, the spacing between CLF decreases and they become narrower. CLF also appear to be more resistant than the surrounding LTU as they have a higher relief, possibly indicating a competency contrast between the two materials (Fig. 3.12). The spacing of CLF has a wide range (10–130 m crest-to-crest) and can change abruptly to form discrete regions in which the size and spacing remains consistent (Fig. 3.12).

CLF are present in two areas around Ceti Mensa: on the northern corner and on the intermediate plateau. Both of these locations contain large numbers of CLF that have uniform characteristics but are separated by more than 300 m in elevation and do not appear to represent the same stratigraphic unit. On the shallow slopes of the northern corner of Ceti Mensa, both slopes of some CLF are covered by mantling material which makes distinguishing them from active dunes more difficult and increases their thermal inertia. On the intermediate plateau, the largest concentration of CLF are present near the edge of the plateau and some of them are present on the steeper slopes leading down to the bottom of the re-entrant. The dunes on the steeper slopes of the plateau are quite heavily blanketed by aeolian sediments and a transition zone is evident where sediment cover increases, again with a corresponding increase in thermal inertia.

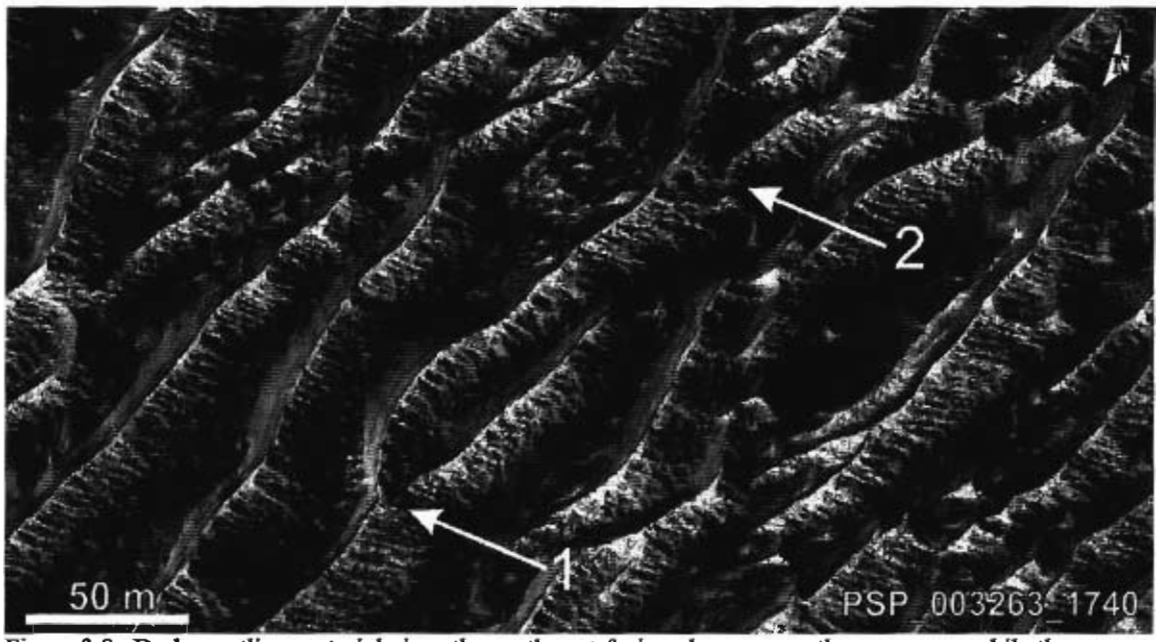

Figure 3.8. Dark mantling material gives the northwest-facing slope a smooth appearance while the southeast-facing slopes have a corrugated texture produced by parallel lineations. CLF bifurcate with a smooth transition (1) from the crestline of (2) from the middle of another feature.

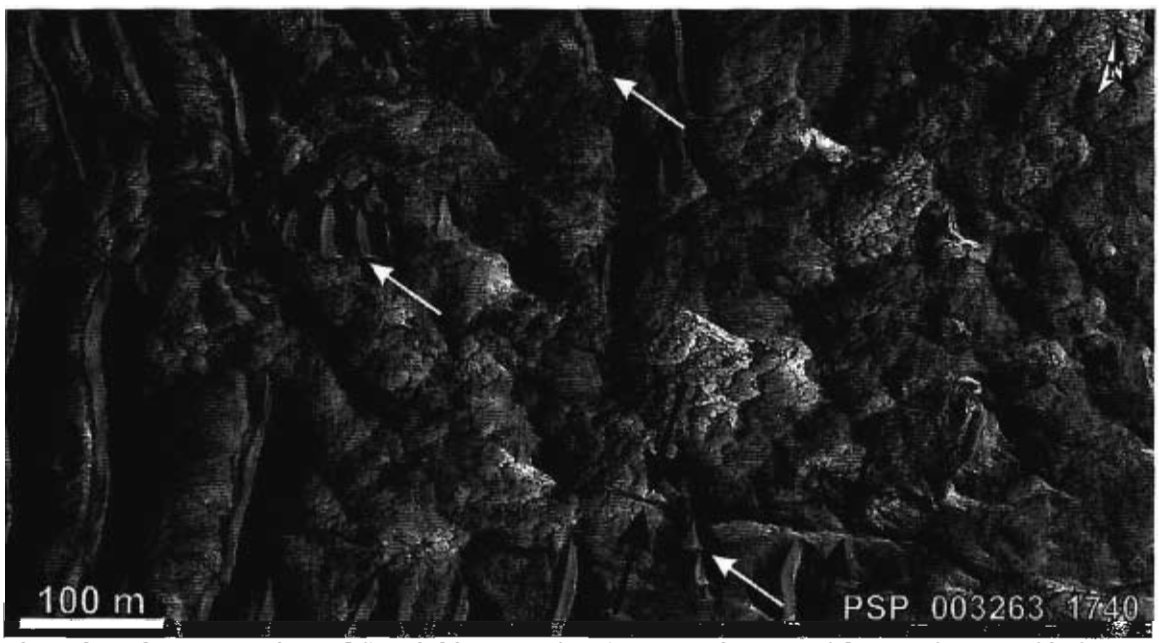

Figure 3.9. Planar truncations of CLF (white arrows) and a transecting curved fracture (between black arrows).

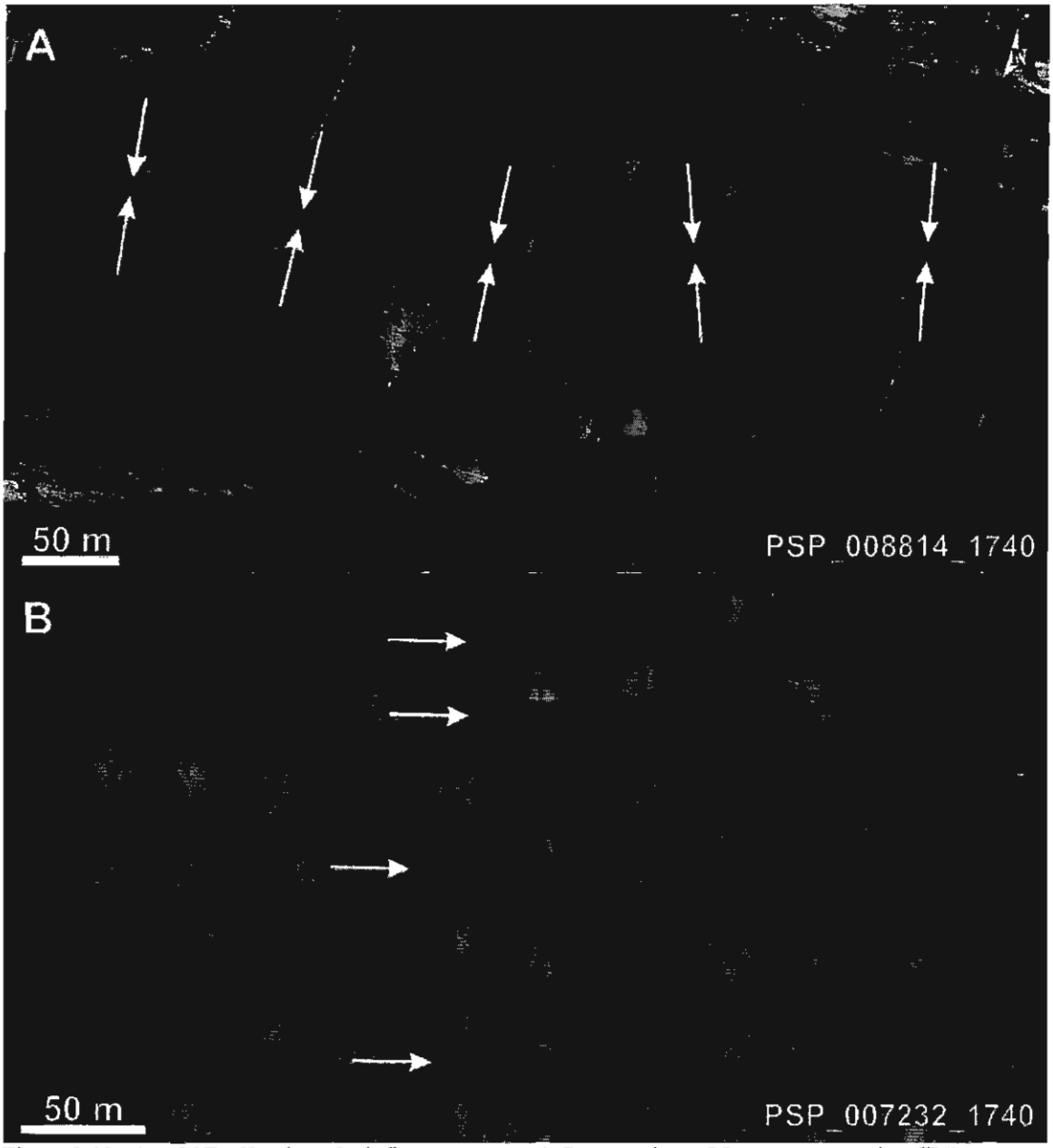

Figure 3.10. A – CLF offset by a fault (between arrows). B – 3D view of fractures truncating CLF (arrows). Vertical exaggeration is 1.

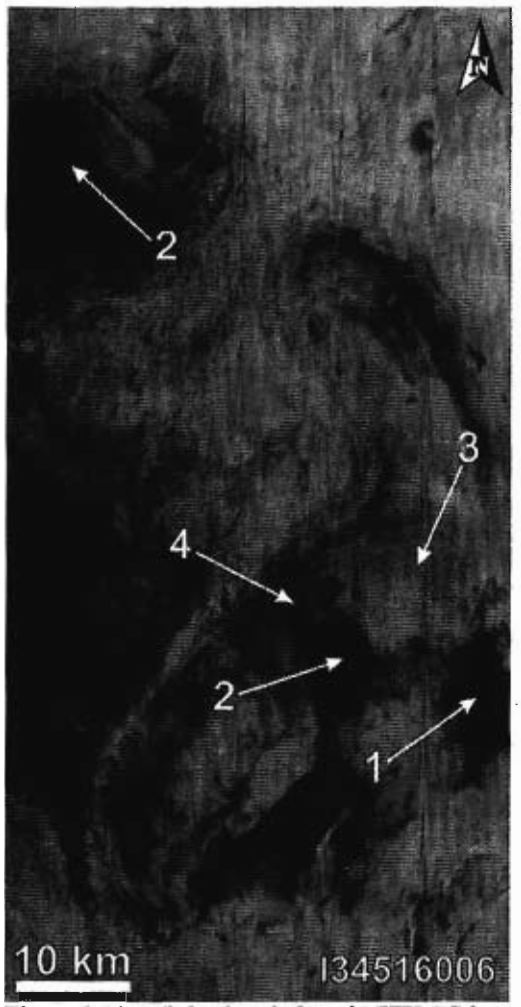

Figure 3.11. Night-time infrared THEMIS image of Ceti Mensa. (1) Region dominated by active aeolian sediments (at least a few centimeters thick). (2) Regions dominated by CLF. (3) LTU dominated by kieserite. (4) LTU dominated by polyhydrated sulfates.

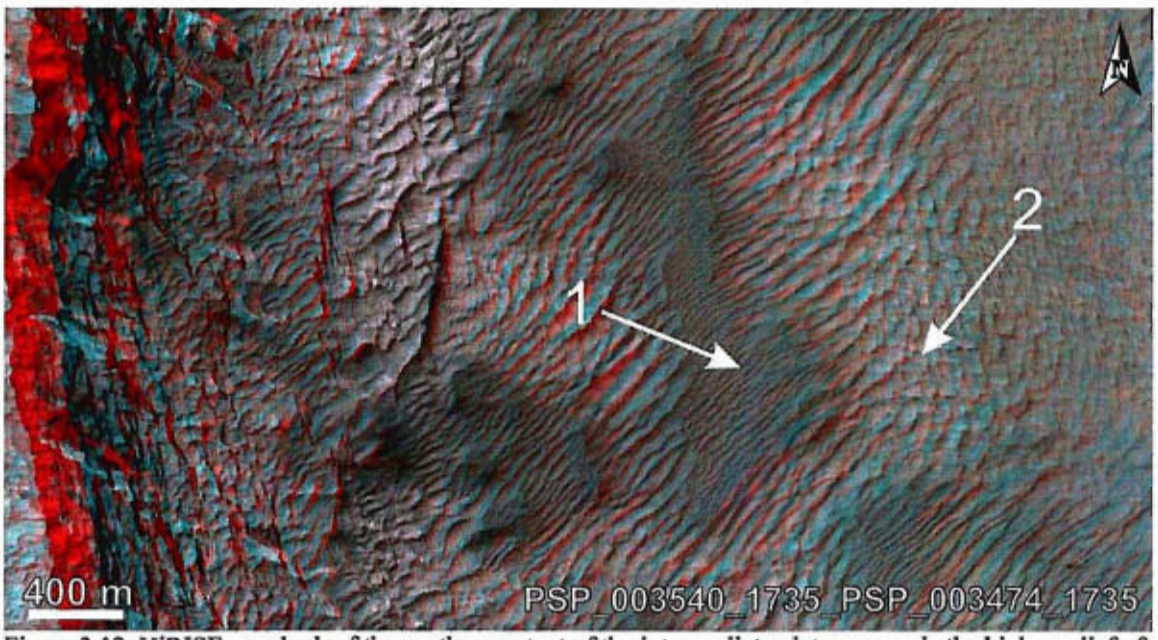

Figure 3.12. HiRISE anaglyph of the southern extent of the intermediate plateau reveals the higher relief of the (1) CLF, relative to the (2) LTU. The range of spacing widths displayed by CLF is also visible.

3.3.2 Active Aeolian Features

The spacing of dunes in the study area ranges from 10–130 m (crest-to-crest) (Fig. 3.13). The observed dunes bifurcate with two subtly different variations, defined by the angle at which they deviate from the original dune crestline - either with a smooth, low angle transition from the crestline (Fig. 3.14; 1), or at a highly oblique angle with a severely curved tail connecting the two crests (Fig. 3.14; 2). The morphology of these dunes is most consistent with that of linear dunes (asymmetry, bifurcation methods, spacing and parallel alignment) and consistent throughout the study area, indicating overall wind regime that is consistent throughout the study area. It is noteworthy to mention that the study area is practically devoid of barchan dunes, unlike terrestrial dune fields which typically contain about 40% barchan dunes [Bridge and Demmico, 2008]. The thermal inertia of aeolian bedforms (Fig. 3.11; 1) is lower (darker) than the LTU (Fig. 3.11; 3&4) but significantly higher (brighter) than that of the CLF fields (Fig. 3.11; 2).

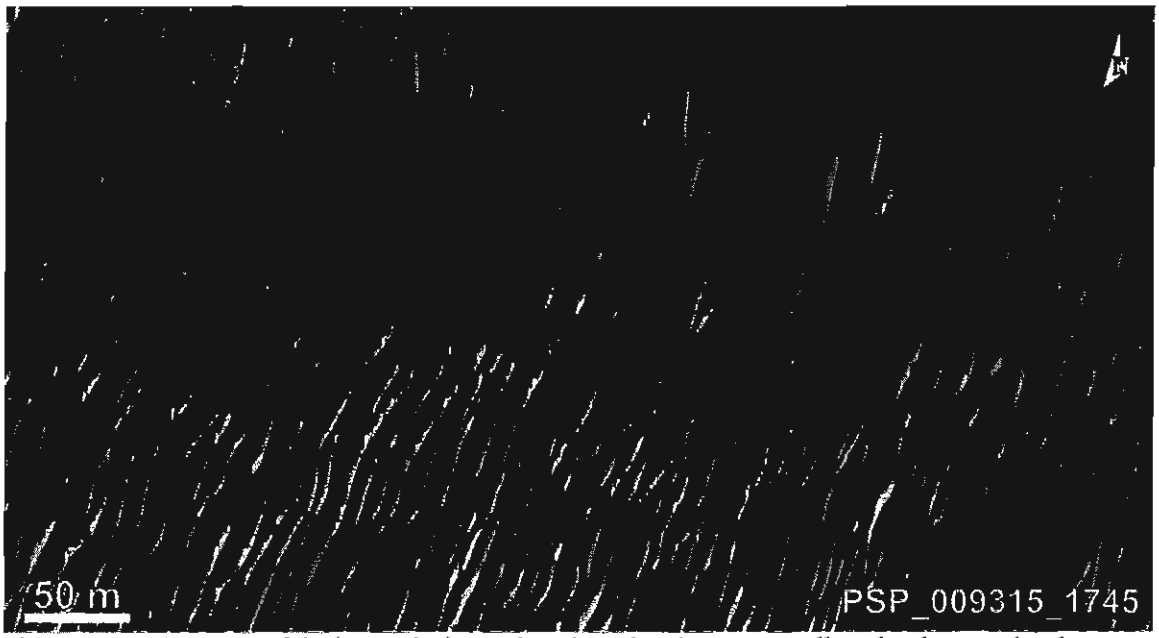

Figure 3.13. The center of the image depicts a sharp boundary between smaller, closely spaced and broader, widely spaced active dunes.

The crestlines of active dunes in West Candor generally have very regular orientations throughout the study area and are aligned approximately northeast-southwest. Smaller dunes are commonly observed on the SE-facing slopes of larger dunes, perpendicular to their crestline, forming compound or complex dunes. Active dunes form abundantly around most of Ceti Mensa, with the exception of the flat-lying intermediate plateau within the southeast re-entrant which contains very little active aeolian sediments (dust mantles in topographic depressions) and erosional features dominate. However, immediately adjacent to the southeast border scarp of Ceti Mensa, a thicker covering of dust is present and obscures the CLF. Dunes do form within the re-entrant but only on the steeper slopes below the intermediate plateau. Where active dunes are present in Candor, they generally have an asymmetric profile with smaller dunes forming on the southeast-facing slopes (Fig. 3.14).

On top of Ceti Mensa, aeolian sediments are more abundant with small superimposed dunes forming on the southeast-facing slopes of the CLF, highly oblique to the crestline. The limited HiRISE coverage does not allow for a close inspection further to the west on Ceti Mensa, where it appears a greater volume of sediment is present.

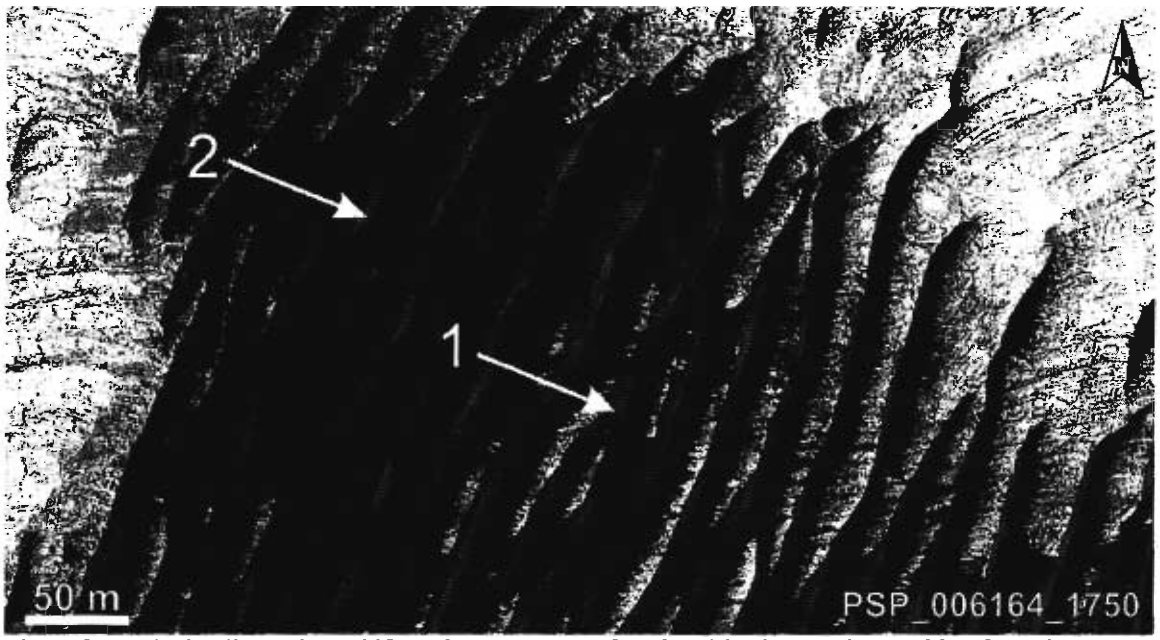

Figure 3.14. Active linear dunes bifurcating at a range of angles; (1) a low angle transition from the crestline of one dune to another, (2) a highly oblique angle with a severely curved tail connecting the two crests. Dune material is streaked across the LTU in the interdunal area and the SE-facing surface is covered by superimposed dunes perpendicular to the axis of the primary dune.

3.3.3 Yardangs

Below the south-eastern border of Ceti Mensa, the orientations of yardangs range from 95–145° and are surrounded by LTU with very little mobile sediment in the vicinity. These orientations indicate the prevailing winds on the intermediate plateau are from the northeast and Ceti Mensa has a minimal effect on the wind direction (Fig. 3.15).

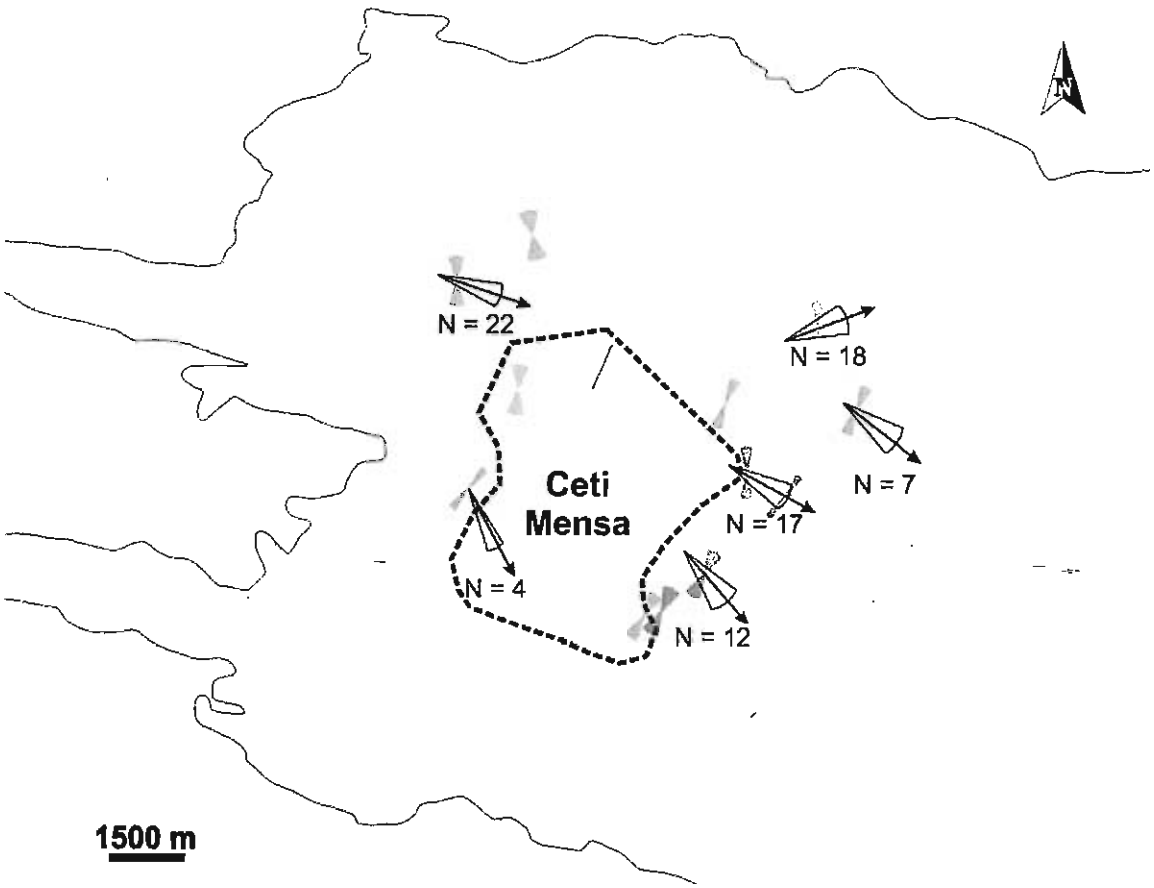

Figure 3.15. A diagrammatic representation of the yardang (black), active dune (grey) and CLF (red) orientations in West Candor. The range of yardang orientations for a given location is presented as a wedge and the number of measurements (N) for each wedge is listed underneath. The downwind direction and the average orientations are shown as arrows. A qualitative representation of the orientation ranges displayed by active dunes (grey) and CLF (red) are depicted by a two-wedge symbol (bow-tie).

3.3.4 Light-Toned Unit (LTU)

The light-toned unit (LTU) that covers the intermediate plateau along the eastern flank of Ceti Mensa, onlaps and fills between individual CLF, sometimes leaving only the top few centimeters of the CLF exposed while completely covering others (Figs. 3.16 A&B). Small orthogonal and polygonal fractures cover some areas of LTU (Fig. 3.17) while others areas are scalloped and scoured smooth by aeolian erosion (Fig. 3.7). The most highly fractured LTU corresponds with the polyhydrated sulfate-rich area identified by Mangold et al. [2008]. However, the characteristic planar truncations of the CLF do not continue into the LTU.

Sharp contacts between LTU and CLF demonstrate the distinct albedo contrast (Fig. 3.16). Layering in the LTU may be present but is difficult to trace because of the low albedo contrast and its highly irregular nature. However, in some areas, what appears to be layering is discernible because it shows greater internal albedo contrast or has been sculpted into terraces.

LTU is also found on top of Ceti Mensa and in the surrounding lowlands. The thermal inertia of the kieserite is relatively high (Fig. 3.11; C), when compared to CLF and active dunes. However, the thermal inertia of the polyhydrated sulfates (Fig. 3.11; D) is lower than the kieserite, almost as low as that of active dunes.

Figure 3.16A. Sharp contact between LTU and CLF material from upper left to lower middle of image. The light-toned unit fills between and eventually covers CLF to the east. Topography slopes from the top right to bottom left.

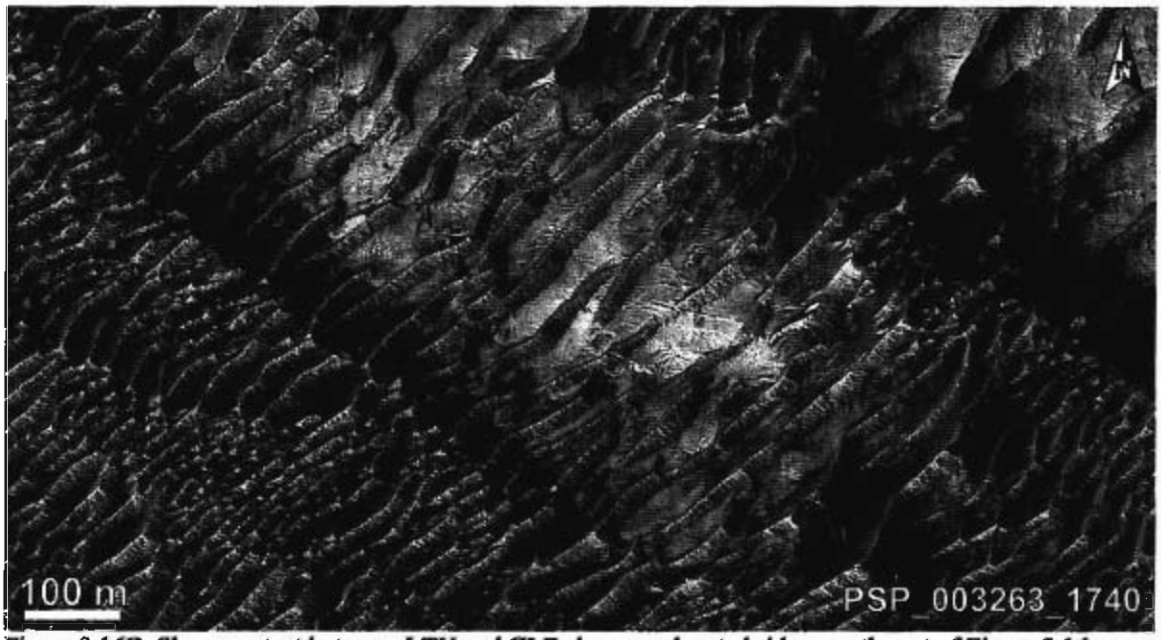

Figure 3.16B. Sharp contact between LTU and CLF along an elevated ridge, northwest of Figure 3.16. Topography slopes from the top right to bottom left.

Figure 3.17. Extensively orthogonally and polygonally fractured LTU filling between the CLF.

3.4 Discussion

Characteristics of CLF, such as their size and the nature in which they bifurcate are similar to characteristics of the aeolian dunes observed in and around the study area (Table 1). Individual linear dunes display a comparable spacing range (10–130 m) to

individual CLF. Both CLF and active dunes will either gradually transition into dunes of a different size or do so abruptly, forming a linear boundary beyond which all the dunes or CLF are of similar size and spacing (Figs. 3.12 & 3.13). The manner in which linear dunes bifurcate either with a smooth transition between crestlines or at a highly oblique angle is also quite similar to the division of CLF (Fig. 3.18). The observed asymmetry of the CLF is also consistent with slightly asymmetric linear dunes (Fig. 3.3) as described by Bridge and Demicco [2008]. In addition, the CLF and the active dunes have remarkably similar and uniform orientations, approximately northeast-southwest.

Table 3.1. List of characteristics displayed by GCT and active aeolian bedforms. Characteristics displayed by the structure are indicated with an X.

Characteristic	CLF	Active Dunes
Bifurcations	X	X
Asymmetry	X	X
Have a range of spacing widths (crest-to-crest)	10 – 130 m	10 – 130 m
Orientation	348° – 46°	327° – 49°
Visibly affected by deformation	X	
Very low thermal inertia	X	
Terminating with a low relief point		X
Corrugated appearance on the southeast slopes	X	X
Partial covering of mantling material	X	

Although the overall morphology of the CLF is consistent with active aeolian dunes, the evidence of brittle deformation, planar fractures and transecting fractures with or without offsets (Figs. 3.9 & 3.10), suggest a competency equal to that of indurated or completely lithified sediments. Planar truncations for example, are not observed in active dunes, likely because of insufficient grain cohesion that does not allow for such planarity. Conversely, dunes terminate by slowly tapering to a low relief point or smoothly

transition into the crestline of another dune. Dunes should be generally unaffected by fracture formation and not display angular offset when faulted. The difference between active dunes and CLF is further highlighted by the accumulations of mantling material that partially obscure the CLF and create a colour and textural contrasts with the southeast-facing slope. Theses contrasts are not observed on active dunes as they are entirely comprised of unconsolidated sediments.

Given the abundance of deformational structures present in the CLF and their conformity with the overall morphology of active dunes, it is likely CLF originated as dunes but were later lithified and deformed in a brittle manner. For the CLF to retain the characteristics of active dunes, it is necessary that they were either rapidly stabilized or buried, and possibly lithified, to avoid erosion and the destruction of their characteristic dune morphology. Stabilization may have occurred by sediment saturation and cementation which is supported by the work of Lucchitta [2010], who proposed a low-level lake covering West Candor after Ceti Mensa was isolated. Lucchitta [2010] also anticipated a maximum depth on the order of 1000 m, based on benches at 1400 – 2000 m elevation along the wall rock in the southwest of the chasma which are similar in appearance to strandlines. In agreement with these findings, water to an elevation of 2000 m is approximately the level necessary to completely cover all of the CLF below the southeast border of Ceti Mensa. However, the CLF on top of Ceti Mensa are at an elevation of ~3100 m and could not have been lithified if the water only reached 2000 m. Groundwater percolation is a possible agent stabilizing and/or cementing the CLF at the summit of Ceti Mensa, likely during the same period the large lakes in Candor were

present. It is also possible that all of the CLF were stabilized by freezing or circulating subsurface water and large lakes are not necessary to avoid erosion.

The presence of kieserite and CLF along the intermediate plateau may indicate that it was formed after the formation of Ceti Mensa proper and subsequent isolation by either erosion or chasma floor collapse. The circulation of water in this area, as proposed by previous authors [e.g. Geissler et al., 1993; Bibring et al., 2007], is conducive to the formation of kieserite and cementing aeolian material.

The corrugated texture on the southeast-facing slopes may be the expression of internal structures (cross-strata), exposed and accentuate by erosion, resulting from linear dune formation or related to superimposed dunes. The orientation and regular spacing of the corrugations is consistent with cross-strata in linear dunes dipping parallel to the direction of lateral migration (Fig. 3.4). The exposure of the corrugations only on the SE-facing slopes may be due to deposits of mantling material that cover the NW-facing slopes, obscuring any corrugations that may be present.

Alternatively, the corrugations may be the result of cross strata formed by superimposed transverse dunes on the SE-facing slopes of the primary linear paleodunes (Fig. 3.5). This interpretation is consistent with the fact that superimposed dunes form almost exclusively on the SE-facing slopes of active dunes and share similar spacing to that of the corrugations (Fig. 3.18). Regardless of whether the lineations are the product of primary dune or superimposed dune formation, the expression of internal structures as lineations further suggests the CLF are lithified.

The morphology (Symmetry, bifurcation method, parallel alignment, spacing and internal structures) of the CLF is most consistent with that of linear dunes and likely

formed under similar wind regimes, although they cannot be reconciled with the wind direction indicated by the yardangs. This may indicate the yardangs formed under wind regime independent of those which formed the CLF and active liner dunes.

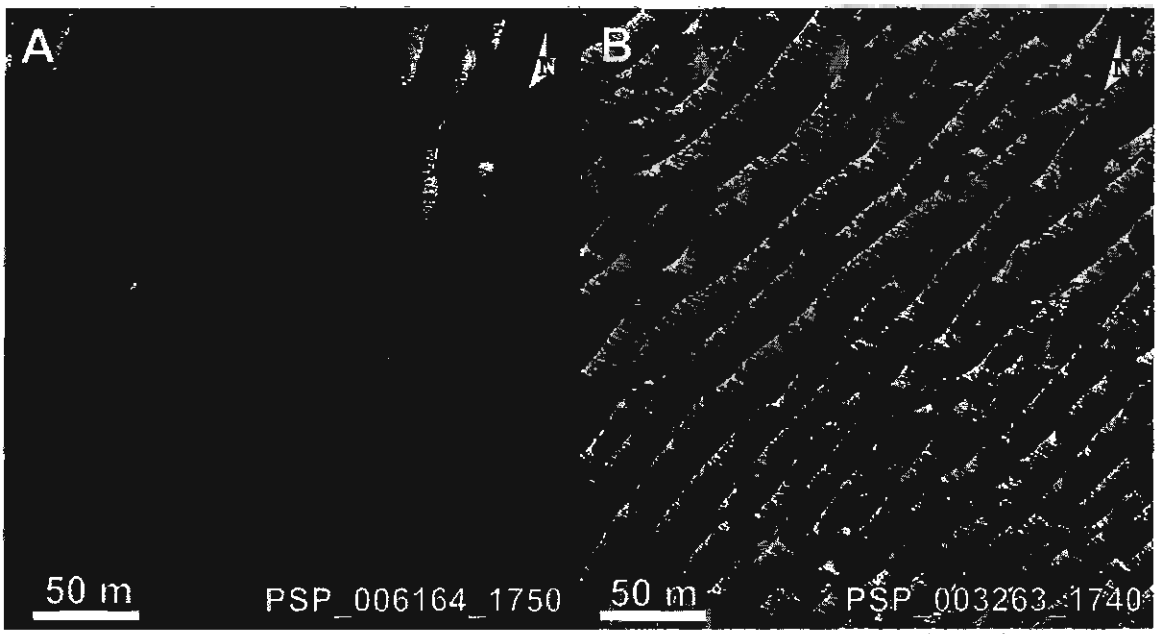

Figure 3.18. Comparison of A – active superimposed dunes on active linear dunes in the northwest of the study area and B – corrugated texture on CLF.

Edgett and Malin [2000] described lithified/fossilized dunes with a "ridged-and-grooved" texture in the Herschel Basin, similar to the corrugated texture on the CLF in our study area, but no further similarities were evident. They interpret the "ridged-and-grooved" texture to be a result of aeolian erosion that scoured and plucked grain-sized material. They, however, did not speculate on the process that lithified the dunes. As the CLF are made up almost exclusively of linear dune morphology (i.e. the absence of lithified barchanoid or crescentic shapes) with highly regular orientations, it can be inferred that the original dune field was mature and/or the sediment supply was abundant when it was lithified. The same can be said for the active dunes in the study, as they share these characteristics.

As previously stated, the material properties of the CLF determine the thermal inertia but cannot be conclusively resolved at the resolution of the current instrumentation (HiRISE, CRISM, THEMIS, etc.). However, it is possible to speculate about the most likely cause(s), based on the factors that affect thermal conductivity and the attributes visible at the available resolutions, assuming they are comprised of materials similar to the surrounding features (i.e. similar mineralogy, density and caloric capacity). Compared to that of the active dunes in the area, the thermal inertia of the CLF is surprisingly low for a lithified material, as thermal inertia usually increases with increasing induration. This fact suggests that the thermal inertia of the CLF was even lower before induration or that the CLF are poorly lithified. It is also possible that induration of the material reduced the pore radius, thereby increasing the thermal conductivity and decreasing thermal inertia.

As previously mentioned, there is a general positive correlation between grain size and thermal inertia, as fine grained materials conduct heat more efficiently and increases thermal conductivity, which may imply the CLF are composed of finer grained material than the active dunes. A covering of fine grained material a few centimeters thick can also reduce the detected thermal inertia of the underlying unit. However, it is not likely the lower thermal inertia of the CLF is the result of a fine dust covering as other materials covered by visibly similar dust do not have comparable thermal inertias. Furthermore, the area in which CLF are located is subject to predominantly erosional forces and lacks large accumulations of mantling material. This interpretation may also be supported by their low albedo (although not as low as active dunes).

The predominance of erosion below the southeast border of Ceti Mensa further bolsters the interpretation that the CLF are lithified and more competent than the LTU, as unconsolidated sediments would otherwise have been removed. The relationship between kieserite and actively eroding surfaces noted by Mangold et al. [2008] is also consistent with our interpretation of the intermediate plateau being dominated by erosion. The heavily eroded appearance of the LTU below the southeast border suggests a large volume of LTU has been removed by the existing wind regime. The polygonal fractures on the LTU are also significant because it shows that the LTU is also at least partially indurated and is not merely a recent deposit of windblown sediments.

The onlapping of LTU onto CLF, together with the absence of deformation representing the same period of deformation which produce the planar truncations of the CLF, may indicate the LTU was deposited after the Formation, lithification and initial deformation of the CLF. The presence of CLF beneath the LTU implies significant changes in the depositional environment after Ceti Mensa had been isolated. Given the conditions under which kieserite formation is possible, together with the lithification of dunes, the idea of circulating water in West Candor is further supported. Dunes would have been formed when the intermediate plateau was dry (they may have been coastal dunes on the edge of a large lake in the southeast re-entrant), but were later stabilized and indurated before they could be eroded.

The northeast-southwest orientation of the active dunes and the almost exclusive formation of superimposed dunes on the southeast-facing slopes indicate that the current dominant wind direction is from the north and the subordinate wind from the northeast. The orientations of yardangs below Ceti Mensa's south-eastern border (95–145°) indicate

they were formed when the prevailing winds were from the northwest and therefore are not in equilibrium with the current wind regime. The orientation of the CLF and the lineations visible on their southeast-facing slopes suggests that the CLF formed under a wind regime similar to the present and not that which sculpted the yardangs.

3.5 Conclusion

Given the similarities between the CLF and active dune morphology, and the evidence for brittle deformation, it is reasonable to suggest that the CLF originated as aeolian bedforms but have subsequently been lithified and deformed in a brittle manner. The thermal inertia of the CLF and active dunes in THEMIS night-time infrared imagery further suggest a disparity in the material properties of the two deposits which could be the result of diagenesis. The strongly eroded nature of the LTU and the on-lapping relationship with indurated aeolian deposits (dunes) indicates that the LTU was deposited after the aeolian deposits and the contact between them represents an unconformity in the stratigraphic sequence. Having shown that the lithified dunes (CLF) formed after Ceti Mensa became a high-standing remnant, and the subsequent formation of the LTU, given the environments in which kieserite forms, it can be stated that water was present at the surface or circulating in the subsurface in the relatively recent past.

3.6 References

Alvarez, F. X., Jou, D., Sellitto, A., 2010. Pore-size dependence of the thermal conductivity of porous silicon: A phonon hydrodynamic approach. Applied Physics Letters, 97, 033103, doi:10.1063/1.3462936

Bagnold, R. A., 1973. The physics of blown sand and desert dunes. Chapman and Hall, London, 265 pp.

Bibring, J.-P., Langevin, Y., Gendrin, A., Gondet, B., Poulet, F., Berthé, M., Soufflot, A., Arvidson, R., Mangold, N., Mustard, J., Drossart, P., the OMEGA team, 2005. Mars surface diversity as revealed by the OMEGA/Mars Express observations. Science, 307, 1576 – 1581, doi:10.1126/science.1108806.

Bibring, J.-P., et al. 2006. Global mineralogical and aqueous Mars history derived from OMEGA/Mars Express data. Science, 312, 400 – 404, doi:10.1126/science.1122659.

Bibring, J.-P., Arvidson, R. E., Gendrin, A., Gondet, B., Langevin, Y., Le Mouelic, S., Mangold, N., Morris, R. V., Mustard, J. F., Poulet, F., Quantin, C., Sotin, C., 2007. Coupled ferric oxides and sulfates on the Martian surface. Science, 317, 1206–1210.

Bourke, M.C., Bullard, J., Barnouin-Jha, O., 2004. Aeolian sediment transport pathways and aerodynamics at troughs on Mars. J. Geophys. Res., (Planets) 109 (E7). doi:10.1029/2003JE002155.

Bridge, J. S., Demicco, R. V., 2008. Earth surface processes, landforms and sediment deposits. Cambridge University Press, New York, 830 pp.

Bristow, C. S., Bailey, S. D., & Lancaster, N. 2000. The sedimentary structures of linear sand dunes. Nature 406, 56–59.

Bristow, C. S., Lancaster, N., & Duller, G. A. T. 2005. Combining ground penetrating radar surveys and optical dating to determine dune migration in Namibia. Journal of the Geological Society of London 162, 315–321.

Catling, D.C., Wood, S.E., Leovy, C., Montgomery, D.R., Greenberg, H.M., Glein, C.R., Moore, J.M., 2006. Light-toned layered deposits in Juventae Chasma, Mars. Icarus, 181, 26–51. doi:10.1016/j.icarus.2005.10.020.

Chapman, M. G., 2002. Layered, massive, and thin sediments on Mars: Possible Late Noachian to Late Amazonian tephra? In: Volcano-Ice Interactions on Earth and Mars.

Smellie, J. L. and Chapman, M. G. (Eds.). Geol. Soc. Spec. Publ., London, 202, 273–203.

Chapman, M.G., Tanaka, K.L., 2001. Interior trough deposits on Mars: Subice volcanoes? J. Geophys. Res., 106, 10087–10100. doi:10.1029/2000JE001303.

Chojnacki, M., Hynek, B.M., 2008. Geological context of water-altered minerals in Valles Marineris, Mars. J. Geophys. Res. 113, E12005. doi:10.1029/2007JE003070 Res.

Christensen, P.R., Jakosky, B., Kieffer, H.H., Malin, M.C., McSween, H.Y., Nealson, K., Mehall, G.L., Silverman, S.H., Ferry, S., Caplinger, M., Ravine, M., 2004. The Thermal Emission Imaging System (THEMIS) for the Mars 2001 Odyssey mission. Space Sci. Rev. 110, 85–130.

Clarke, J. D. A., Bourke, M. C., 2009. Recognition criteria of spring deposits on Mars at all scales: Evidence from the Dalhousie Springs analog (Australia). Lunar and Planet. Sci. XL, Abstract #1102.

Edgett, K.S., Malin, M.C., 2000a. The new Mars of MGS MOC: ridged layered geologic units (They're Not Dunes). Lunar and Planet. Sci. XXXI, Abstract #1057.

Edgett, K.S., Malin, M.C., 2000b. Examples of Martian sandstone: indurated, lithified, and cratered eolian dunes in MGS images. Lunar and Planet. Sci. XXXI, Abstract #1071.

Fergason, R.L., Christensen, P.R., Kieffer, H.H., 2006. High-resolution thermal inertia derived from the Thermal Emission Imaging System (THEMIS): Thermal model and applications. J. Geophys. Res. 111, doi:10.1029/2006JE002735.

Fueten, F., Stesky, R., MacKinnon, P., Hauber, E., Gwinner, K., Scholten, F., Zegers, T., Neukum, G., 2006. A structural study of an interior layered deposit in southwestern Candor Chasma, Valles Marineris, Mars, using high resolution stereo camera data from Mars Express. Geophys. Res. Lett., 33. L07202. doi:10.1029/2005GL025035.

Fueten, F., Stesky, R., MacKinnon, P., Hauber, E., Gwinner, K., Scholten, F., Zegers, T., 2008. Stratigraphy and structure of interior layered deposits in west Candor Chasma, Mars, from High Resolution Stereo Camera (HRSC) stereo imagery and derived elevations. J. Geophys. Res., 113, doi:10.1029/2007JE003053.

Gaddis, J., Skinner, T., Hare, R., Kirk, T., Titus, L., Weller, G.N., HRSC Co-Investigator Team, U.S. Geological Survey, Astrogeology Program, 2006. Morphology and

morphometry of Ceti Mensa, west Candor chasma, Mars. Lunar and Planet. Sci. XXXVII, Abstract #2076.

Geissler, P. E., Singer, R. B., Komatsu, G., Murchie, S., Mustard, J., 1993. An unusual spectral unit in west Candor Chasma: Evidence for aqueous or hydrothermal alteration in the Martian canyons, Icarus, 106, 380– 391, doi:10.1006/icar.1993.1179.

Gendrin, A., Mangold, N., Bibring, J.-P., Langevin, Y., Gondet, B., Poulet, F., Bonello, G., Quantin, C., Mustard, J., Arvidson, R., LeMouélic, S., 2005. Sulfates in Martian layered terrains: The OMEGA/Mars Express view. Science, 307, 1587–1591, doi:10.1126/science.1109087.

Greeley, R., Bridges, N.T., Kuzmin, R.O., Laity, J.E., 2002. Terrestrial analogs to wind-related features at the Viking and Pathfinder landing sites on Mars. J. Geophys. Res. (Planets) 107 (E12).

Hesp, P., Hyde, R., Hesp, V., & Zengyu, Q. 1989. Longitudinal dunes can move sideways. Earth Surface Processes and Landforms 14, 447–451.

Hynek, B. M., Phillips, R. J., Arvidson, R. E., 2003. Explosive volcanism in the Tharsis region: Global evidence in the Martian record. J. Geophys. Res., 108(E9), 5111, doi:10.1029/2003JE002062.

Kieffer, H.H., Martin, T.Z., Peterfreund, A.R., Jakosky, B.M., Miner, E.D., Palluconi, F.D., 1977. Thermal and albedo mapping of Mars during the Viking primary mission. J. Geophys. Res. 82, 4249–4291.

Kocurek, G., Ewing, R.C., 2005. Aeolian dune field self-organization — implications for the formation of simple versus complex dune-field patterns. Geomorphology 72, 94–105.

Komatsu, G., Ori, G. G., Ciarcelluti, P., Litasov, Y. D., 2004. Interior layered deposits of Valles Marineris, Mars: Analogous subice volcanism related to Baikal Rifting, Southern Siberia. Planet. Space Sci., 52, 167– 187.

Lancaster, N. 1995. Geomorphology of Desert Dunes. London: Routledge.

Lancaster, N. 2005. Aeolian processes. In Encyclopedia of Geology 4 (Eds. R. C. Selley, R. L. M. Cocks, & I. R. Plimer), pp. 612–627. Oxford: Elsevier.

Lucchitta, B. K., 1987. Recent mafic volcanism on Mars. Science., 235, 565–567.

Lucchitta, B.K., 1990. Young volcanic deposits in the Valles Marineris, Mars. Icarus, 86, 476–509. doi:10.1016/0019-1035(90)90230-7.

Lucchitta, B.K., 1999. Geologic Map of Ophir and Central Candor Chasmata MTM-05072 of Mars. US Geological Survey, Geologic Investigations Series Map I-2568.

Lucchitta, B.K., 2004. A volcano composed of light-colored layer deposits on the floor of Valles Marineris. Lunar and Planet. Sci. XXXV, Abstract #1881.

Lucchitta, B. K., 2007. Multiple erosional and depositional episodes in West Candor Chasma, Mars. Lunar and Planet. Sci. XXXVIII, Abstract #2093.

Lucchitta, B.K., 2010. Lakes in Valles Marineris. In: Lakes on Mars. Cabrol, N. A., Grin, E.A. (Eds.). Elsevier, pp. 111-162.

Lucchitta, B.K., Bertolini, L.M., 1989. Interior structures of Valles Marineris. In: Lunar and Planet. Sci. XX Proceedings, 590–591.

Lucchitta, B.K., McEwen, A.S., Clow, G.D., Geissler, P.E., Singer, R.B., Schultz, R.A., Squyres, W.W., 1992. The canyon system on Mars. In: Mars, Kieffer, H.H., Jakosky, B.M., Snyder, C.W., Matthews, M.S. (Eds.). Univ. of Arizona Press, Tucson, pp. 453–492.

Lucchitta, B.K., Isbell, N.K., Howington-Kraus, A., 1994. Topography of Valles Marineris: Implications for erosional and structural history. J. Geophys. Res., 99(E2), 3783–3798.

Malin, M.C., Edgett, K.S., 2000. Sedimentary rocks of early Mars. Science, 290, 1927–1937. doi:10.1126/science.290.5498.1927.

Malin, M.C., Edgett, K.S., 2001. Mars Global Surveyor Mars Orbiter Camera: Interplanetary cruise through primary mission. J. Geophys. Res., 106(E10), 23429–23570. doi:10.1029/2000JE001455.

Malin, M.C., Bell III, J.F., Cantor, B.A., Caplinger,M.A., Calvin,W.M., Clancy, R.T., Edgett, K.S., Edwards, L., Haberle, R.M., James, P.B., Lee, S.W., Ravine, M.A., Thomas, P.C., Wolff, M.J., 2007. Context camera investigation on board the Mars Reconnaissance Orbiter. J. Geophys. Res., 112, doi:10.1029/2006JE002808.

Mangold, N., Gendrin, A., Gondet, B., LeMouelic, S., Quantin, C., Ansan, V., Bibring, J.-P., Langevin, Y., Masson, P., Neukum, G., 2008. Spectral and geological study of the sulfate-rich region of West Candor Chasma, Mars. Icarus, 194, 519– 543, doi:10.1016/j.icarus.2007.10.021.

McEwen, A.S., Eliason, E.M., Bergstrom, J.W., Bridges, N.T., Hansen, C.J., Delamere, W.A., Grant, J.A., Gulick, V.C., Herkenhoff, K.E., Keszthelyi, L., Kirk, R.L., Mellon, M.T., Squyres, S.W., Thomas, N., Weitz, C.M., 2007. Mars Reconnaissance Orbiter's High Resolution Imaging Science Experiment (HiRISE). J. Geophys. Res., 112, E05S02, doi:10.1029/2005JE002605.

McKee, E. D., Douglass, J. R., 1971. Deformation of Lee-Side Laminae in Aeolian Dunes. Geol. Soc. Amer. Bull., 82, 359-378.

McKee, E. D., 1945. Small-scale structures in the Coconino sandstone in northern Arizona. J. Geol., 53, 313-325.

McKee, E. D., 1957, Primary structure in some recent sediments: Amer. Assoc. Petroleum Geologists Bull., 41, 1704-1742.

Mellon, M.T., Jakosky, B.M., Kieffer, H.H., Christensen, P.R., 2000. Highresolution thermal inertia mapping from the Mars Global Surveyor Thermal Emission Spectrometer. Icarus 148, 437–455.

Moratto, Z. M., Broxton, M. J., Beyer, R. A., Lundy, M., Husmann, K., 2010. Ames Stereo Pipeline, NASA's Open Source Automated Stereogrammetry Software. Lunar and Planet. Sci. XXXXI, Abstract #2364.

Murchie, S., Arvidson, R., Bedini, P., Beisser, K., Bibring, J.-P., Bishop, J., Boldt, J., Cavender, P., Choo, T., Clancy, R. T., Darlington, E. H., Des Marais, D., Espiritu, R., Fort, D., Green, R., Guinness, E., Hayes, J., Hash, C., Heffernan, K., Hemmler, J., Heyler, G., Humm, D., Hutcheson, J., Izenberg, N., Lee, R., Lees, J., Lohr, D., Malaret, E., Martin, T., McGovern, J. A., McGuire, P., Morris, R., Mustard, J., Pelkey, S., Rhodes, E., Robinson, M., Roush, T., Schaefer, E., Seagrave, G., Seelos, F., Silverglate, P., Slavney, S., Smith, M., Shyong, W.-J., Strohbehn, K., Taylor, H., Thompson, P., Tossman, B., Wirzburger, M., Wolff5, M., 2007. Compact Reconnaissance Imaging Spectrometer for Mars (CRISM) on Mars Reconnaissance Orbiter (MRO). J. Geophys. Res., 112, E05S03, doi:10.1029/2006JE002682.

Murchie, S.L., Roach, L.H., Seelos, F.P., Milliken, R.E., Mustard, J.F., Arvidson, R.E., Wiseman, S.M., Lichtenberg, K.A., Andrews-Hanna, J.C., Bibring, J.-P., Bishop, J.L., Parente, M., Morris, R.V., 2009. Evidence for the origin of layered deposits in Candor Chasma, Mars, from mineral composition and hydrologic modeling. J. Geophys. Res., 114, E00D05, doi:10.1029/2009JE003343.

Mustard, J. F., Murchie, S. L., Pelkey, S. M., Ehlmann, B. L., Milliken, R. E., Grant, J. A., Bibring, J.-P., Poulet, F., Bishop, J., Noe Dobrea, E., Roach, L., Seelos, F., Arvidson, R. E., Wiseman, S., Green, R., Hash, C., Humm, D., Malaret, E., McGovern, J. A., Seelos, K., Clancy, T., Clark, R., Marais, D. D., Izenberg, N., Knudson, A., Langevin, Y., Martin, T., McGuire, P., Morris, R., Robinson, M., Roush, T., Smith, M., Swayze, G., Taylor, H., Titus, T., Wolff, M., 2008. Hydrated silicate minerals on Mars observed by the CRISM instrument on MRO. Nature, 454, 305–309, doi:10.1038/nature07097.

Nedell, S. S., Squyres, S. W., Andersen, D. W., 1987. Origin and evolution of the layered deposits in the Valles Marineris, Mars. Icarus, 70, 409–441.

Okubo, C. H., 2010. Structural geology of Amazonian-aged layered sedimentary deposits in southwest Candor Chasma, Mars. Icarus, 207, 210-225.

Okubo, C.H., Lewis, K.W, McEwen, A.S., Kirk, R.L., 2008. Relative age of interior layered deposits in southwest Candor Chasma based on high-resolution structural mapping. J. Geophys. Res., 113, E12002, doi:10.1029/ 2008JE003181

Parteli, E. J. R., Herrmann, H. J., 2007. Dune formation on the present Mars. Physical Review E 76 (4), 041307. doi:10.1103/PhysRevE.76.041307.

Peterson, C., 1981. A secondary origin for the Central Plateau of Hebes Chasma. In: Lunar and Planet. Sci. XII Proceedings, Part B, pp. 1459–1471.

Poulet, F., Bibring, J.-P., Mustard, J. F., Gendrin, A., Mangold, N., Langevin, Y., Arvidson, R. E., Gondet, B., Gomez, C., the OMEGA Team, 2005. Phyllosilicates on Mars and implications for the early Mars history. Nature, 438, 623–627, doi:10.1038/nature04274.

Putzig, M.E., Mellon, M.T., Kretke, K.A., Arvidson, R.E., 2005. Global thermal inertia and surface properties of Mars from the MGS mapping mission. Icarus 173 (2), 325–341.

Pye, K., & Tsoar, H. 1990. Aeolian Sand and Sand Dunes. London: Chapman and Hall.

Roach, L. H., Mustard, J. F., Murchie, S. L., Bibring, J.-P., Forget, F., Lewis, K. W., Aharonson, O., Vincendon, M., Bishop, J. L., 2009. Testing evidence of recent hydration state change in sulfates on Mars. J. Geophys. Res., 114, E00D02, doi:10.1029/2008JE003245.

Rossi, A. P., Neukum, G., Pondrelli, M., van Gasselt, S., Zegers, T., Hauber, E., Chicarro, A., Foing, B., 2008. Large-scale spring deposits on Mars? J. Geophys. Res., 113, E08016, doi:10.1029/2007JE003062.

Rubin, D.M. 1990. Lateral migration of linear dunes in the Strzelecki Desert, Australia. Earth Surface Processes and Landforms 15, 1–14.

Rubin, D. M., & Hunter, R. E. 1985. Why deposits of longitudinal dunes are rarely recognized in the rock record. Sedimentology 32, 147–157.

Rubin, D. M., Hunter, R. E., 1987. Bedform alignment in directionally varying flows. Science 237, 276–278.

Sharp, R. P., 1963. Wind Ripples. J. of Geol., 71, No. 5, 617-636.

Schultz, R.A., 1998. Multiple-process origin of Valles Marineris basins and troughs, Mars. Planet. Space Sci., 46, 827–834.

Schultz, R.A., Lin, J., 2001. Three-dimensional normal faulting models of the Valles Marineris, Mars, and geodynamic implications. J. Geophys. Res., 106 (B8), 16,549–16,566.

Tokano, T. 2007. Dune-forming winds on Titan and the influence of topography. Icarus, 194, 243-262

Thomas, P., Veverka, J., Lee, S., Bloom, A., 1981. Classification of wind streaks on Mars. Icarus, 45, 124– 153.

Tsoar, H. 1983. Dynamic processes acting on a longitudinal (seif) dune. Sedimentology 30, 567–578.

Van Boxel, J. H., Arens, S. M., Van Dijk, P. M., 1999. Aeolian processes across transverse dunes. I: Modeling the air flow

Vaniman, D.T., Bish, D.L., Chipera, S.J., Fialips, C.I., Carey, J.W., Feldman, W.C., 2004. Magnesium sulfate salts and the history of water on Mars. Nature 431 (7009), 663–665.

Warren, J., 1999. Evaporites. Blackwell Sciences, London. 438 pp.

Werner, B.T., 1995. Eolian dunes: computer simulations and attractor interpretation. Geology 23, 1107– 1110.

Wiggs, G. F. S., Bullard, J. E., Garvey, B., Castro, I., 2002. Interactions between airflow and valley topography with implications for aeolian sediment transport. Physical Geogr., 21(5), 366– 380.

Witbeck, N.E., Tanaka, K.L., Scott, D. H., 1991. The geologic map of the Valles Marineris region, Mars. U.S. Geol. Surv. Misc. Invest. Map, I-2010.

Chapter 4: Overall Conclusions

Analysis of the deformation, deposition and erosional patterns of ILD in West Candor Chasma has provided several insights into the evolution of West Candor and of the ILD themselves. In Chapter 2, the preferred orientations of the small-scale faults and fractures parallel to the chasma-forming faults indicate a close relationship between them and possibly a related origin. The orientation of the deformation features further implies chasma-forming faults were active after ILD emplacement, likely in response to a continuation of the imposed stress that initially generated the chasma-forming faults.

The brittle deformation of the ILD demonstrates that the ILD were emplaced and lithified prior to the onset of deformation. Moreover, the small displacement of the exposed deformation features indicates that the deformation features record only minor amounts of strain; hence no significant offset on any existing underlying faults, could have occurred, if they exist.

The deformation exhibited by the CLF, discussed in Chapter 3, indicates the chasma-forming faults were active subsequent to ILD formation, after the CLF formed and lithified. Given the number of preferred orientations displayed by the various types of deformation features it is likely West Candor has undergone multiple episodes of deformation.

The conformity of the CLF morphology with aeolian dunes indicates they initially formed as such but were later lithified and deformed in a brittle manner. The onlapping relationship between the lithified dunes and the LTU further suggests that conditions conducive to kieserite formation were present after the aeolian bedforms were deposited. The conditions necessary for kieserite formation, together with the elevation of apparent

strandlines in the southeast of the chasma, suggest that the southeast re-entrant of Ceti Mensa contained standing water at one time.

As Ceti Mensa would have already been an isolated ILD mound (either through erosion or collapse of the chasma floor) in order for lithified dunes to form along its flanks, the lithified dunes formed relatively late in the history of West Candor Chasma. Therefore, circulating water responsible for lithification was active during the later stages of chasma development. This timeline indicate that West Candor has undergone multiple episodes of significant deposition and erosion since ILD formation.

The research contained in this thesis is meant to further our understanding of the evolution of Valles Marineris and constrain the formation of ILD, both in age and mechanism. To this end, I have demonstrated that following deposition of the main ILD stack in West Candor, was at least one period of aeolian dominated deposition, followed by a period in which the presence of water permitted the deposition of the sulfates that comprise the LTU.

Future research should be dedicated to continuing the measurement of small-scale deformation feature orientations in the other chasmata of Valles Marineris to confirm their origin, as they should have also been influenced by the imposed stress field responsible for the parallel alignment of chasmata. Future research could also be dedicated to identifying other areas where lithified dunes of similar morphology are present in an effort to better understand the cause of their low thermal inertia values.